ASPECT DEPENDENT EFFICIENT MULTIPATH GHOST SUPPRESSION IN THROUGH THE WALL RADAR WITH COMPRESSIVE SENSING

BY

ABDI TALIB ABDALLA

A Dissertation Presented to the
DEANSHIP OF GRADUATE STUDIES

KING FAHD UNIVERSITY OF PETROLEUM & MINERALS

DHAHRAN, SAUDI ARABIA

In Partial Fulfillment of the
Requirements for the Degree of

DOCTOR OF PHILOSOPHY

In

ELECTRICAL ENGINEERING

April, 2016

KING FAHD UNIVERSITY OF PETROLEUM & MINERALS

DHAHRAN- 31261, SAUDI ARABIA

DEANSHIP OF GRADUATE STUDIES

This thesis, written by **Abdi Talib Abdalla** under the direction of his thesis advisor and approved by his thesis committee, has been presented and accepted by the Dean of Graduate Studies, in partial fulfillment of the requirements for the degree of **DOCTOR OF PHILOSOPHY IN ELECTRICAL ENGINEERING**.

Dr. Ali A. Al-Shaikhi

Department Chairman

Dr. Salam A. Zummo

Dean of Graduate Studies

12/5/16

Date

Dr. Ali H. Muqaibel
(Advisor)

Dr. Azzeddine Zerguine
(Member)

Dr. Tareq Al-Naffouri
(Member)

Dr. Abdulmalek Zidouri
(Member)

Dr. Wail Mousa
(Member)

The memory of my beloved parents who passed away before I finished my studies

ACKNOWLEDGMENTS

My unreserved praises and gratitude to Allah (SWT) for his blessings on me and my family members. I feel privileged to glorify his name in a sincere way through this accomplishment. I ask for his blessings, mercy and forgiveness all the time. I sincerely ask him to accept this effort as an act of worship. May his peace and blessing be upon the prophet Muhammad, and his family.

I feel obliged to grant my individual thanks to my advisor Dr. Ali. Hussein Muqaibel for his challenging guidance, patience, caring and motivation that enlarged my competence on the field. I am thankful for his good cooperation shown for the whole period of my dissertation. His good communication and contribution led to my successful completion of this work.

I am deeply grateful to my dissertation committee members, Dr. Azzeddine Zerguine, Dr. Tareq Al-Naffouri, Dr. Abdulmalek Zidouri and Dr. Wail Mousa for their constructive comments, suggestions, and continual supports.

I would like to extend my special, sincere and hearty thanks to Mr. Mohammad Tamim Alkhodary and Mr. Umar Johar for their cooperation that made my work to be much simpler. They always gave me hope and all necessary supports for successful completion of this work.

Without my colleagues, Saleh Alawsh and Ali Albeladi, this work would not finish in time with some credible contents. Their heartfelt contributions and transparencies during the whole period of my study are memorable.

A special thanks to the King Fahd University of Petroleum and Minerals, particularly to the Electrical Engineering Department and also the University of Dar es Salaam for their support and cooperation.

Finally, I have to thank my family at large, my wives and my children for their patience and strong support by giving me an ample time to concentrate on my research work by sacrificing their precious times.

TABLE OF CONTENTS

LIST OF TABLES

LIST OF FIGURES

LIST OF ABBREVIATIONS AND ACRONYMS

AD	Aspect Dependent
AM	Additive-Multiplicative
BP	Basis Pursuit
CD	Change Detection
CoSAMP	Compressive Sampling Matching Pursuit
CRLB	Cramer-Rao Lower Bound
CS	Compressive Sensing
DOA	Direction of Arrival
DoF	Degree of Freedom
DSBF	Delay and Sum Beamforming
EM	Electromagnetic Wave
EMD	Earth Mover's Distance
ET	Extended Target
FDTD	Finite Difference Time-Domain
FL-SAR	Forward Looking Synthetic Aperture Radar

HMAM	Harmonic Mean-based AM
IF	Improvement Factor
LASSO	Least Absolute Shrinkage and Selection Operator
ME	Multipath Exploitation
MP	Matching Pursuit
MIMO	Multiple Input Multiple Output
MVM	Multi-View Monostatic
NLOS	Non Line of Sight
NMSE	Normalized Mean Square Error
NSP	Null Space Property
OT	Other Techniques
PDSA	Pythagorean based Displaced Subarrays
PISA	Pythagorean-based interlaced Subarrays
PPT	Primitive Pythagorean Triple
PSF	Point Spread Function
PT	Point Target
RF	Radio Frequency

ROMP	Regularized Orthogonal Matching Pursuit
SABMP	Support Agnostic Bayesian Matching Pursuit
SAR	Synthetic Aperture Radar
SCR	Signal to Clutter Ratio
SFR	Stepped Frequency Radar
SNR	Signal to Noise Ratio
SOCA	Spatial Orthogonal Coprime Arrays
SP	Subspace Pursuit
StOMP	Stage-wise Orthogonal Matching Pursuit
SVD	Single Value Decomposition
TIF	Target Improvement Factor
TWRI	Through-the-Wall Radar Imaging
UWB	Ultra-wide Band
UUP	Uniform Uncertainty Principle
VR	virtual radars
WSAM	Weighted Sum-based AM

LIST OF SYMBOLS

d	width of the front wall
ε_r	relative permittivity of the front wall
c	speed of EM wave in vacuum
v	speed of EM wave in the wall
θ_{air}	reflection angle in air
θ_{wall}	reflection angle in wall
k	number of internal reflections within the wall
τ_{np}	round trip delay between the n^{th} array and p^{th} target
R	Number of multipath returns due to the interior walls
R_w	Number of multipath due to the front wall
f_m	m^{th} frequency
$y[m,n]$	received signal at n^{th} array when m^{th} frequency transmitted
$y_w[m,n]$	received signal at n^{th} array when m^{th} frequency transmitted due to front wall
M	total number of frequency bins
N	total number of radar positions
N_x	number of pixels along cross range direction
N_y	number of pixels in down range direction
σ_p	target reflectivity
s	image vector

$\check{\boldsymbol{s}}_{\boldsymbol{i}}^{(\mathbf{0})}$	modified image vector
$\widetilde{\check{\boldsymbol{s}}_{\boldsymbol{\imath}}^{(\mathbf{0})}}$	estimated modified image vector
$\boldsymbol{\Phi}^{(\mathrm{r})}$	$M \times N_x N_y$ linear system relates the original signal and measurements due to the r^{th} return
A	measurement matrix
B	Signal bandwidth
B	Scan matrix of measurement vectors
$\widehat{N}$	Number of active elements in Pythagorean array
G	Pythagorean aperture gain
Δx	Target span along crossrange direction
Δy	Target span along downrange direction
Δf	Frequency step size
$\sigma_{q_{xz}}$	Reflectivity of the point (x, z) on the q^{th} ET
ΔR	Downrange resolution
ΔR_C	Crossrange resolution
λ	Signal wavelength
R	Target range
J	Number of compressed measurements

LIST OF PUBLICATIONS

Journal papers

1. A. H. Muqaibel, A. T. Abdalla, S. Al-Dharrab, “Aspect dependent efficient multipath ghost suppression in TWRI with compressive sensing” *Journal of Radioengineering.* Submitted
2. A. T. Abdalla and A. H. Muqaibel, “Through-the-Wall Radar Imaging Exploiting Pythagorean Coprime-Based Synthetic Apertures with Sparse Reconstruction”, *Digital Signal Processing.* Submitted
3. A. T. Abdalla and A. H. Muqaibel, “Indoor target localization using marginal antenna with virtual radars support”, to be Submitted
4. A. T. Abdalla, M. T. Alkhodary and A. H. Muqaibel, “Extended Target Modelling and Agnostic Block Sparse Reconstruction in Through-the-Wall Radar Imaging: A Different Perspective”, to be Submitted

Conference papers

5. A. T. Abdalla, A. H. Muqaibel, S. Al-Dharrab, “Aspect dependent multipath ghost suppression in TWRI under compressive sensing framework” *ICCSPA’15*, *Sharjah UAE, 2015*.
6. A. T. Abdalla and A. H. Muqaibel, “Multiple Target Sparse Reconstruction in TWRI Utilizing Ghost’s Aspect Dependence Feature”, *in 2015 IEEE International RF and Microwave Conference (RFM 2015), Malaysia.*

7. A. T. Abdalla and A. H. Muqaibel, “Single-View Bistatic Sparse Reconstruction in TWRI Exploiting Ghost’s Aspect Dependence Feature”, *in 2016 IEEE Wireless Communications and Networking Conference (IEEE WCNC2016), Doha, Qatar.*
8. A. T. Abdalla and A. H. Muqaibel, “Multipath Ghost Suppression in TWRI Exploiting Aspect Dependence Feature with Pythagorean Triple Coprime-Based Arrays”, *To be submitted*

ABSTRACT

Full Name : [Abdi Talib Abdalla]
Thesis Title : [Aspect Dependent Efficient Multipath Ghost Suppression In Through-the-Wall Radar with Compressive Sensing]
Major Field : [Electrical Engineering]
Date of Degree : [April 2016]

Recently, Through-the-Wall Radar Imaging (TWRI) society has witnessed a dramatic milestone after successful application of Compressive Sensing (CS) and sparse image reconstructions. However, multipath propagation is still a challenging problem. Multipath creates ambiguities in the measurements which result in ghost targets that can be confused with genuine targets. In this dissertation, multipath ghost suppression method based on Aspect Dependent (AD) feature is developed under CS framework. A measurement procedure is proposed using strategically selected duo-subaperture to realize the AD feature. The corresponding subimages are fused using either weighted sum or harmonic mean based techniques proposed in this work. Apart from using small fraction of the measurement, the knowledge of the reflecting geometry is not needed making the proposed method feasible. The results based on MATLAB and experimental data returned Target Signal-to-Clutter Ratio (TSCR) of 97.3dB and Target Relative Clutter Peak (TRCP) of 23.7dB which are relatively higher compared to the existing methods.

It was found that under given conditions, the optimal configuration to suppress multipath ghost is to divide the aperture into two, reconstruct the respective subimages and then combine them via effective fusion technique. Our contribution answer the questions as how many subapertures and how to divide the aperture to effectively suppress the ghosts.

To enhance the performance of the proposed method, sparse subarrays based on Pythagorean triple are proposed and evaluated. Two imaging modalities are examined: subarrays imaging followed by image fusion and imaging using combined subarrays. In each case, three configurations are discussed: Pythagorean-based Interlaced Sub-Apertures, Pythagorean-based Displaced Sub-Apertures (PDSA) and Spatial Orthogonal Coprime Arrays. The effectiveness of the subarrays is examined using MATLAB simulation and specialized EM propagation software. Imaging using duo-subarrays with PDSA configuration gives a TRCP of around 5dB higher than random selection.

In some applications, the conventional signal model does not hold because the target occupies more than one pixel. This work, extends the existing model to incorporate extended targets. The ground truth is modeled to contain complex shaped targets forming blocks of pixels of unequal sizes with unknown reflectivity distributions and the recently proposed blockSABMP algorithm is implemented in TWRI problem. The approach is scrutinized under different scenarios such as complex shaped target, non-homogeneous scene and Rayleigh distributed target. For all scenarios, it returns the best Earth Mover's Distance values and Normalized Mean Squared Errors compared to the existing algorithms.

Moreover, this work proposes a single antenna localization scheme for indoor target utilizing virtual radars. The fact that multipath returns are AD, the radar is located such that it receives minimal returns. This reduces wall ambiguity significantly and simplifies the process of associating the multipath to their respective walls. Simulation results show that the proposed method is robust for a good range of timing errors.

ملخص الرسالة

الاسم الكامل : عبدي طالب عبد الله
عنوان الرسالة : قمع الأشباح بكفاءة عالية اعتماداً على الجانب في نظام التصوير الراديوي من خلال الجدار
باستخدام الاستشعار المضغوط
التخصص : الهندسة الكهربائية
تاريخ المناقشة : أبريل 2016

شهدت تقنيات التصوير من خلال الجدار في الآونة الأخيرة تطوراً ملموساً بعد التطبيق الناجح لتقنية للاستشعار المضغوط وإعادة بناء الصور ذات الخاصية المتناثرة (sparse). تزود تقنية التصوير الراديوي من خلال الجدار، صور توضيحية مقربة للأهداف المراد تصويرها من خلف جدار ما، وذلك بالاعتماد على الأشعة الكهرومغناطيسية. في تقنية التصوير من خلال الجدار، تتسبب الجدران المحيطة بالأهداف المراد تصويرها بتبعثر وانتشار الأشعة الكهرومغناطيسية ورجوعها إلى الرادار سالكة مسارات متعددة. مما ينتج عن ذاك غموضاً في القياسات وذلك يؤدي إلى ظهور أهداف إضافية في الصورة مع أنها غير موجودة في الحقيقة، هذه الأهداف الغير حقيقية تسمى (أشباح). في الجانب التطبيقي لهذه التقنية، يؤدي ظهور الأشباح في الصور النهائية إلى مزج بين الأهداف الحقيقية وغير الحقيقية، مما يؤدي إلى خطأ في تفسير الصورة خلال عملية الكشف. في هذه الرسالة، يتم قمع الأشباح بناءً على المزايا التي تعتمد على الجانب في التصوير الراديوي وباستخدام بيانات مضغوطة وقليلة الحجم. نقترح إجراء القياس باستخدام اختيار استراتيجي لتحقيق ميزة الاعتماد على الجانب بالإضافة إلى استخدام الاستشعار المضغوط. بعد ذلك يتم الجمع بين الصور التي أعيد بناؤها باستخدام التقنية المقترحة وبكفاءة عالية. في هذا العمل، ليست هناك حاجة لمعرفة الشكل الهندسي للمشهد المراد تصويره خلف الجدار، مما يجعل الطريقة المقترحة أكثر جدوى. تظهر نتائج المحاكاة لهذه الطريقة والبيانات التجريبية فعالية الطريقة المقترحة. بصرف النظر عن استخدام جزء صغير من المعلومات، ليست هناك حاجة لمعرفة الشكل الهندسي مما يجعل الطريقة المقترحة مجدية. أظهرت النتائج المبنية على محاكات برنامج الماتلاب MATLAB والبيانات التجريبية أن نسبة إشارة الهدف إلى نسبة إشارة إلى الفوضى (TSCR) هي 97.3dB أما إشارة الهدف النسبية فهي 23.7dB والتي تعتبر عادية نسبيا مقارنة مع الأساليب القائمة.

لتعزيز أداء الطريقة المقترحة، تم استخدام أماكن متناثرة جزئية من مصفوفة التصوير (subarrays) والتي اختيرت على أساس أرقام شبه أولية (coprime) وثلاثية فيثاغورس وقد تم تقييمها. تم أيضا في الرسالة اختبار طرق التصوير الراديوي التالية: التصوير باستخدام اثنين من جزئيات مصفوفة التصوير ثم تليها تقنية الدمج الانصهاري الفعالة وأخيراً التصوير باستخدام جزئيات مصفوفة التصوير مجتمعة. في جميع الطرق المذكورة، تم مناقشة إعدادات "جزئية مصفوفة التصوير". يتم فحص فعالية الطرق المقترحة على التصوير باستخدام محاكاة في برنامج الماتلاب وبرامج متخصصة متخصص لتوليد بيانات كهرومغناطيسية.

إن النموذج التقليدي الذي يقترح أن الأهداف المراد تصويرها تمثل نقطة واحدة في الصور الراديوية ليس واقعياً، لأن الهداف عادة ما تحتل أكثر من نقطة (بكسل). نقترح في هذا العمل نموذجاً مطوراً والذي يأخذ بعين الاعتبار الأهداف الغير نقطية والممتدة عبر أكثر من بكسل. لقد تم تصميم الأهداف المرجعية بأشكال هندسية معقدة وممتدة على أكثر من بكسل وتحمل قيماً مجهولة التوزيع الاحصائي. تظهر النتائج باستخدام برنامج المحاكاة الماتلاب والبيانات التجريبية فعالية الطريقة المقترحة.

وعلاوة على ذلك، تم اقترح مخطط لتحديد المكان باستخدام هوائي واحد للاستخدام الداخلي من خلال معلومات من الرادارات الافتراضية. بما أن المسارات المتعددة للأشعة المنعكسة تعتمد على الجانب التصويري، فقد تم تحديد موقع الهوائي بحيث يستقبل أقل إشارات منعكسة ممكنة، وذلك بالاعتماد على الشكل الهندسي للمشهد المراد تصويره، وبالتالي تم خفض غموض الجدران بشكل كبير جداً، مما يسهل عملية ربط الأشعة المنعكسة بالهدف الأصلي. وتبين نتائج المحاكاة أن الطريقة المقترحة قوية وفعالة لمجموعة واسعة من الأهداف والتوقيت الزمني.

.

"The most learned of men is the one who gathers knowledge from others on his own; the most worthy of men is the most knowing and the meanest is the most ignorant."

Muhammad ibn Abdullah

CHAPTER 1

INTRODUCTION

The ultimate objective of Through-the-Wall Radar Imaging (TWRI) is to obtain high-resolution images of behind the wall scenes using electromagnetic (EM) waves. TWRI has been sought out in rescuing missions in case of fire or earthquake tragedies, in determining interior structures of inaccessible buildings, in performing inspection for law enforcing and military applications [1]–[7]. This technology has witnessed a tremendous growth and attracted the attention of many researchers in the last few years.

One of the major challenges facing TWRI is multipath stemming from multiple reflections of EM waves from the walls, floors and ceilings [2], [3], [5], [8], [9]. Vast amount of research findings are available today illustrating the adverse effects of multipath on urban communications and radar imaging and how to mitigate those effects. In TWRI multipath reflections give rise to replica of targets during image reconstruction and increase the probability of false alarm. The copies of the true target, referred to as ghosts, populate the scene and cause confusion with genuine targets. Without an effective and efficient multipath ghost suppression techniques, TWRI technology may result in an incorrect scene interpretation which can lead to improper resources allocation. Recently, ghost suppression in TWRI applications became topical and attracted the attention of many researchers.

High-resolution images in both, range and crossrange demand wide bandwidth signal and large aperture, respectively. Thus, huge amount of data needs to be stored and processed [1], [10]. In [10], the authors tackled this problem by applying compressive sensing (CS) techniques to TWRI application assuming a sparse scene. As a result, only small fraction of data was used to reconstruct images without compromising the quality. Hence, ghost suppression methods under CS framework inevitably become the preferred solution for sparse scene scenarios.

According to [4], [11]–[13] and the references therein, multipath ghosts are Aspect Dependent (AD): the location of the ghost changes with the transceiver location. This feature has been successfully used to identify and suppress multipath ghosts from a group of genuine targets. To the best of our knowledge, no research has been presented for ghost suppression employing AD feature under CS framework.

This dissertation proposes an efficient and practical multipath ghost suppression technique in TWRI which incorporates AD feature of the ghosts with the application of CS. In this work, a general signal model which mimics a real TWRI scenario is considered. The model includes the front wall reflection and reverberation, the target-to-side-wall reflections and target-to-target interactions which were not considered before.

1.1. Motivation

The main intention of TWRI systems is to provide useful information of obscured areas. Such information is useful in a number of daily life activities including but not limited to, law enforcing, rescue missions in earthquakes and fire tragedies. A clear and unambiguous image of the scene will make the mission more successful, which is the area of interest of many researchers in TWRI community. This area of research has witnessed a tremendous growth in the last few years. Many contributions are now available from different countries around the world under renowned projects with U.S, Germany, China, Netherlands and Turkey being among the prominent contributors to this field. Though, multipath phenomenon, and hence ghost formation, remains among the challenges facing the field as acknowledged by the radar community [8]. The presence of multipath ghost in the reconstructed image causes incorrect image interpretation and leads to waste of resources due to the increased false alarms.

Currently, the field has found an increased interest after successful application of CS for image reconstruction which guarantees high quality images using only few measurements. Based on the reviewed literature, the field has not been extensively explored in the area of image quality improvement especially under CS framework. The issues of multipath ghost and clutter reduction techniques need to be revisited to incorporate CS. As a result system complexity, efficiency, and their practicability will be highly improved. It is also pointed out in [4], [8], [12] that multipath ghost exhibits AD property which can be exploited to identify ghosts from a collection of true targets but none implemented with CS. This dissertation proposes a technique that can efficiently suppress ghosts exploiting AD feature under CS framework.

1.2. Literature Review

Available contributions on TWR literature fall into one of the following categories: detection, localization, or classification of targets. Different techniques have been applied to achieve the goals but Multipath Exploitation (ME) and CS based techniques found considerable attention lately. Different ME and CS approaches are available [2], [5], [14], [15] and some of the contributions evaluate and/or improve their performances to TWR applications as in [16]–[18]. Interestingly, most of the recent contributions integrate ME with CS to achieve the same goals in a more efficient manner [1], [7], [8], [19]–[21] as shown in Figure 1-1. Besides, multipath suppression methods exploiting AD characteristic of the ghost has been examined [4], [12], [13], [22].

There are other techniques including exploitation of phase history of subapeture images [23], [24], MIMO radar systems [25]–[27] and coarray-based aperture applications [28], [29] are also encountered in the TWRI technique.

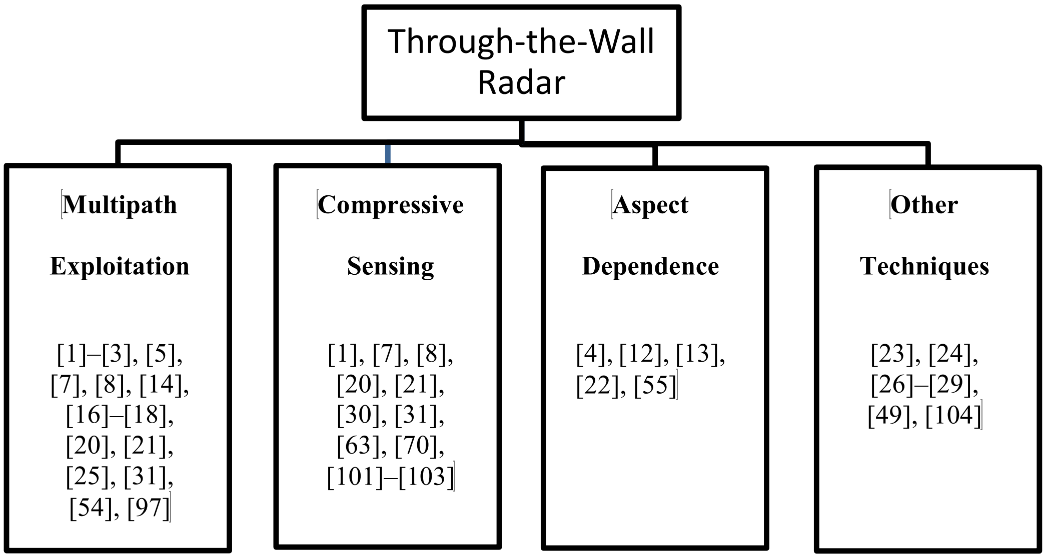

Figure 1-1: TWRI general overview in recent years.

1.2.1. Focused Literature Survey

A handful of contributions in TWRI address the problem of multipath ghost suppression in image reconstruction. The reviewed contributions on multipath ghost suppression can be broadly categorized in three groups: ME-based; CS-based and AD-based ghost suppression methods as summarized in Figure 1-2. Our emphasis was on recently published contributions in TWRI literature.

The proposed contributions in this work tend to fill the gap on the intersection of AD and CS as shown in Figure 1-2.

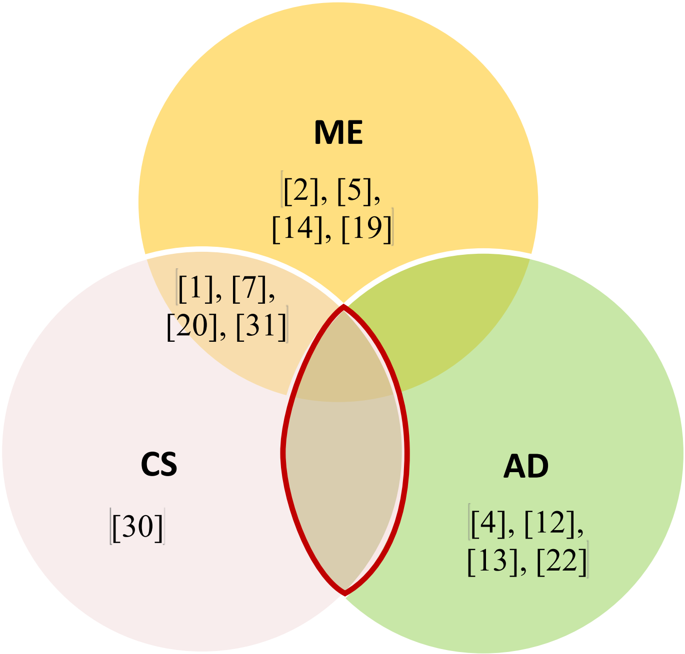

Figure 1-2: Dissertation covers the intersection of AD and CS.

The authors in [14] exploited specular multipath in TWRI to suppress ghosts. In their paper, they developed a scheme that takes advantage of the additional energy residing in the ghosts for stationary or slowly moving targets. The proposed technique starts by forming an image using Synthetic Aperture Radar (SAR), and then calculating the locations of the ghosts for each target and mapping each ghost target back onto the corresponding target location and hence increases Signal-to-Clutter Ratio (SCR) of the genuine targets. However, the technique involves very complex mathematical expressions and requires knowledge of the number of targets which is not always available. Also, when the ghost overlaps with a true target location, the technique is silent. In [19], the authors exploited the formed multipath ghosts to improve the target classification instead. The technique starts by localizing the ghost targets and then the ghosts are included in the classification process by concatenating them with the direct target images. It can be intuitively argued that the method will underperform when the number of targets increases and in case the ghost overlap with any real target, the method will not work as well. In [2], the authors improved their results in [14] by using point spread functions in conjunction with multipath exploitation. This does not require a priori information about the number of targets unlike in [14] but again works on the full data volume. They derived closed-form expressions of the multipath ghost locations and the method associates and maps back the multipath ghosts to their true targets. Eventually, improves the effective SCR at the genuine target locations assuming free space propagation.

In [30], the authors proposed a blind multipath elimination by sparse inversion to remove wall clutters without multipath exploitation. The technique first identifies the strongest impulse response of the targets behind the wall and attributes that response to a primary target. Then, it calculates a delay operator that matches the primary response to similar reflections in the residual data. The next stage is to update the waveform to compensate for any distortions that may arise from the EM propagation through the wall. Finally, the three stages repeated until convergence. The complexity of the technique may outweighs its effectiveness.

There are two major contributions in the field presented by [1], [20]. The authors in [20] proposed an image reconstruction technique using CS. Their method inverts a specular multipath model and uses group returns of the same wall in one measurement matrix. Finally they applied group sparsity theory to reconstruct subimages. As the extension of [20], the authors in [1] incorporated the front wall reverberation effect which makes the approach more practical. They inverted multipath model assuming the knowledge of the reflecting geometry. Unfortunately, the complete knowledge of the geometry is not always available. Also, the model does not address the challenge of the targets interactions. Besides, the method requires high dimensional matrices and hence high memory demand and prolonged processing time. The work in [7], extends the previous work in [1] to incorporate the moving targets as well. However, the paper uses similar assumptions as in [1] for the Point-like Target (PT) and known reflecting geometry which enable model reversal and therefore, share the same drawbacks. Parallel to [20], the authors in [31] also proposed a CS based multipath ghost suppression technique using SAR assuming prior knowledge of the propagation environment. Based on the multipath model, an over complete dictionary that accounts for interaction of the radar, targets and environment was constructed and then the image is reconstructed by solving convex optimization problem. Technically, their approach is similar to that proposed in [20] and therefore, suffers the same disadvantages.

There are two exciting recent contributions in the area utilizing AD feature of the multipath ghosts. The authors in [13] proposed an innovative multipath ghosts suppression method exploiting AD property of the ghost using full data set. The authors modeled the ghost positions as a hidden Markov chain problem. However, apart from limited resolution due to big data problem, their method shows some inherent challenges: requires image decomposition into N-subapeture images using directional filters; and also requires complex advanced algorithms. The authors in [4] proposed a multipath ghost suppression method exploiting AD characteristic without CS. The authors formed three images using back projection method; one using the whole aperture and two using subapetures. The method involves tedious searching of appropriate subapetures and shifting of antenna array in two extreme ends of the room which increases complexity and processing time. However, the attractive feature of their method is the simplicity of obtaining the final image. An inspiring contribution by [22], the authors proposed ghost suppression technique for target-to-target interactions. They examined different array configurations and image fusion strategies to combat the effect of the ghosts. However, the effect of side walls was not addressed which is unavoidable in TWRI applications.

Specific literature review for the subsequent contributions will be provided in their respective chapters.

1.3.Dissertation Contributions

The dissertation contributions with their corresponding publications are summarized as follows:

a) This work proposes a new multipath ghost suppression method in TWRI which exploits the AD feature under CS framework. The main aspect of the proposed method is the reduction of the size of the sensing matrix by around $\left(1-\frac{1}{R}\right)\times$

100% compared to the recently published work based on model-reversal for R multipath case. Only a pair of reduced and strategically collected measurements are used to identify and then suppress ghost's artifacts. Besides, it relaxes the constraint of the knowledge of the reflecting geometry.

The effectiveness of the proposed suppression method has been scrutinized under single and multiple targets scenarios, joint-wall target reconstruction, Multi-View Monostatic (MVM) and Single-View Bistatic (SVB) setups and it bode well in all possible scenarios. We set up and conduct experiments to evaluate the effectiveness of the proposed method under practical data [6], [32]–[34].

b) Also, sparse arrays based on Primitive Pythagorean Triple (PPT) coprime numbers are proposed to ensure sufficient multipath resolvability with design simplicity. Pythagorean triple are pairwise coprime numbers and their squares also pairwise coprime which helps to design arrays with sufficient number of active elements and yet with feasible lengths. In this work, we address the best array configuration through Pythagorean coprime subarrays under given conditions. Results based on MATLAB simulation and specialized electromagnetic propagation software show the effectiveness of the proposed array configurations[35].

c) The existing signal model is extended to incorporate extended targets and we suggest the most appropriate target model which mimics the real TWRI scenarios casting it as block sparse problem with varying block sizes and unknown pixel value distributions. We implement the recently proposed block *Support Agnostic Bayesian Matching Pursuit (*Block*SABMP)* algorithm into TWRI problem, to the best of our knowledge such algorithm which is agnostic to the signal distribution and works for different block sizes has not been applied in TWRI before. The two inherent properties of the algorithm match the properties of the vectorized scene in TWRI. In multiple target scenario, we have multiple extended targets having different reflectivity distributions which are not necessarily known a priori. Even if the distribution of each extended target pixels is known but vectorizing the scene will result into a vector with complex distribution.

d) Further, the work come up with a single antenna based indoor target localization method exploiting virtual radars. This was possible due to aspect dependence property of specular multipath components which do exist only at certain radar locations. The use of marginal radar has reduced the wall ambiguity and reduced the computational complexity significantly compared to the latest published similar approaches. We derive closed-form expressions for the target locations exploiting virtual radar's information given the knowledge of the reflecting geometry. We also develop a closed-form expression for the maximum localization error. Simulation results show that the method is robust to the timing errors and can localize with good accuracy [36].

e) Additionally, the work extends the current received signal model based on point-target assumption to a more general model which best reflect the real TWRI scenario. The model takes into account the front wall reflections and reverberations, the side-wall reflections and target-to-target interaction as well. In CS based approaches, the target-to-target interaction has been ignored due to nonlinear behavior. In this work, we model the target-to-target interaction as a linear component by imposing additional but justifiable assumptions.

f) We also propose two image fusion strategies which outperform the traditional image masking approach [32]–[34]:

    (i) Weighted Sum-based Additive Multiplicative (WSAM) fusion: the intermediate image takes the weighted sum of the subimages such that it minimizes the clutter norm and maintain the true targets casting it as an optimization problem.

    (ii) Harmonic Mean-based Additive Multiplicative (HMAM) fusion: The fact that harmonic mean of a list of numbers leans towards the least elements of the list and maintains the same value for equal elements, can be utilized to suppress large clutters in TWRI while it maintains the true targets.

For full list of publications, refer to page xxii.

1.4.Dissertation Organization

This dissertation is organized as follows: Chapter 2 gives relevant technical background material to understand the concepts of TWRI and CS theories. A generalized received signal model taking into account the front wall contribution, side wall reflection and target-to-target interaction is presented and discussed. The adverse effect of multipath returns and hence ghost formation in TWRI are articulated herein. Besides, the basics and rationales of CS application in TWRI applications are enumerated. Further, the expected performance measures are described as well.

In Chapter 3, a multipath ghost suppression method for stationary targets exploiting AD feature of the ghost is presented and its effectiveness is evaluated using both simulated measurements and experimental data. Also, the two devised image fusion strategies based on harmonic mean and weighted sum of the individual images are elaborated.

In Chapter 4, sparse arrays based on Pythagorean triple coprime numbers are proposed for TWRI applications. Sensing matrix design and recoverability test are presented. Different array configurations are suggested and evaluated in view of TWRI applications.

Proposed ghost suppression techniques are applied to extended targets in Chapter 5. A different perspective on Extended Target (ET) modelling and reconstruction is presented therein.

Chapter 6 describes a novel indoor target localization scheme based on multipath exploitation. The method which localizes a single stationary target using single antenna in an enclosed environment is proposed and its performance against timing errors is evaluated.

Conclusions and recommendations for the future works are summarized in Chapter 7.

“If you can’t explain it simply, you don’t understand it well enough”
“A person who never made a mistake never tried anything new”
Albert Einstein

CHAPTER 2

THROUGH-THE-WALL RADAR IMAGING ESSENTIALS

Due to its diverse applications, TWRI is rapidly growing and attracting the attention of many researchers. The current trend in TWRI research is the application of CS to improve image quality while reducing the data acquisition and image reconstruction times. This chapter intends to highlight technical background materials on which our research is built. The chapter presents the essentials of TWRI and related CS theories. Besides, the rationale of using CS to TWRI is elaborated. The effect of multipath due to the scattered EM waves from the surrounding walls and nearby targets on the image reconstruction and interpretation is delineated herein.

The rest of the chapter is organized as follows: Section 2.1 presents TWRI system design parameters. Radar resolutions, sensitivity and dynamic range are highlighted. Section 2.2 presents the models of the scene and the received signals. The effects of interior walls, front wall and target interactions are outlined. A new linearized formulation of the target-to-target interaction is suggested herein. In Section 2.3, the ghost formation in TWRI is described and their properties are enumerated. Section 2.4 explains the available wall mitigation techniques under reduced measurements based on spatial filtering and subspace projection. Section 2.5 gives a background on CS theory particularly in TWRI applications. Section 2.6 gives an overview of the conventional image formation algorithm based on Delay and Sum Beamforming (DSBF) algorithm. Section 2.7 defines the performance metrics that will be used in this work and Section 2.8 summarizes the chapter.

2.1. Through-the-wall Radar Imaging

TWRI aims at sensing through building walls using RF signals to reveal targets located behind the wall. In the TWRI literature, the scene of interest is mostly interrogated using either pulsed radar or Stepped-Frequency Radar (SFR) system. In the two scenarios, the transmitted Ultra-wide band (UWB) signal is realized in time and frequency domain, respectively. For pulsed radar, to acquire higher resolution the transmitted pulses should have shorter duration thereby the transmitted bandwidth increases. As presented in the radar literature, the Signal-to-Noise Ratio (SNR) is a function of the transmitted energy in the radar signal [37]–[39]. The energy of the pulse is specified by the transmitted peak power in the pulse and the pulse width. When transmitting shorter pulses to earn higher range resolution, results to low energy being transmitted and hence reduces SNR for a given transmitter power [37]. The radar engineers suggested radar waveforms with longer time to acquire high energy but at the same time give better range resolution. One approach is transmitting a series of monochromatic waves of linearly increasing frequency one after the other, known as stepped frequency signal. Throughout this work, SFR is assumed unless otherwise stated. In the following sub-sections, the nuts and bolts of the SFR design are delineated.

2.1.1. Step Frequency Radar Design Parameters

In SFR, a series of M monochromatic waves whose frequency monotonically increases by a constant value, called frequency step size, Δf, as shown in Figure 2-1, are transmitted and received at each radar location with the initial frequency value f_0 and the final value f_{M-1}. The number of transceivers in a physical array or positions in SAR determine the aperture length of the radar system.

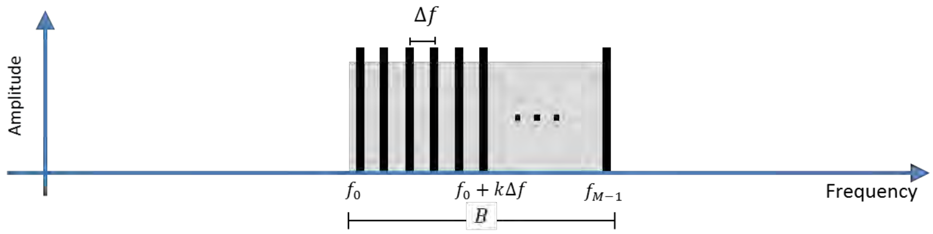

Figure 2-1: stepped frequency signal.

The choice of Δf is very crucial in the SFR design as it dictates the maximum range that the system can image without ambiguity. The maximum unambiguous range, R_{max}, is given by [40]:

$$R_{max} = \frac{c}{2\Delta f} \tag{2.1}$$

In addition to unambiguous range, there are other crucial parameters in SFR design including radar resolutions, sensitivity and its dynamic range.

2.1.2. Downrange and Crossrange Resolution

Radar resolution measures the capability of the radar to distinguish two close targets in downrange and crossrange directions [40]. The downrange resolution, ΔR , expressed in meters, refers to the ability of the radar system to resolve distinct targets positioned along the same angular location but at different downranges. Mathematically, ΔR is given by [40]:

$$\Delta R = \frac{c}{2B} = \frac{c}{2M\Delta f} \tag{2.2}$$

where c denotes the speed of the RF signal in the free space and B is the signal bandwidth.

The downrange resolution improves with increasing bandwidth and that explains why the modern TWRI systems employ UWB signals.

On the other hand, the crossrange resolution, ΔR_C expressed in meters, refers to the ability of the radar to distinguish adjacent targets laying at the same downrange but with different angular displacements. For the SAR system of aperture length, L, operating with RF signal of wavelength, λ, imaging two targets located at a range, Ɽ, then the crossrange resolution is given by [40], [41]:

$$\Delta R_C = \frac{\lambda Ɽ}{2L} \tag{2.3}$$

The crossrange resolution in (2.3) improves with increasing aperture length and this explains why the modern TWR systems use SAR to realize large aperture when physical array becomes infeasible. It is also inferred in (2.3) that the crossrange resolution is range dependent, i.e. the farther the targets they are, the lower the crossrange resolution the radar can achieve for a given aperture and the same operating frequency.

The above equation was derived for radars with narrow frequency band, monostatic configuration, and one-dimensional SAR processing. When using UWB signals the λ varies significantly across the frequency band and therefore, the system in such case uses upper bound instead [42].

2.1.3. Sensitivity and Dynamic Range of the Radar

Radar sensitivity in a nutshell, is the minimum input RF power that the radar can detect. It provides a measure of the radar's ability to detect the presence or absence of a target [40], [43]. The dynamic range on the other hand, is quantitatively defined as the ratio between the strongest signal to the weakest signal registered by the radar system and is normally expressed in dB [40], [43]. This number quantifies the maximum amount of loss that the radar signal can have, and still be detectable in the receiver [37]. In TWRI applications, strong reflections from the surrounding clutters including the front wall, if not well handled, may limit the radar's dynamic range which might saturate or even block the receiver and jeopardize the detection of the targets with low cross-sections. In which case they are treated as noise.

In the recent years, clutter mitigation was the area of interest with which front wall clutter can be dealt with prior to target detection [44]–[46]. The dominant challenge in TWRI applications is the multipath components which severely affect target reconstruction and interpretation. This area has drawn attention of many researchers lately. To better address multipath challenges and possible remedial measures, a realistic multipath propagation model is needed.

2.2.Scene Geometry and Received Signal Model

In TWRI, both transmitter and receiver are situated on the same side, few meters from the front wall referred to as back-off distance. Electromagnetic waves traverse two different media from the transmitter reaching the receiver in a round trip fashion after being reflected by the behind the wall target. The signal undergoes a significant distortion as the wave is refracted twice, once at the air-wall interface and then at the wall-air interface in the forward direction. When moving from the target back to the receiver similar action happens [1], [6].

When the signal reaches the target it might be reflected at one or multiple secondary reflectors as depicted in Figure 2-2 resulting to multipath phenomenon. The Figure 2-2 shows a scene model comprised of a front wall and three side walls with N transceiver locations. Multipath returns can be broadly categorized as follows: interior wall; floor/ceiling; wall ringing; and target-to-target interaction multipaths [1], [20]. The multipath due to the interior wall can be further subdivided into first-order, second-order or higher-order multipath. In first-order case, only one interior wall is involved, one trip is directly from or to the target and others involves the wall to complete the trip. In second-order multipath, there are two cases; one similar to the first-order except that the signal reflect on two interior walls and there is also a monostatic scattering scenario where transmission and reception occurs along the same path but involves secondary reflector. Whereas higher-order involves at least three secondary reflectors. Higher-order multipath can be neglected as the received signal becomes very weak due to the additional reflections. Also the prolonged delay resulting from many secondary reflections for many presumed target locations is equivalent to the direct-path delay of a target that lies outside the perimeter of the room being imaged [1], [20].

In the literature the received signal model has been considered superficially to simplify the analysis. In TWRI, the received signal comprises of many components including the front wall returns, direct returns from the targets, reflections due to the interior walls, front wall reverberations, target-to-target interaction and floor/ceiling returns. In this work, a more general model is used to best represent TWRI scenarios.

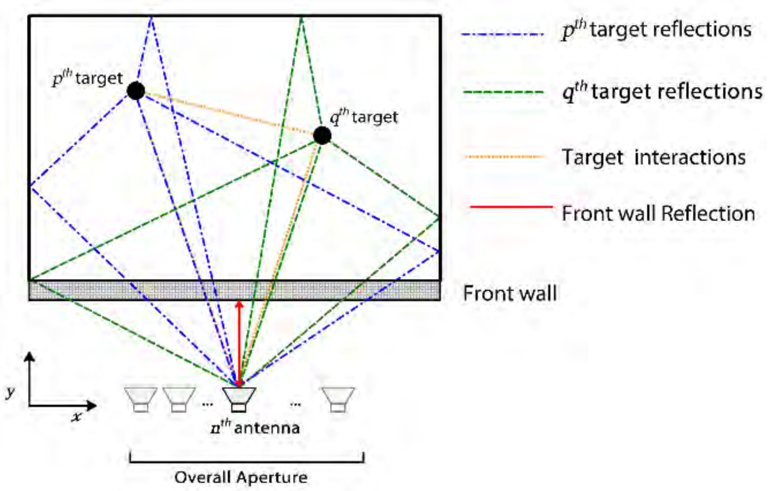

Figure 2-2: TWRI multipath scenario with first order returns.

2.2.1. Interior Wall Multipath Model

In Figure 2-3 a simple TWRI interior wall reflection scenario with only one interior wall is depicted to elaborate the idea. Consider a p^{th} target located at $z_p = [x_p, y_p]^T$, and the interior right wall as shown in Figure 2-3 is parallel to the y-axis and is located at $x = x_w$. With specular reflection assumption, there are two propagation paths: from the n^{th} antenna located at x_n to the target following the path-A and back to the antenna after reflection via path-B. The second path is the direct path without any wall reflection. As a result, we observe that the reflected return yields alternative antenna-target geometry. According to TWRI literature, a virtual radar is realized and located behind the same wall at $[2x_w - x_n, 0]$ simulating bistatic configuration and the delay associated with path-B is the same as that from the target to the virtual radar. This correspondence simplifies the calculation of the one-way propagation delay from the target back to the receiver as indicated by path-B. The same principle can be readily applied to the remaining walls. The associated delay is obtained by dividing Euclidean distance by the speed of the EM wave assuming the ray tracing model.

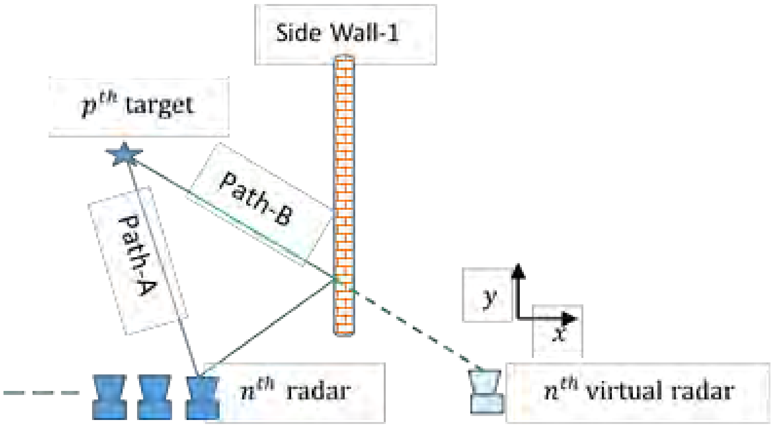

Figure 2-3: Multipath Propagation via Reflections from Interior Walls.

2.2.2. Front Wall Reverberations Model

Besides, multipath stemming from multiple reflections of the interior walls, another big challenge of TWRI is the presence of the front wall. As the wave propagates through the front wall, it gets reflected from the outer and inner surfaces of the wall causing multiple reflections within the wall. This phenomenon known as wall ringing or reverberation [1], [47]. As a result of wall ringing, copies of true targets "ghosts" in the reconstructed image are generated that are equally spaced in the radial direction from the array with exponentially reducing intensity[1]. The front wall returns on the other hand can be dealt with using available wall mitigation techniques [44]–[46], [48].

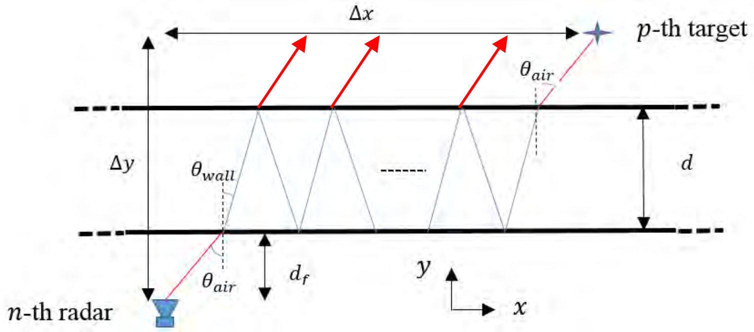

Figure 2-4: Wall reverberation model

Figure 2-4 shows the effect of wall reverberation on the transmitted signal. The distance between the target and the array element in crossrange direction, Δx, can be expressed as:

$$\begin{aligned} \Delta x &= d_f \tan\theta_{air} + d(1+2k)\tan\theta_{wall} + \left(\Delta y - d - d_f\right)\tan\theta_{air} \\ \Delta x &= (\Delta y - d)\tan\theta_{air} + d(1+2k)\tan\theta_{wall} \end{aligned} \tag{2.4}$$

where Δy is the distance between target and array element in the downrange direction, θ_{air} and θ_{wall} are the angles in the air and in the wall medium, respectively, d is the width of the wall and k is an integer which denotes the number of internal reflections within the wall. In many cases k assumes the value of two to three [49]. The two angles are related by Snell's law [49]:

$$\frac{\sin\theta_{air}}{\sin\theta_{wall}} = \sqrt{\varepsilon_r} \tag{2.5}$$

where ε_r defines the relative permittivity of the wall. Equations (2.4) and (2.5) form a nonlinear system which can be solved for the unknown angles using numerical methods such as Newton method [8]. The one-way time delay that a given return will undergo due to k wall reverberations will be [8]:

$$\tau(\Delta x, \Delta y, k) = \frac{(\Delta y - d)}{c \cos \theta_{air}} + \frac{d\sqrt{\varepsilon_r}(1 + 2k)}{c \cos \theta_{wall}} \tag{2.6}$$

2.2.3. Target-to-Target Interaction Multipath Model

In some applications, the interaction between the targets is significant and cannot be ignored as the trend in the recent literature portray. In this work, the target interaction is considered when modeling the received signal and is formulated to comply with the available linear models. As demonstrated in Figure 2-2, some signal components reflect at the nearby targets as they head to the receiver. The target interactions results in a non-linear signal component which brings complexity particularly when applying CS. To overcome this complexity we hypothesize that *for two nearby and interacting targets, the overall reflectivity can be transferred to one of the target and the other target being considered as perfect reflector of a unit reflectivity*. Therefore, the resulting multipath return will be interpreted as coming from a physical target of reflectivity equal to the product of the individuals.

2.2.4. Received Signal Models

Having described the possible multipath contributions in the TWRI applications, suppose there are N different radar locations defining radar aperture. At each location, M equally spaced monochromatic waves are transmitted and received to realize an ultra-wideband (UWB) signal. Similar signal was used by [20], [50], [51] in their analysis. The scene is divided into N_x by N_y pixels where N_x and N_y are the number of pixels in crossrange and downrange, respectively, as shown in Figure 2-5. The target reflectivity on a p^{th} grid point is represented by σ_p, with $p = 0, 1, \dots, N_x N_y - 1$. If R target returns and R_w wall returns are considered, then the received signal at the n^{th} radar position when the m^{th} frequency, f_m, is $y[m, n]$, with $n = 0,1,2, \dots, N-1$ and $m = 0,1,2, \dots, M-1$. The received signal comprises of four main contributions: reflection from the front wall, target-to-side wall reflection, target-to-target reflection and ambient noise. It is therefore, given by:

$$\begin{aligned} y[m,n] = & \sum_{r=0}^{R-1} \sum_{p=0}^{N_x N_y - 1} \sigma_p^{(r)} \exp\left(-j2\pi f_m t_{pn}^{(r)}\right) + \sum_{r_w=0}^{R_w-1} \sigma_w^{r_w} \exp\left(-j2\pi f_m t_w^{(r_w)}\right) \\ & + \sum_{r=0}^{R-1} \sum_{\substack{p,q=0 \\ p \neq q}}^{N_x N_y - 1} \sigma_{pq}^{(r)} \exp\left(-j2\pi f_m t_{pqn}^{(r)}\right) + v(m,n) \end{aligned} \tag{2.7}$$

where $t_{pn}^{(r)}$ represents the round-trip delay between the p^{th} target and the n^{th} receiver due to the r^{th} return, $t_{pnq}^{(r)}$ is the round trip delay between p^{th} and q^{th} targets with n^{th} transceiver and $t_w^{(r_w)}$ is the time delay of the r_w^{th} front wall return. While $\sigma_p^{(r)}$ and $\sigma_w^{r_w}$ are the target and wall pixel reflectivity, respectively, with respect to the r^{th} and r_w^{th} returns return and $v(m,n)$ is the noise sample. The overall signal reflectivity due to the interactions is $\sigma_{pq}^{(r)} = \sigma_p^{(r)} \sigma_q^{(r)}$.

If multipath are not well modeled, then unwanted targets will be created during image reconstruction resulting to misleading interpretation. These hypothetical, unwanted targets are known as *ghosts*.

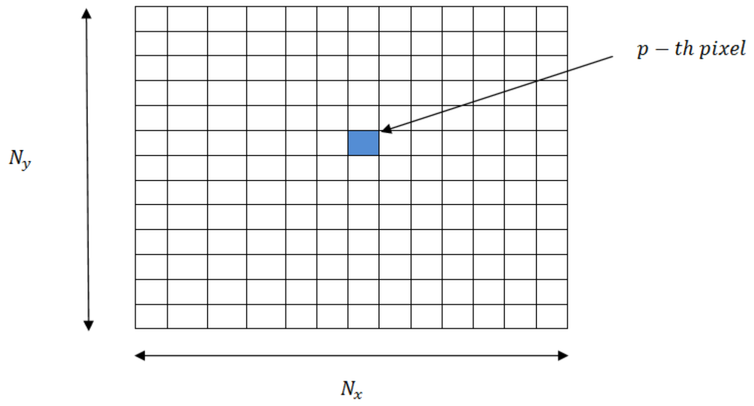

Figure 2-5: Imaged scene sub-divided into pixels.

2.2.5. Single-View Bistatic Configuration

Based on the theoretical framework of the problem, the performance of the ghost suppression method based on AD feature is a strong function of the array setup. In the previous sections, the analysis was solely made on MVM radar configuration. However, based on the reviewed literature, bistatic radar configuration shown to affect multipath propagation due to the change in the reflecting geometry and hence ghost locations [51]–[54]. Unlike in MVM configuration, in SVB configuration the transmitter is fixed and the receiver moves along the aperture to scan the area of interest.

Figure 2-6 shows the SVB radar configuration where the transmitter, T_X, is kept fixed at predefined location and N receiver locations defines the aperture. The transmitter emits a series of M monochromatic waves one by one after the other and received at each of the N receiver locations to interrogate the scene. The received signal at the n^{th} receiver location when the m^{th} frequency, f_m, is transmitted, $y[m,n]$ is similar to that of MVM with exception of the time delay. The delay in this case, is the summation of the delays from the transmitter to the target and that from the target to the receiver as shown in Figure 2-6 with all symbols carry usual meanings. When taking the effect of the front wall into account, the expression will change accordingly as presented in [49].

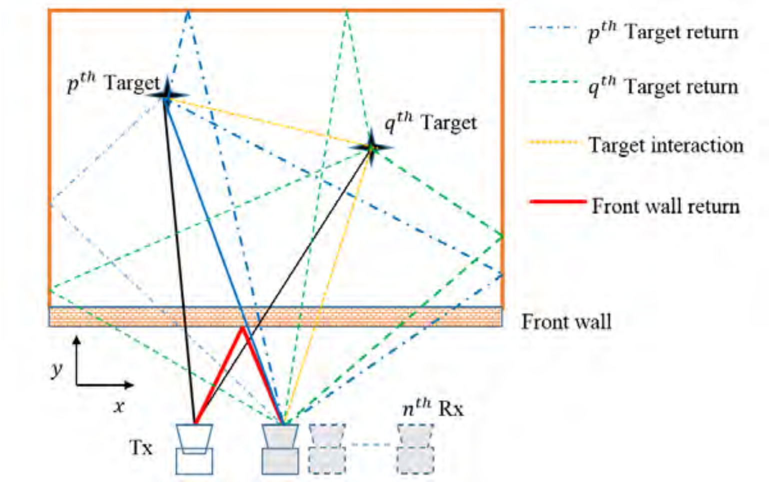

Figure 2-6: SVB first order multipath scenario.

2.3.Ghost Formation in TWRI

In TWRI applications employing physical array or SAR, ghost targets result from interaction of the genuine targets with secondary reflectors such as surrounding walls or with targets themselves. The front wall causes ghost only when the signal component undergoes multiple internal reflections, *wall reverberation*. The ghosts due to the front wall reverberation effect appear in downrange direction with their spacing as a function of wall thickness and relative permittivity [6], [8]. When the signal travels from the transceiver to the target, part of it propagates straight to the target and other components get reflected by the walls, floor and ceiling before reaching the target or after being reflected back from the target to the receiver. The signal components scattered by the same target register different delays due to different reflecting geometries as shown in Figure 2-7 (a)-(c). In this case, the receiver interprets each of the delayed versions as they come from different physical targets and results into hypothetical targets as depicted in Figure 2-7 (d). The formed ghosts with the true targets fall on concentric circles with the transceiver location being their common center. In this way, the scene becomes populated and the number of expected ghosts grows proportionally with the number of true targets for a given reflecting geometry. Suppose there are P true targets in the scene and R signal returns were recorded by the transceiver. The number of multipath ghosts is upper bounded by $P(R-1)$ assuming specular reflection.

The locus of the ghost location with respect to the transceiver due to the presence of a given wall when employing monostatic configuration is estimated mathematically by considering the average time delay from the transceiver to the target (path-A) and the delay from the target back to the transceiver (path-B) as shown in Figure 2-7. Suppose that the time delay of the signal from the radar to the target and that from the target to the radar via the right wall is τ_A and τ_B, respectively. The possible location of the true target is described by the circle with the radius $c\tau_A$. The locus of the ghost location due to a single bounce (first-order reflection) on the right-side wall is a circle with radius $c\left(\frac{\tau_A+\tau_B}{2}\right)$ as shown in Figure 2-7 (d). If the signal undergoes reflection twice at the wall (second-order reflection), the resulting ghost will reside $c\tau_B$ away from the radar as depicted in Figure 2-7 (d) with $\tau_B > \left(\frac{\tau_A+\tau_B}{2}\right) > \tau_A$. The presence of the left and back walls generates ghosts in a similar fashion. During SAR image reconstruction and interpretation, the formed ghost targets pose some technical challenges. However, their peculiar properties can be exploited to identify and then suppress them.

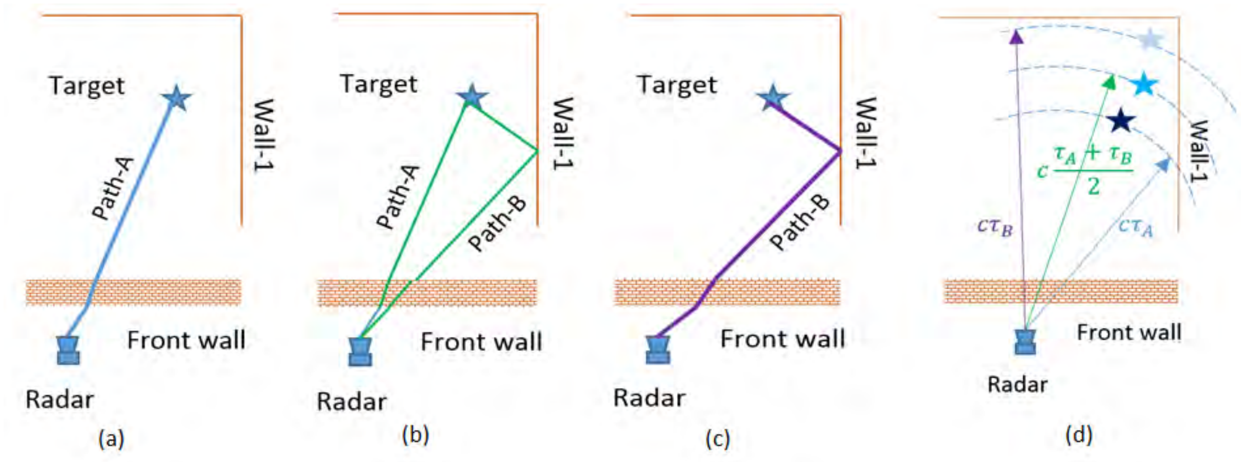

Figure 2-7: Some indoor multipath scenes (a) direct propagation (b) first-order interior bounce (c) second-order interior bounce (d) corresponding target and ghost locations.

The properties of multipath ghosts include lower crossrange resolution, non-ideal focusing and aspect dependence (AD).

A. *Lower crossrange resolution*

In SAR imaging, downrange resolution and crossrange resolution of a radar system are functions of the signal bandwidth and the aperture size, respectively. During through-the-wall sensing, direct return is registered at every radar locations making the image of the true target highly resolved in crossrange direction. However, multipath returns only exist at some locations of SAR making the image of ghost target exhibit less resolution compared to that of real target [55]. This property of ghosts is termed as *lower crossrange resolution*.

B. *Non-ideal focusing*

Consider a ghost of a given target positioned at (x, z) with the system origin at the center of the array. Due to the presence of a right wall located at crossrange of w_1, the prospective focusing location of the ghost is $(w_1 + x)/2$ in crossrange direction. But during the SAR image formation, the ghost is found at $(x + w_1)/2 + c(\tau_B - \tau_A)/2$ instead, see [55] for detailed information. This property of the ghost is referred to as *non-ideal focusing.*

C. Aspect dependence

In TWRI, changing the transceiver location, alters the signal reflecting pattern and therefore, registers different values of the round-trip delays. If the scene is interrogated using different locations, their corresponding ghosts reside in different pixels. This property of the ghost is referred to as *Aspect Dependence (AD)*. On the other hand, the true targets locations remain unchanged regardless of the array shift making identification of ghost from genuine target possible. The effectiveness of this property on multipath ghost suppression is demonstrated in [6], [8], [12], [13], [55]. In this work, the AD feature is utilized to suppressed multipath ghosts under CS framework making the method more efficient and feasible.

The application of the CS entails the sparsity condition on the scene of interest, which might be challenged in the presence of the front wall. Therefore, the front wall contribution needs to be mitigated before the image reconstruction process.

2.4.Front Wall Mitigation

The main challenge of the front walls is the strong EM reflections which obscure the targets, rendering target detection and classification difficult, if not impossible [44], [48]. Without an effective wall clutter mitigation method, the targets may not be detected in the presence of strong wall reflections. For moving targets scenario, the wall effect can be alleviated by using change detection technique [8], [56]. Though, this is not possible for stationary target scenario, in which case the front wall reflections should be properly attenuated before image formation. In recent literatures, the common front wall mitigation techniques applied under CS framework include spatial filtering and Singular Value Decomposition (SVD) based approaches [44], [48].

2.4.1. Spatial Filtering Approach

The fact that front wall contribution has zero spatial frequency, meaning the delays of the wall returns do not vary with the radar locations. Then, the front wall return can be distinguished from the target returns under spatial domain. The received signal when the m^{th} frequency is transmitted at the n^{th} radar locaton, $y[m,n]$, has therefore, two components with regards to spatial variations. Separating front-wall reflections from target reflections amounts to basically separating a zero-frequency signal from non-zero frequency valued signals across antennas, which can be achieved using a proper spatial filter [45], [48]. Mathematically, the spatial filter which notches out the constant component can be realized as the subtraction of the average value of the return across the array from the total return. The filtered signal, $\tilde{y}[m,n]$ is therefore, given by [48]:

$$\tilde{y}[m,n] = y[m,n] - \frac{1}{N}\sum_{n=0}^{N-1} y[m,n] \tag{2.8}$$

2.4.2. Wall Mitigation Based on Singular Value Decomposition

The second approach to mitigate the contribution of the front wall under CS framework is SVD based approach [44], [46], [48]. Suppose that the received signals using N antennas when transmitting M equally spaced frequencies are arranged into an $M \times N$ matrix, **B** [48]:

$$\mathbf{B} = [\mathbf{b}_0\ \mathbf{b}_1 \ldots \mathbf{b}_{\mathrm{n}} \ldots \mathbf{b}_{\mathrm{N-1}}] \tag{2.9}$$

where $\mathbf{b}_n$ is the $M \times 1$ column vector containing the stepped frequency signal received by the n^{th} radar given by:

$$\mathbf{b}_n = [y(0,n)\ \ldots y(m,n)\ \ldots y(M-1,n)]^T \tag{2.10}$$

Performing SVD of **B**, gives:

$$\mathbf{B} = \mathbf{UDV}^{\mathrm{H}} \tag{2.11}$$

where H denotes the conjugate transpose, **U** and **V** are unitary matrices containing the left and right singular vectors, respectively, and **D** is a diagonal matrix containing the singular values $\lambda_1, \lambda_2, \ldots \lambda_N$ in descending order.

It is assumed in SVD based approach that the front wall and target reflections lie in different subspaces. Therefore, the first K dominant singular vectors of the **B** matrix are used to construct the wall subspace $\boldsymbol{S}_{wall}$ [48]:

$$\mathbf{S}_{\mathrm{wall}} = \sum_{k=1}^{K} \boldsymbol{u}_k \boldsymbol{v}_k^H \tag{2.12}$$

Defining $\boldsymbol{S}_{wall}^{\perp}$ as the subspace orthogonal to the wall subspace, we can write:

$$\mathbf{S}_{\mathrm{wall}}^{\perp} = \mathbf{I} - \mathbf{S}_{\mathrm{wall}} \mathbf{S}_{\mathrm{wall}}^{\mathrm{H}} \tag{2.13}$$

where **I** denotes the identity matrix. Now, projecting the **B**-scan matrix on the orthogonal subspace, the wall returns will be mitigated, given by:

$$\widetilde{\mathbf{B}} = \mathbf{S}_{\text{wall}}^{\perp}\mathbf{B} \tag{2.14}$$

In [48], it was shown that both spatial filtering and subspace methods for wall mitigation give better results when applied under CS framework. In this work, the spatial filtering will be used.

2.5.Compressive Sensing

Compressive Sensing (CS) or sometimes referred to as compressed sampling states that a sparse or compressible signal can be reconstructed using fewer measurements compared to the signal dimension contrary to conventional linear algebra theory [41], [57]. A *sparse signal* refers to a signal in which only few of its entries are non-zero. While compressible signal means a signal with fewer significant entries but the remaining are not necessarily zeros.

Many applications today with TWRI as one example, face the *big data* challenge. To acquire, process, and store this large amount of data using traditional techniques becomes a nightmare. Although in many applications, most of the collected data are insignificant and can be omitted without compromising the quality of the expected signal. For the past years, all these data were captured and then compressed off-line by dropping all insignificant ones. But CS provides a way to simultaneously acquire and compress the signal. This capability drastically reduces the cost and time for data acquisition and processing [58], [59].

Further, CS theory suggests that a signal which is not sparse or compressible in its original domain may have sparse representation in other domains [58], [59]. For example, a sinusoid signal is not sparse in time domain but it is in the frequency domain. Since most of real life phenomena including but not limited to radar imaging, seismic activities, speech signals and videos, to name a few, exhibit sparsity in certain domains, CS finds itself attractive as it enables significant reduction in data volumes. Hence, complexity and processing time without compromising signal contents.

CS theory asserts that one can recover certain signals and images from far fewer samples or measurements below the Nyquist rate. To make this possible, CS relies on two principles: sparsity, which pertains to the signals of interest, and incoherence, which pertains to the sensing modality [59].

To comprehend the idea, consider a sparse signal $\boldsymbol{s} \in \mathbb{C}^{N_x N_y \times \mathbf{1}}$ denotes a 2D image signal of length $N_x N_y$ as presented in the previous sections. The secret behind CS reconstruction is that we acquire the measurements as linear combinations of its elements and not samples of the signal. For notational simplicity, let $\mathbf{A} \in \mathbb{C}^{J \times N_x N_y}$ with $J \ll N_x N_y$ be a sensing matrix which defines the linear combinations of the elements of $\boldsymbol{s}$ and $\overline{\boldsymbol{y}} \in \mathbb{C}^{J \times 1}$ being the compressed measurement vector which is a linear projection of $\boldsymbol{s}$. Mathematically, we can write $\overline{\boldsymbol{y}}$ in the presence of Gaussian noise, $\boldsymbol{v}$, as:

$$\overline{\boldsymbol{y}} = \mathbf{A}\boldsymbol{s} + \boldsymbol{v} \tag{2.15}$$

A crucial stage in CS application is the design of $\mathbf{A}$ to ensure the signal information is preserved otherwise it will lead to erroneous reconstruction. If the vector of interest is not sparse in the original domain, then it can be transformed using arbitrary basis resulting to a sparse vector. Suppose, $\boldsymbol{\theta}$ is the sparse representation of $\boldsymbol{s}$ using transformation $\boldsymbol{\phi}$ such that $\mathbf{s} = \boldsymbol{\phi\theta}$. The design of $\mathbf{A}$ in this case depends very much on the sparsifying matrix. The CS theory asserts that the columns of $\mathbf{A}\boldsymbol{\phi}$ should be as much incoherent as possible to ensure recoverability. Among the performance criteria used to measure the recoverability of the given sensing matrix include Restricted Isometry Property (RIP), mutual coherence, *spark* and Null Space Property (NSP), to name a few [60]. Unlike RIP, *Spark* and NSP are needed in the noiseless scenarios and therefore, will not be good candidates in TWRI applications.

2.5.1. Restricted Isometry Property (RIP)

A sensing matrix, $\mathbf{A}$ is said to satisfy RIP of order P if there exists a $\delta_P \in (0,1)$ such that [59]:

$$(1-\delta_P)\|\boldsymbol{s}\|_2^2 \leq \|\mathbf{As}\|_2^2 \leq (1+\delta_P)\|\boldsymbol{s}\|_2^2 \tag{2.16}$$

for all $\mathbf{s} \in \sum_P = \{\boldsymbol{s}: \|\boldsymbol{s}\|_0 \leq P\}$

If **A** satisfies RIP, then this is sufficient condition for a variety of algorithms to be able to recover a sparse signal from noisy measurements.

In TWRI application, RIP tends to be cumbersome even if the sparsity of the scene is available as a result of lacking computationally tractable math [60]. Mutual coherence of the sensing matrix on the other hand, provides relatively easy alternative.

2.5.2. Mutual Coherence

In classical array literature, the array design focusses on the Point Spread Function (PSF). The normalized PSF is equivalent to the mutual coherence between columns of the sensing matrix in CS framework, which is the focus of this work. The mutual coherence of the matrix is the maximum absolute value of the inner product among all pairs of columns in the matrix [61], [62]:

$$\mu(\mathbf{A}) = \max_{i \neq j} \frac{|\boldsymbol{a}_i^H \boldsymbol{a}_j|}{\|\boldsymbol{a}_i\| \|\boldsymbol{a}_j\|} \tag{2.17}$$

where $\boldsymbol{a}_i$ is the i^{th} column vector of $\mathbf{A}$. In classical algorithms, it may also provide useful information on the performance of the given array including resolution, noise and other interference robustness and ambiguity information. When this metric returns a small value, it serves as sufficient condition to ensure unique signal reconstruction.

2.5.3. Signal Reconstruction Algorithms

Since (2.15) forms an underdetermined system, the traditional mathematics suggests infinite many solutions. However, if the signal of interest is sparse, then naturally one can think of l_0-norm minimization to acquire a unique solution which is given be:

$$\tilde{\boldsymbol{s}} = \underset{\mathbf{s}}{\operatorname{argmin}} \|\mathbf{s}\|_0 \;\text{ s.t. } \|\bar{\boldsymbol{y}} - \mathbf{A}\mathbf{s}\|_2 < \varepsilon \tag{2.18}$$

where ε is a function of noise power [63]. Basically (2.18) counts the number of non-zeros, and returns the sparsest solution. One inherent challenge with this approach is the requirement of exhaustive search over all possible supports of $\boldsymbol{s}$, which is infeasible, labeled as *NP-hard problem* [57].

It is reported in CS literature that the problem in (2.18) can be relaxed and the vector $\boldsymbol{s}$ in (2.15) can be reconstructed with high probability using at least $J = CP \log\left(\frac{N_x N_y}{P}\right)$ measurements by minimizing l_1-norm instead [57]:

$$\tilde{\boldsymbol{s}} = \underset{\mathbf{s}}{\operatorname{argmin}} \|\mathbf{s}\|_1 \;\text{ s.t. } \|\boldsymbol{y} - \mathbf{A}\mathbf{s}\|_2 < \varepsilon \tag{2.19}$$

This convex optimization problem now can be casted as linear program, referred to as Basis Pursuit (BP) and algorithms to solve such problems exist in abundancy. Computationally, BP are inefficient especially for large signals. To overcome this challenge, greedy algorithms, like Matching Pursuit (MP) were developed [62], [64]–[66], which finds the support of the unknown vector iteratively. MP algorithm is faster but is greatly challenged by stability. Besides, the algorithm requires computation of inner products which adds computational complexity especially for large size and less sparse vectors [57]. As improvement remedy to this shortcoming, a number of derivatives of the MP have been presented in the literature including but not limited to Compressive Sampling Matching Pursuit (CoSAMP), Stage-wise Orthogonal Matching Pursuit (StOMP), Subspace Pursuit (SP) and Regularized Orthogonal Matching Pursuit (ROMP) as narrated in [57].

In both, convex relation and greedy algorithms, the only priori information utilized is the signal sparsity. In some applications, statistical information of the noise is available in priori and making use of it is the crucial feature of the Bayesian algorithms.

Bayesian algorithms outperform the previous approaches as they make use of the additional statistical information of the signal other than sparsity. Currently, Bayesian based approaches attracted the attention of many researchers. Its theory has been dwelt on in [57], [67]. In Bayesian algorithms, the unknown signal is modeled as Bernoulli-Gaussian or Bernoulli-Laplacian. If the prior statistics is assumed to follow Gaussian distribution as in many contribution, then it allows a tractable math but its feasibility is limited. The support agnostic [57], [68], [69] on the other hand, is applicable when the support distribution is not Gaussian or even unknown in priori. In many real life with TWRI as an example, the information of the behind the wall targets are not necessarily known. As part of our contribution, TWRI signal model for Extended Target (ET) is reformulated and the sparse solution using agnostic Bayesian approach is suggested in Chapter 5.

2.5.4. Formulation of Compressive Sensing in TWRI

The emergence of TWRI technology was an incredible milestone in the radar imaging society which enable to capture images of the targets located behind walls. The demand of high resolution image in TWRI calls for wide signal bandwidth and large aperture and hence more data to be acquired, stored and processed [6], [8], [21], [70], [71]. To overcome the *big data* problem, an efficient data acquisition approach based on CS was introduced in TWRI by Yoon and Amin [72]. The findings in [72] was a breakthrough in the research of getting a clearer image while paying relatively less cost. In [72], it was shown that if the scene is sparse in which most TWRI applications satisfy, then CS can be applied to allow an efficient way of data acquisition. However, the presence of multipath ghosts and wall reverberations may cast a sparse scene as a populated scene, and at minimum will make the scene less sparse, thus degrades the performance of CS algorithms.

To apply CS, (2.7) has to be expressed as a linear system. Since the target-to-target contribution in (2.7) is non-linear, we suggest in this work that the overall signal reflectivity due to the target interactions, $\sigma_{pq}^{(r)}$ is dictated by the second target and first target is taken as perfect reflector. Then we can replace the term $\sigma_{pq}^{(r)}$ in (2.7) by $\beta_{q}^{(r)}$ and its corresponding matrix representation will be:

$$\begin{bmatrix} y[0,0] \\ y[1,0] \\ y[2,0] \\ \vdots \\ y[M-1,0] \\ y[0,1] \\ y[1,1] \\ \vdots \\ y[M-1,N-1] \end{bmatrix} = \begin{bmatrix} \exp\left(-j2\pi f_0 \tau_{0,0}^{(0)}\right) & \exp\left(-j2\pi f_0 \tau_{1,0}^{(0)}\right) & \cdots & \exp\left(-j2\pi f_0 \tau_{N_xN_y-1,0}^{(0)}\right) \\ \exp\left(-j2\pi f_1 \tau_{0,0}^{(0)}\right) & \exp\left(-j2\pi f_1 \tau_{1,0}^{(0)}\right) & \ddots & \exp\left(-j2\pi f_1 \tau_{1,0}^{(0)}\right) \\ \vdots & \vdots & & \vdots \\ \exp\left(-j2\pi f_{M-1} \tau_{0,0}^{(0)}\right) & \exp\left(-j2\pi f_{M-1} \tau_{1,0}^{(0)}\right) & & \exp\left(-j2\pi f_{M-1} \tau_{N_xN_y-1,0}^{(0)}\right) \\ \exp\left(-j2\pi f_0 \tau_{0,1}^{(0)}\right) & \exp\left(-j2\pi f_0 \tau_{1,1}^{(0)}\right) & & \exp\left(-j2\pi f_0 \tau_{N_xN_y-1,1}^{(0)}\right) \\ \exp\left(-j2\pi f_1 \tau_{0,1}^{(0)}\right) & \exp\left(-j2\pi f_1 \tau_{1,1}^{(0)}\right) & \cdots & \exp\left(-j2\pi f_1 \tau_{N_xN_y-1,1}^{(0)}\right) \\ & \vdots & & \vdots \\ \exp\left(-j2\pi f_{M-1} \tau_{0,N-1}^{(0)}\right) & \exp\left(-j2\pi f_{M-1} \tau_{1,N-1}^{(0)}\right) & & \exp\left(-j2\pi f_{M-1} \tau_{N_xN_y-1,0,N-1}^{(0)}\right) \end{bmatrix} \times \begin{bmatrix} \sigma_0^{(0)} \\ \sigma_1^{(0)} \\ \sigma_2^{(0)} \\ \vdots \\ \sigma_{N_xN_y-1}^{(0)} \end{bmatrix} + \cdots \tag{2.20}$$

Notational representation of (2.20) can be written as:

$$\mathbf{y} = \sum_{r=0}^{R-1} \boldsymbol{\Phi}^{(\mathrm{r})}\mathbf{s}^{(\mathrm{r})} + \sum_{r_w=0}^{R_w-1} \boldsymbol{\Phi}_w^{(r_w)}\mathbf{s}_w^{(r_w)} + \sum_{r=0}^{R-1} \sum_{\substack{p,q=0 \\ p\neq q}}^{N_xN_y-1} \boldsymbol{\Psi}_q^{(\mathrm{r})}\mathbf{s}_q^{(\mathrm{r})} + \mathbf{v} \tag{2.21}$$

where $\boldsymbol{s}^{(\boldsymbol{r})}$, $\boldsymbol{s}_q^{(\boldsymbol{r})}$, and $\boldsymbol{s}_w^{(\boldsymbol{r_w})} \in \mathbb{C}^{\boldsymbol{N_xN_y\times 1}}$, with $r = 0, 1, \dots R-1$ and $r_w = 0, 1, \dots R_w - 1$ represents the vectors of reflectivities, $\sigma_p^{(r)}$, $\beta_p^{(r)}$ and $\sigma_w^{r_w}$, respectively, whereas σ_{p} assumes a value of one if there is target at p^{th} pixel, otherwise zero. The entries of the matrices $\boldsymbol{\Phi}^{(\mathrm{r})}, \boldsymbol{\Phi}_w^{(r)}$and $\boldsymbol{\Psi}_q^{(\mathrm{r})} \in \mathbb{C}^{MN\times N_xN_y}$ are defined as:

$$\left[\boldsymbol{\Phi}^{(r)}\right]_{ip} = \exp\left(-j2\pi f_m t_{pn}^{(r)}\right) \tag{2.22}$$

$$\left[\boldsymbol{\Psi}_q^{(r)}\right]_{ip} = \exp\left(-j2\pi f_m t_{pnq}^{(r)}\right) \tag{2.23}$$

$$\left[\boldsymbol{\Phi}_w^{(r)}\right]_{ip} = \exp\left(-j2\pi f_m t_w^{(r)}\right) \tag{2.24}$$

$$m = i \bmod M, \qquad n = \left\lfloor \frac{i}{M} \right\rfloor, \qquad i = 0, 1, 2..MN-1$$

From (2.21) the reduced measurement vector, $\bar{\boldsymbol{y}}$, is obtained using down-sampling matrix, **D** given by:

$$\bar{\mathbf{y}} = \mathbf{D}\mathbf{y} \tag{2.25}$$

In TWRI, the sensing matrix can be viewed as the product of two matrices [60]. The first is a predefined matrix describing the signal propagation model (2.21) which is the function of the radar parameters and reflecting geometry. The second matrix is down-sampling matrix, $\mathbf{D}$ which compresses the measurements based on CS theories. Therefore, designing the sensing matrix in TWRI is basically designing $\mathbf{D}$. In practice, CS is applied directly during data collection. The image vector $\boldsymbol{s}$ is then reconstructed given reduced set of measurements, $\bar{\boldsymbol{y}}$ by solving optimization problem (2.19). In this dissertation, Yall1 algorithm [73] is used for image reconstructions, unless otherwise stated. The choice of Yall1 is based on the recent findings of Albeladi and Muqaibel [56] which evaluated the performance of CS algorithms in view of TWRI applications. To evaluate the effectiveness of the CS in the image reconstruction, it is compared with the conventional DSBF algorithm.

2.6.Delay and Sum Beamforming Algorithm

For performance comparison, conventional DSBF is frequently used to gauge the level of the reconstructed images using CS approaches. Given a set of measurements collected from N different transceiver locations using M monochromatic frequencies of carefully chosen band taking into account the allowable signal attenuation and practical antenna length. At each location, M signals are transmitted and received to interrogate the scene of interest. The complex image $I(x_p, y_p)$ of the p^{th} grid point (x_p, y_p) is obtained by summing phase shifted copies of the received signals [1], [50]:

$$I(x_p, y_p) = \frac{1}{MN}\sum_{n=0}^{N-1}\sum_{m=0}^{M-1} y[m,n]\exp(j2\pi f_m \tau_{pn}) \tag{2.26}$$

where τ_{pn} is the focusing delay associated by the n^{th} transceiver and the p^{th} grid point.

Consider a scene shown in Figure 2-8 (a) with three targets located at $(-2,3)m$, $(2,3.5)m$ and $(0,4.5)m$ is imaged using a $2m$ long aperture with 77 radar locations, parallel to the front wall around $2m$ away from the radar. A stepped frequency signal is used ranging from $1GHz - 3GHz$ with the total number of frequency, $M = 201$. The side walls reside at crossrange of $\pm 3m$, and the back wall at $6m$ downrange. The corresponding DSBF image using (2.7) and (2.26) is shown in Figure 2-8 (b) which is accompanied with the ghosts as a result of multipath phenomenon. The ghosts can adversely affect the quality of the image if not effectively suppressed.

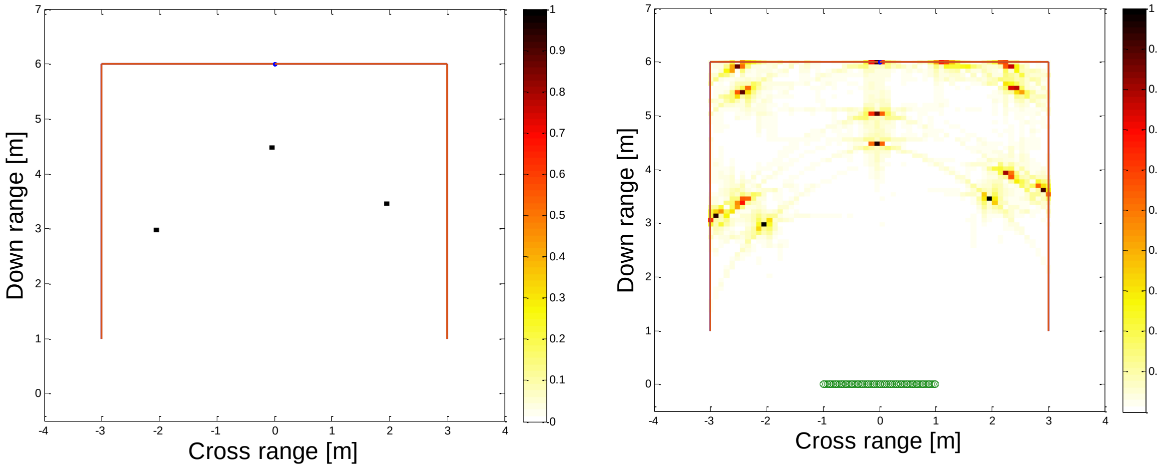

(a)

(b)

Figure 2-8: Imaging using DSBF (a) the scene (b) DSBF image

2.7. Performance Metrics

To quantify the performance of the reconstructed images, we defined three performance metrics: the Target Signal-to-Clutter Ratio (TSCR), the Target Relative Clutter Peak (TRCP) and the precision. In this context, the reconstructed ghosts are treated as clutters.

2.7.1. Target Signal-to-Clutter Ratio

The TSCR is defined as the ratio of the maximum target amplitude to the average amplitude in the clutter region. Mathematically, TSCR is given in logarithmic notation as [6], [8], [45]:

$$\mathrm{TSCR} = 20\log_{10}\frac{\max_{p\in A_t}|s(p)|}{\frac{1}{N_c}\sum_{p\in A_c}|s(p)|} \tag{2.27}$$

where A_t and A_c are the target and clutter areas, respectively, $s(p)$ is the signal value at corresponding to the p^{th} pixel and N_c is the number of clutter pixels. The clutter region in this work refers to area of the room excluding the target area.

2.7.2. Target Relative Clutter Peak

The TRCP on the other hand, is the ratio of the maximum target amplitude to the maximum clutter amplitude. It can be deduced from the previous equation as:

$$\mathrm{TRCP} = 20\log_{10}\frac{\max_{p\in A_t}|s(p)|}{\max_{p\in A_c}|s(p)|} \tag{2.28}$$

The TRCP is more crucial and should receive more attention as it tells how easy the target can be distinguished from the surrounding clutters. This has direct consequences on the target detection than TSCR. When the TRCP is relatively small, the probability of correct detection will be highly reduced and the rate of false alarms will therefore, increase.

2.7.3. Precision

A similar to TRCP but more informative performance measure is the precision. Denote TP as true positives and FP as false positives. The precision on the reconstructed image can be expressed as [56]:

$$\text{Precision} = \frac{TP}{TP + FP} \tag{2.29}$$

We treat ghost targets as false positives or false alarms and genuine targets as true positives. Precision gives information on the probability of correct target detection in the presence of ghosts. When it assumes the value of one, means the number of expected target was correctly reconstructed. Otherwise, the scene is contaminated with ghosts and other clutters.

In the subsequent chapter, we propose efficient method for multipath ghost suppression under CS framework. The effectiveness of the proposed method is scrutinized under different possible scenarios using both simulation and experimental data.

2.8.Conclusion

This chapter highlighted the nuts and bolts of the TWRI. It started with the important design parameters for SFR system. The scene and signal models were described and the new formulation of the target-to-target interaction was presented leading to a generalized signal model. The physics behind the ghost formation was given and the ghost properties were enumerated, one of which will be exploited to facilitate suppression process in the subsequent chapters. The chapter also described the concept of CS and the rationale behind its application to the TWRI applications. The effects of the front wall were outlined and how to combat them was narrated as well. The chapter also enumerated the performance metrics that will be used to evaluate the image quality.

It was pointed out in this chapter that the ghost locations are aspect dependent, this peculiar feature will be exploited to identify and suppress the ghost under reduced measurement volumes and will be discussed in the subsequent chapter.

> *"…echo time delays determine target locations, but multipath spread of electromagnetic wave will introduce false time delays. There are several methods to deal with this problem, in which the main consideration is to pick out direct reflecting delays between multiple reflecting delays and obtain certain involved parameters. However, these methods maybe efficient only in detecting single target or dispersing multiple targets rather than complex target regions forming easily multiple scattering…"*
>
> **Liang WANG** [55]

CHAPTER 3

MULTIPATH GHOST SUPPRESSION EXPLOITING ASPECT DEPENDENCE FEATURE IN TWRI UNDER COMPRESSIVE SENSING FRAMEWORK

3.1.Introduction

This chapter presents a proposed multipath ghost suppression technique which incorporates aspect dependence (AD) feature of the ghosts under CS framework. In conventional CS-based TWRI, a fraction of J measurements is randomly collected from a given aperture of

N locations. In this work, multiple of the same fraction are collected such that the AD feature is maximized and then their corresponding images are strategically combined to suppress the effect of the ghosts. Exploiting the AD feature allows simplification of the existing image reconstruction problem significantly by reducing the size of the measurement matrix. It is also eliminating the constraint of the knowledge of reflecting geometry as the method entails only direct return information of the given scene. A general scene and received signal model which best represent a real TWRI scenario as described in Chapter 2 is utilized to evaluate the proposed ghost suppression method. The model takes into account the front wall contribution; both reflections and reverberation, the target to side-wall reflections and target-to-target interaction as well.

To optimize the performance of the proposed method, we proposed two image fusion strategies which outperform the traditional image masking approach: Weighted Sum based Additive-Multiplicative (WSAM) fusion and Harmonic Mean based Additive-Multiplicative (HMAM) fusions. The former approach takes the weighted sum of the subarray images such that it minimizes the clutter norm and maintain the true targets casting it as an optimization problem. On the other hand, the latter uses the fact that harmonic mean of a set of numbers leans towards the least elements of the list while maintains the same value for equal elements. This property can be utilized to suppress large clutters including ghost in TWRI. The details of the two image fusion strategies will be presented in the sequel.

The effectiveness of the proposed method is shown using computer simulations and real experimental data. Both computer simulation and real experimental results under multiple targets condition show promising performance in terms of TSCR and TRCP and guarantee correct target detection at a given threshold value.

The rest of this chapter is organized as follows: Section 3.2 highlights the received signal models. Section 3.3 presents the proposed ghost suppression method based on duo-subaperture imaging. The sensing matrix design and analysis are presented in this section. Also, subimages sparse reconstruction and image fusion strategies are discussed. Section 3.4 presents the results based on both MATLAB simulation and experimental data. Results discussion and comparison to the recent findings are detailed. Finally, Section 3.5 concludes the chapter.

3.2.Received Signal Models

In the literature, the available signal models partially reflect the TWRI scenario. They do not collectively include all possible signal contributions. Therefore, the practicability of their corresponding multipath ghost suppression are questionable. In this work we use the generalized signal model presented in Chapter 2 which best reflect the TWRI scenario. The model include the front wall contribution, side-wall reflections and target-to-target interactions.

Considering the signal model (2.21) and we rewrite it here to provide a logical flow:

$$\mathbf{y} = \sum_{r=0}^{R-1} \mathbf{\Phi}^{(\mathrm{r})}\mathbf{s}^{(\mathrm{r})} + \sum_{r_w=0}^{R_w-1} \mathbf{\Phi}_w^{(r_w)}\mathbf{s}_w^{(r_w)} + \sum_{r=0}^{R-1} \sum_{\substack{p,q=0 \\ p\neq q}}^{N_xN_y-1} \mathbf{\Psi}_q^{(\mathrm{r})}\mathbf{s}_q^{(\mathrm{r})} + \mathbf{v} \tag{3.1}$$

$$\left[\mathbf{\Phi}^{(r)}\right]_{ip} = \exp\left(-j2\pi f_m t_{pn}^{(r)}\right) \tag{3.2}$$

$$\left[\boldsymbol{\Psi}_q^{(r)}\right]_{ip} = \exp\left(-j2\pi f_m t_{pnq}^{(r)}\right) \tag{3.3}$$

$$\left[\boldsymbol{\Phi}_w^{(r)}\right]_{ip} = \exp\left(-j2\pi f_m t_w^{(r)}\right) \tag{3.4}$$

$$m = i \bmod M, \qquad n = \left\lfloor \frac{i}{M} \right\rfloor, \qquad i = 0, 1, 2..MN - 1$$

where all symbols carry their usual meanings. In this work, two radar configurations will be examined: MVM and SVB as elaborated in Chapter 2 and hence two corresponding signal models and their performances will be analyzed in view of ghost suppression using AD feature. The main difference between the two models is the associated time delays. For the SVB configuration, the time delay in the above equations is defined as the time elapsed when the signal travel from a fixed transmitter to the receiver after striking the behind the wall target.

3.3. Duo-Subaperture Imaging

To address the challenges on the existing ghost suppression methods, we propose multipath ghost suppression technique which incorporates AD feature of the multipath ghosts under CS framework. The introduction of AD feature simplifies the problem in terms of complexity and relaxes the requirement of knowing the reflecting geometry. In this case, we can reconstruct the scene of interest without having to know the location of the reflecting walls.

In the reconstruction process, consider again equation (2.21) to be perfect inverse model. Factorizing in (2.21) with respect to $\boldsymbol{\Phi}^{(0)}$, gives:

$$
\begin{aligned}
\mathbf{y} = \mathbf{\Phi}^{(0)} \Bigg[& \mathbf{s}^{(0)} + {\mathbf{\Phi}^{(0)}}^{-1}\mathbf{\Phi}^{(1)}\mathbf{s}^{(1)} + \cdots + {\mathbf{\Phi}^{(0)}}^{-1}\mathbf{\Phi}^{(R-1)}\mathbf{s}^{(R-1)} + {\mathbf{\Phi}^{(0)}}^{-1}\mathbf{\Phi}_w^{(0)}\mathbf{s}_w^{(0)} \\
& + \cdots + {\mathbf{\Phi}^{(0)}}^{-1}\mathbf{\Phi}_w^{(R_w-1)}\mathbf{s}_w^{(R_w-1)} + {\mathbf{\Phi}^{(0)}}^{-1} \sum_{\substack{p,q=0 \\ p\neq q}}^{N_xN_y-1} \mathbf{\Psi}_q^{(0)}\mathbf{s}_q^{(0)} + \cdots \\
& + {\mathbf{\Phi}^{(0)}}^{-\mathbf{1}} \sum_{\substack{p,q=0 \\ p\neq q}}^{N_xN_y-1} \mathbf{\Psi}_q^{(R-1)}\mathbf{s}_q^{(\boldsymbol{R-1})} \Bigg] + \mathbf{v}
\end{aligned}
\tag{3.5}
$$

If we define a residual column vector, $\mathbf{w}$ which contains information from other subimages as:

$$
\begin{aligned}
\mathbf{w} = & {\mathbf{\Phi}^{(0)}}^{-1}\mathbf{\Phi}^{(1)}\mathbf{s}^{(1)} + \cdots + {\mathbf{\Phi}^{(0)}}^{-1}\mathbf{\Phi}^{(R-1)}\mathbf{s}^{(R-1)} + {\mathbf{\Phi}^{(0)}}^{-1}\mathbf{\Phi}_w^{(0)}\mathbf{s}_w^{(0)} \\
& + \cdots + {\mathbf{\Phi}^{(0)}}^{-1}\mathbf{\Phi}_w^{(R_w-1)}\mathbf{s}_w^{(R_w-1)} + {\mathbf{\Phi}^{(0)}}^{-1} \sum_{\substack{p,q=0 \\ p\neq q}}^{\mathrm{N_xN_y}-1} \mathbf{\Psi}_q^{(0)}\mathbf{s}_q^{(0)} \\
& + \cdots + {\mathbf{\Phi}^{(0)}}^{-1} \sum_{\substack{p,q=0 \\ p\neq q}}^{\mathrm{N_xN_y}-1} \mathbf{\Psi}_q^{(R-1)}\mathbf{s}_q^{(R-1)}
\end{aligned}
\tag{3.6}
$$

Then (3.5) can be rewritten as:

$$
\mathbf{y} = \mathbf{\Phi}^{(0)}\left(\mathbf{s}^{(0)} + \mathbf{w}\right) + \mathbf{v} \tag{3.7}
$$

Defining the transformed subimage, $\breve{\mathbf{s}}^{(0)} = \mathbf{s}^{(0)} + \mathbf{w}$, then (3.7) becomes:

$$
\mathbf{y} = \mathbf{\Phi}^{(0)}\breve{\mathbf{s}}^{(0)} + \mathbf{v} \tag{3.8}
$$

Now only direct path information, $\mathbf{\Phi}^{(0)}$, is used to reconstruct the modified scene. Since the reconstructed scene contains some contributions from other multipath returns, then the reconstructed scene will be populated by ghosts. We hypothesize that by proper selection of radar apertures, the ghost locations can exhibit significant shift enough to identify them from genuine targets.

By making independent sets of measurements using under-sampling matrices $\mathbf{D}_i \in \{0,1\}^{J\times MN}$ with $J \ll MN$. The matrix $\mathbf{D}_i$ is known to obey restricted isometry property [51], [74]. The optimum length of the subaperture, lN, for a given compressed frequency set is a function of the number of targets, P and surrounding scatters, where l is the ratio of the selected radar locations. In TWRI applications, this number is unknown beforehand. However, it can be estimated prior to running the actual measurement [62].

$$J \geq CPR \log\left(\frac{N_x N_y}{PR}\right) \tag{3.9}$$

where C is a positive constant defined in CS literature. Down-sampling the given observation, gives:

$$\bar{\mathbf{y}}_i = \mathbf{D}_i \mathbf{\Phi}^{(\mathbf{0})}\, \check{\mathbf{s}}_i^{(\mathbf{0})} + \bar{\mathbf{v}}_i \tag{3.10}$$

where $\bar{\mathbf{v}}_i$ signifies the resulting noise vector, the product $\mathbf{D}_i\mathbf{\Phi}^{(\mathbf{0})}$ is the sensing matrix which will be discussed in the subsequent sections. The compressed measurements, $\bar{\mathbf{y}}_i$, are taken such that the corresponding subimages exhibit significant AD feature. It should be noted that in practical implementation of the CS based TWRI, the required measurements is directly acquired without down-sampling the full data volume.

To exploit the AD feature, the given array is divided into sub-arrays and their corresponding images are sparsely reconstructed and then strategically combined to get a final image. A careful increase in the number of subarrays may increases the quality of the final image with the expense of computational cost. To overcome the challenge, we suggest duo-subapeture imaging with careful image fusion strategies to ameliorate the efficiency of the proposed method. Two random subapertures, S_i, $i = 1,2$ are chosen from a linear array of N locations with interelement spacing of d units as shown in Figure 3-1:

$$S_1 = \left\{x: 1 \leq x \leq \left\lfloor \frac{N}{2} \right\rfloor \right\}$$

$$S_2 = \left\{x: \left\lceil \frac{N}{2} \right\rceil \leq x \leq N \right\} \tag{3.11}$$

$$|S_1| = |S_2| = lN$$

$|S_i|$ is the the number of locations in the i^{th}subarray and l denotes the ratio of the selected radar locations.

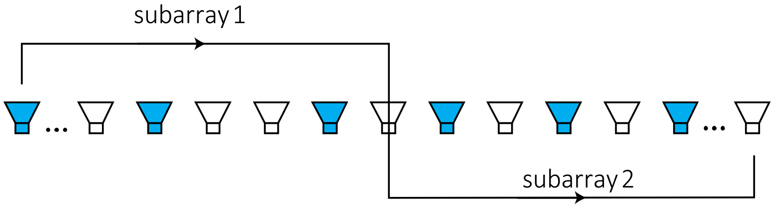

Figure 3-1: Subarrays selection.

The selected subaperture (colored in blue) are then used to design the sensing matrices for image sensing and reconstruction.

3.3.1. Rationale of Subarrays Selection

In the proposed ghost suppression method, the given array is subdivided into two halves with their centers separated by around $N/2$. However, it is desired to optimally decide the subarray separation to ensure maximum ghost suppression. To satisfy the desire, we perform correlation analysis of the received multipath signals at two different array locations. Consider two observation vectors, $\boldsymbol{y}_n$ and $\boldsymbol{y}_{n+k}$ when the subarrays are separated by kd units. It is hypothesized that the observed scenes will be different due to AD feature of the multipath contribution. From (3.10) we have:

$$\begin{aligned} \bar{\mathbf{y}}_n &= \mathbf{A}_n\, \check{\mathbf{s}}_n^{(0)} + \bar{\mathbf{v}}_n \\ \bar{\mathbf{y}}_{n+k} &= \mathbf{A}_{n+k}\, \check{\mathbf{s}}_{n+k}^{(0)} + \bar{\mathbf{v}}_{n+k} \end{aligned} \tag{3.12}$$

The correlation matrix, $\boldsymbol{R}_{\mathrm{n},n+k}$ with the assumption that the noise samples are uncorrelated with the scene is given by:

$$\begin{aligned} \boldsymbol{R}_{\mathrm{n},n+k} &= E\{\bar{\mathbf{y}}_n \bar{\mathbf{y}}_{n+k}^H\} \\ &= \mathbf{A}_n R_{s_n s_{n+k}} \mathbf{A}_{n+k}^H + E\left\{\mathbf{A}_n\, \check{\mathbf{s}}_n^{(0)} \bar{\mathbf{v}}_{n+k}^H\right\} + E\left\{\mathbf{A}_{n+k}\, \check{\mathbf{s}}_{\boldsymbol{n+k}}^{(\mathbf{0})\boldsymbol{H}} \bar{\mathbf{v}}_n\right\} \\ &+ \boldsymbol{R}_v = \mathbf{A}_n R_{s_n s_{n+k}} \mathbf{A}_{n+k}^H + \boldsymbol{R}_v \end{aligned} \tag{3.13}$$

$\boldsymbol{R}_{s_n s_{n+k}} = E\left\{\check{\mathbf{s}}_n^{(0)} \check{\mathbf{s}}_{n+k}^{(0)H}\right\}$; $\boldsymbol{R}_v = E\{\bar{\mathbf{v}}_n \bar{\mathbf{v}}_{n+k}^H\}$; $E\left\{\mathbf{A}_n\, \check{\mathbf{s}}_n^{(0)} \bar{\mathbf{v}}_{n+k}^H\right\} = E\left\{\bar{\mathbf{v}}_n \check{\mathbf{s}}_{n+k}^{(0)H} \mathbf{A}_{n+k}^H\right\} = \mathbf{0}$. We need the value of k that minimizes the number of non-zero elements in $\boldsymbol{R}_{s_n s_{n+k}}$. However,

$R_{\mathrm{n},n+k}$ is a function of the round trip delay which also depends on the target location and it is unknown in priori in TWRI applications. Hence, developing a closed form expression for the aperture separation is not feasible.

To overcome that challenge, a fairly exhaustive search of the acceptable subarray separation was conducted for random target locations placed in a $5 \times 5m^2$ room which conforms to most TWRI applications. An array of $2m$ long with 77 locations was deployed and subarray of $1m$ was used to scan the room as shown in Figure 3-2. In each run, a different target location was assumed and the corresponding image was captured. Figure 3-3(a) shows a sample of the selected target locations whereby only 10 were presented for clarity. The subarray was then linearly shifted along the crossrange direction and determine the cross-correlation between the current image vector, $\boldsymbol{s}_k$ and the initial image, $\boldsymbol{s}_0$. The normalized correlation value is given by:

$$\boldsymbol{R}_k = \frac{\boldsymbol{s}_k^H \boldsymbol{s}_0}{|\boldsymbol{s}_k||\boldsymbol{s}_0|} \tag{3.14}$$

The effective separation is determined when there is no significant change on the cross-correlation of the two images.

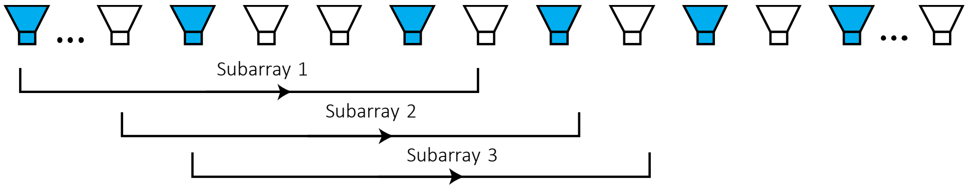

Figure 3-2: Subarray separation searching.

The sample representation of the results for different target locations are shown in Figure 3-3(b) where only five are displayed for clarity.

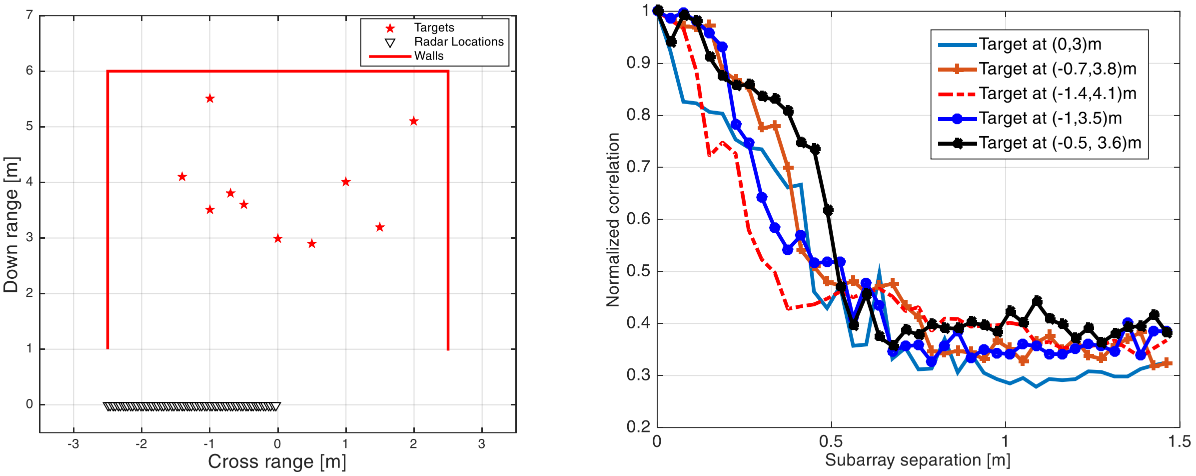

(a)

(b)

Figure 3-3: (a) scene with 10 random targets (b) normalized correlation for five targets.

It can be concluded from Figure 3-3 (b) that the AD effect is more pronounced when the target is closer to the radar as the normalized correlation converges to a constant value after fewer subarray shifts. It is evident from Figure 3-3(b) that the separation of $N/2$ may suffice. We repeated the experiment using different room dimensions and we arrived at similar conclusions. The selected subarrays are then used to design the sensing matrices for sensing and reconstructing the scene.

3.3.2. Sensing Matrix Design and Analysis

As explained earlier, the sensing matrix in TWRI can be viewed as the product of two matrices. The predefined matrix describing the signal propagation model which is a function of the radar parameters and the second matrix is down-sampling matrix, $\mathbf{D}$ which compresses the data volume. The matrix $\mathbf{D}$ is designed such that it compresses both the frequency and radar locations. It consists of randomly chosen rows from an identity matrix as in [60], [70], [75].

In CS theory, the sensing matrix plays an important role in the signal reconstruction process. To ensure the recoverability of the signal, the columns of the sensing matrix, $\mathbf{A}_i = \mathbf{D}_i \mathbf{\Phi}^{(0)}$ should have low correlation value.

To analyze the recoverability of the proposed sensing matrix, we evaluate its mutual coherence. The mutual coherence of the two columns is the normalized inner product between them, while the coherence of the matrix is the maximum absolute value of this inner product among all pairs of elements in the matrix [61], [62]:

$$\mu(\mathbf{A}) = \max_{i \neq j} \frac{\left| \boldsymbol{a}_i^H \boldsymbol{a}_j \right|}{\|\boldsymbol{a}_i\| \|\boldsymbol{a}_j\|} \tag{3.15}$$

The vector $\boldsymbol{a}_j$ specifies the j^{th} column of $\mathbf{A}$. When this metric returns a small value, it serves as sufficient condition to ensure sparse reconstruction. In classical algorithms, normalized mutual coherence may also provide useful information on the performance of the given array including resolution, noise and other interference robustness and ambiguity information [76].

The normalized mutual coherence of the sensing matrix for various undersampling ratios and two different image resolutions, averaged over 100 Monte Carlo runs, are summarized in

Table 3-1. The subarray based sensing matrix is compared with full array based sensing matrix. It is observed that the coherence increases with the image resolution. For the aforementioned subarray configuration, the normalized mutual coherence shows no significant change with data volume.

Table 3-1: Mutual coherence for full and subarray sensing matrices for two image resolutions

	Full array		Subarray	
Measurements (%)	32×32	64×64	32×32	64×64
6	0.469	0.812	0.783	0.941
12	0.432	0.802	0.786	0.945
25	0.418	0.795	0.782	0.941

Though, the coherence of the matrix is relatively high but better than the recently presented sensing matrices in TWRI literature [1]. It should be noted that the mutual coherence is only a sufficient but not necessary condition to ensure perfect reconstruction. Using simulated and experimental data, we attained a very good image quality with similar measurement matrices.

Figure 3-4 (a) shows a correlation of the representative column for image resolution of 32×32 pixels and Figure 3-4 (b) shows a correlation of a representative column for image resolution of 64×64 pixels when the undersampling ratio is 6%. The selected columns are column 500 for the case of 32×32 pixels and 2000 for the case of 64×64 pixels.

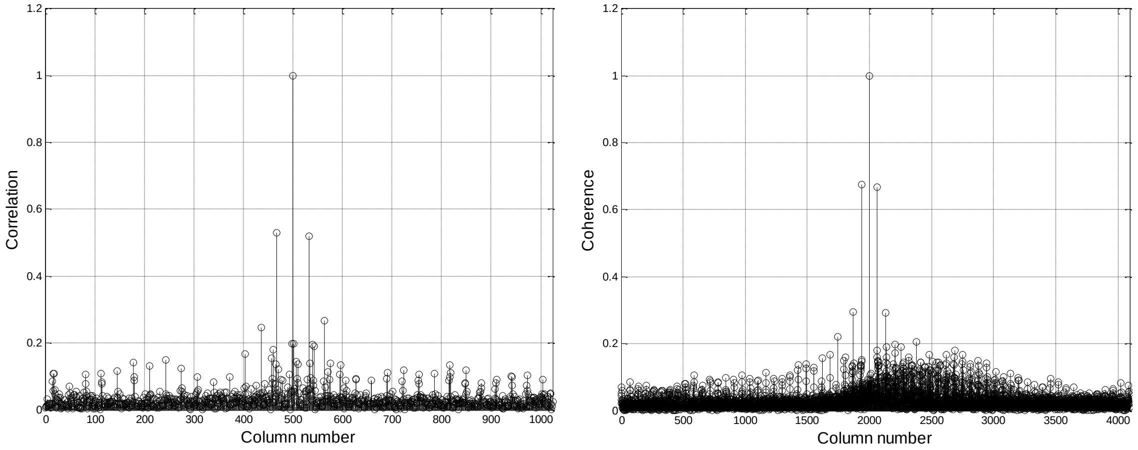

(a)

(b)

Figure 3-4: Sample correlation of the proposed sensing (a) 500th column with 32 × 32 pixels (b) 2000th column with 64 × 64 pixels.

3.3.3. Subimages Sparse Reconstruction

The modified subimage, $\check{\mathbf{s}}_i^{(0)}$, in (3.10) can be reconstructed sequentially using conventional CS approach [58], [59] or concurrently using parallel computing MATLAB toolbox to speed up the reconstruction process.

The reconstructed vectors, $\check{\mathbf{s}}_i^{(0)}$**,** are obtained by solving optimization problem [58], [59]:

$$\widetilde{\check{\mathbf{s}}_i^{(0)}} = \underset{\check{\mathbf{s}}_i^{(0)}}{\operatorname{argmin}} \left\| \check{\mathbf{s}}_i^{(0)} \right\|_1 \text{ s.t. } \left\| \bar{\mathbf{y}}_i - \mathbf{D}_i \mathbf{\Phi}^{(0)} \check{\mathbf{s}}_i^{(0)} \right\|_2 < \varepsilon \tag{3.16}$$

The choice of ε is a function of noise power [63]. To eliminate the effect of the ghosts exploiting AD feature, the reconstructed subimages are strategically fused to yield a final image.

3.3.4. Image Fusion Strategies

When multiple compressed subapertures are considered as in (3.10), then the corresponding ghosts for the respective subimages will reside at different locations following ghost AD feature. However, the locations of the true targets remain unchanged in all subimages. Thus, *masking* the subimages seems to be a natural solution to fuse the subimages. The overall image is obtained by pixel-wise multiplying the individual subimages [4], [11], [22].

Suppose there are L subimages with s_{lp} defines the image value at the p^{th} pixel corresponding to the l^{th} subimage, the overall image is obtained as:

$$s(p) = \prod_{l=1}^{L} \check{s}_{lp}^{(0)} \tag{3.17}$$

According to [22], masking sometimes tends to suppress or even eliminate the genuine targets. To alleviate that challenge, we propose strategic image fusions, *Additive-Multiplicative (AM) fusion*, which is a two-step process. In AM fusion, an intermediate image is first obtained as the strategic summation of the individual subimages as depicted in Figure 3-5. The summation is taken such that the magnitude of the true targets are preserved while minimizing the surrounding clutters. This helps to reduce the effect of the ghost and other clutters and hence increases TRCP at target locations. The intermediate image is then masked with the subimages to obtain the final image. In this work, we proposed two subimage fusion strategies to enhance the image quality:

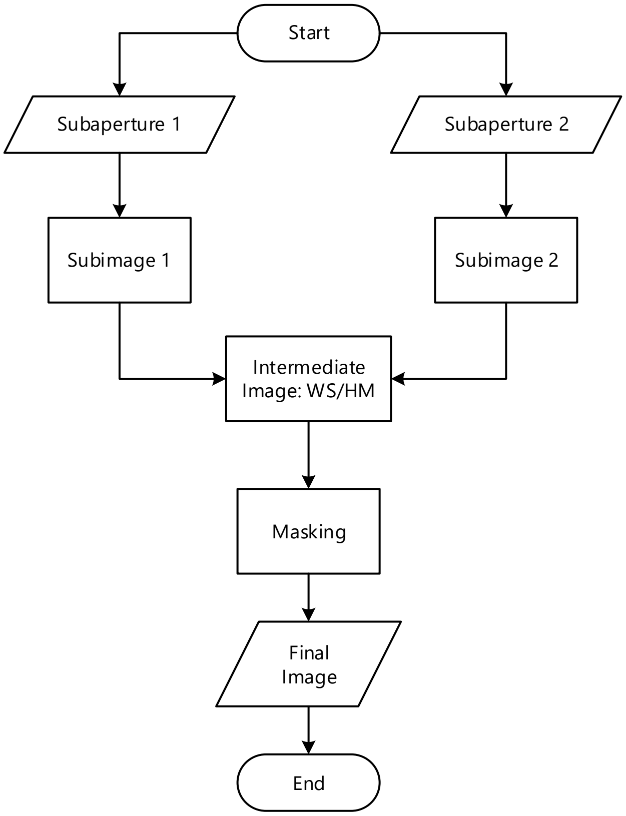

Figure 3-5: Image fusion methods flowchart.

A. *Weighted Sum Based Additive-Multiplicative Fusion (WSAM)*

In this case, the intermediate image is the weighted sum which minimizes the l_2-norm of the resulting image while maintains the magnitudes of the true targets. Consider L subimages, $\check{\mathbf{s}}_1^{(0)}, \check{\mathbf{s}}_2^{(0)} \dots \check{\mathbf{s}}_L^{(0)}$ reconstructed from L compressed apertures. Their weighted sum is given by:

$$s_W(p) = \sum_{l}^{L} \alpha_l \check{s}_l^{(0)}(p) \tag{3.18}$$

where $\alpha_l \in \mathbb{R}: 0 \leq \alpha_l \leq 1$. The values of α_l which result in a minimum norm are obtained using:

$$\min\left\|\alpha_1\check{\mathbf{s}}_1^{(0)} + \cdots + \alpha_L\check{\mathbf{s}}_L^{(0)}\right\| \text{ subject to } \sum_{l=1}^{L}\alpha_l = 1 \tag{3.19}$$

B. Harmonic Mean Based Additive-Multiplicative Fusion (HMAM)

The fact that harmonic mean of a list of numbers leans towards the least elements of the list while maintains the same value for equal elements, can be utilized to suppress large clutters in TWRI while it maintains the true targets. For L subimages, $\check{\mathbf{s}}_1^{(0)}, \check{\mathbf{s}}_2^{(0)} \ldots \check{\mathbf{s}}_L^{(0)}$ reconstructed from L compressed subapertures, the intermediate image, $\boldsymbol{s}_H$, is defined as the harmonic mean of the corresponding subimages and is given by:

$$s_H(p) = \frac{L}{\sum_{l=1}^{L}\frac{1}{\check{s}_l^{(0)}(p)}} \tag{3.20}$$

The overall image is obtained by masking the intermediate image with subimages as shown in Figure 3-5.

The WSAM approach is relatively immune in case when a target of interest is not well visible from one subaperture. If it is possible to establish the probability of target detection, γ, in the presence of clutters and noise, then the problem resembles to that of multi-scan for surveillance radar operations [49]. For duo-subaperture imaging, if the probability of detection, γ, of the target in the presence of clutter and noise is known then, the probability of detecting a target at a given pixel in one of the two images and it is given by $2\gamma - \gamma^2$.

3.4.Results and Discussion

In this section we present results based on MATLAB simulation and experimental data. In the simulation part, four scenarios detailed in the next subsection were implemented to evaluate the effectiveness of the proposed ghost suppression method. For the experimental part, an experiment was setup in KFUPM-EE building for real data collection.

3.4.1. Simulation Results

In this subsection we present results based on MATLAB simulations for four different possible scenarios to evaluate the effectiveness of the proposed suppression method under different data reduction modalities and radar configurations as summarized in Figure 3-6. The first two using MVM configuration and the remaining two with SVB with and without front wall mitigation.

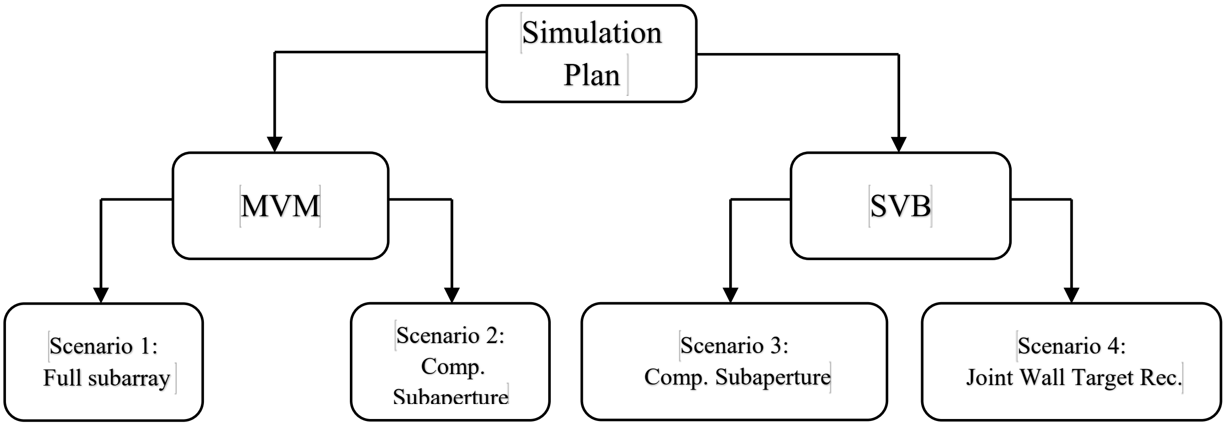

Figure 3-6: Organization of the simulated results.

A TWRI system was simulated using MATLAB®. For comparison, we adopt simulation parameters and setup as in [1]. The left and right sidewalls of the room are at crossrange of $-1.8m$ and $4m$, respectively, while the back wall resides at $6.37m$ downrange. A uniform linear monostatic array composed of 77-elements spaced out by 1.9cm is used to capture the image. The center of the array is taken to be the origin of the system. The front wall parallel to the array is at $2.44m$ downrange with thickness $d = 20cm$ and relative permittivity, $\varepsilon_r = 7.67$. A series of 201 monochromatic waves to realize a UWB signal occupying a spectrum between 1 and $3GHz$ is employed for the scene interrogation.

In this work, we denote partial path as a path from the radar to the target or vice versa. During simulation, a total of six multipath returns were considered whereby one partial path is always the direct path and the second partial path corresponds to: direct, back wall return, left side wall return, right side wall return and the wall reverberation multipath. Also, a return due to the target interaction was taken into account. We assumed all side walls to be perfect reflectors with reflectivity of one. When they are not perfect reflectors, then ghost targets will have less power and hence, becomes relatively easy to be suppressed. Targets located at $(0.31, 3.6)m$ and $(-0.62, 5.2)m$ were considered which are unknown to the receiver. White noise of 0dB SNR was added to the simulated measurements. The DSBF based images utilizing full available measurement using MVM and SVB configurations were obtained for comparison as shown if Figure 3-7. For the SVB configuration, the transmitter is fixed at $2m$ along crossrange and the receiver follows the MVM counterpart. In the case of CS reconstructions, we used only 10% of the total measurement to reconstruct the corresponding images using Yall1 algorithm [73].

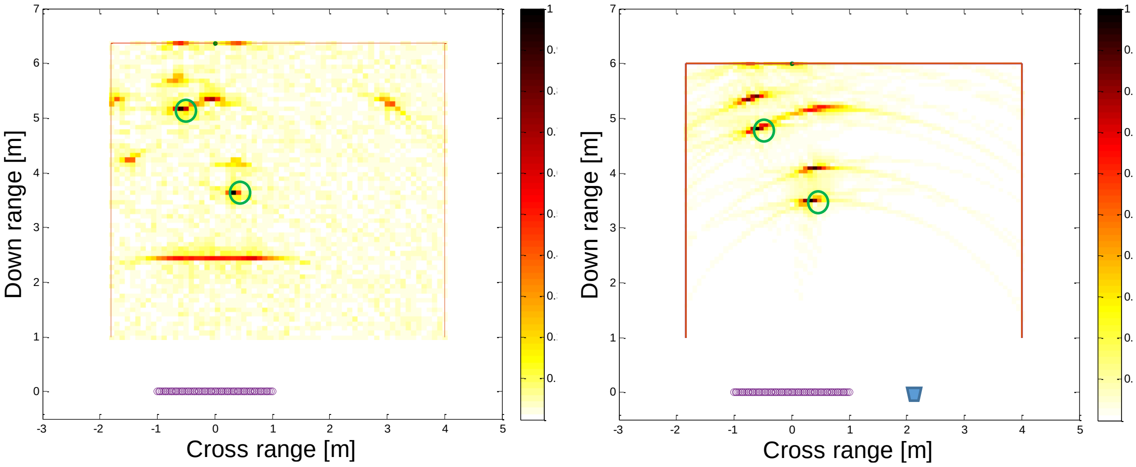

(a) (b)

Figure 3-7: DSBF images (a) MVM (b) SVB configurations.

Duo-subarray with length $N/2$ is considered, a fraction of the radar positions and frequency bins are selected from the two subarrays for sparse image reconstruction. Four scenarios are evaluated in this section: taking the whole subarray with reduced frequency bins, compressed subapertures with MVM configuration, compressed subapertures with SVB and joint reconstruction of the wall and targets as summarized in Figure 3-6.

A. Scenario 1: Whole Subarrays

In this case, we used only one-fifth of the frequency bins randomly selected and the same set is transmitted at each location of the given subarray. The radar locations represent one-half of the total available locations which makes the compressed measurement 10% of the total data volume. The subarray images are depicted in Figure 3-8 (a)-(b). The image quality using CS reconstruction is better than DSBF in spite of using entire measurement set. To obtain the final images, the two subimages were combined using proposed image combining techniques: WSAM fusion and HMAM fusion and are shown in Figure 3-8 (d)-(f). In Figure 3-8 (d) is the final image using conventional masking for performance comparison. It is evident from Figure 3-8 that the proposed fusion strategies outperform the conventional masking.

In the case of WSAM fusion, the intermediate image takes 54% and 46% of the intensity of first and second subimage, respectively, to minimize the clutter norm while maintaining the intensities of the true targets. The proposed image fusion techniques seem to have comparable performance and since the WSAM ensures the minimum clutter norm it is therefore, preferred in practice and will be used to evaluate the final images in the coming scenarios.

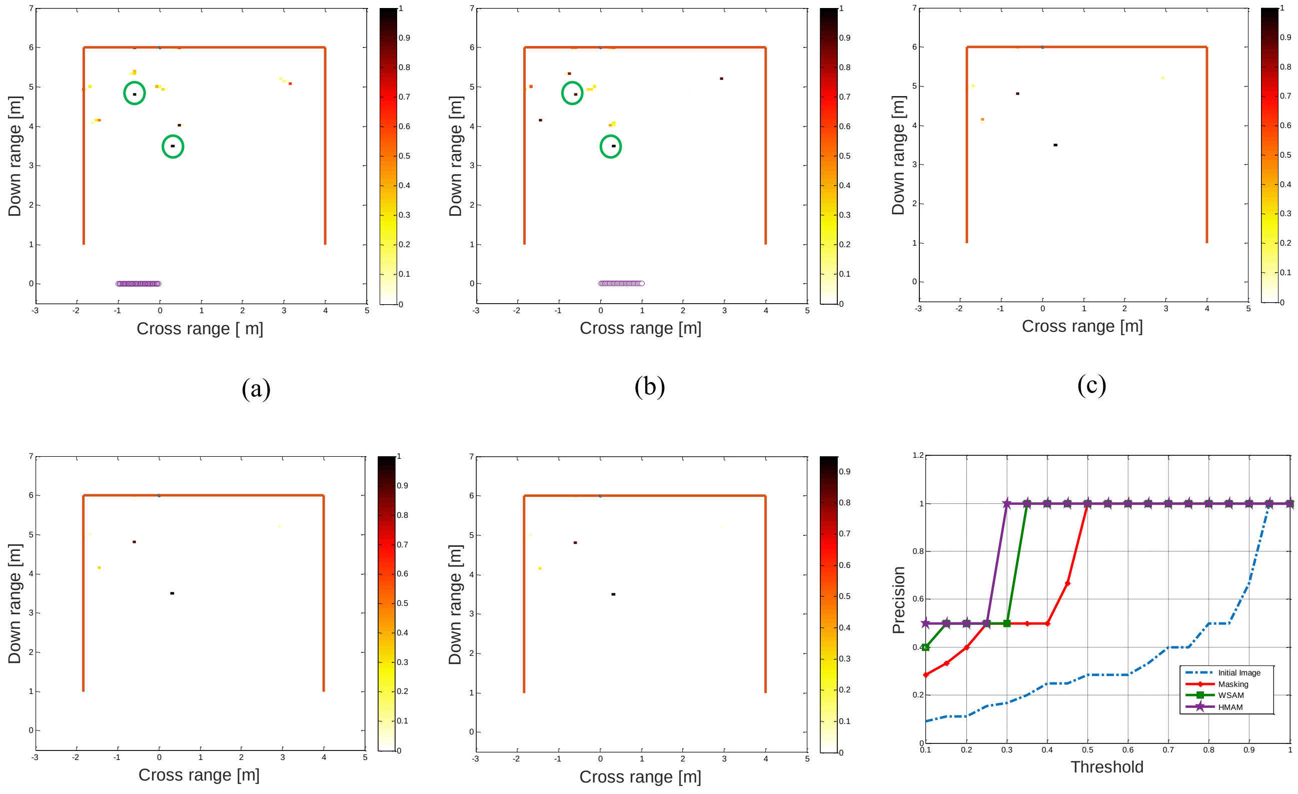

(a) (b) (c)

(d) (e) (f)

Figure 3-8: Images with random frequency: (a) subarray1 (b) subarray2 (c) final with masking (d) final with WSAM 54% by 46% (e) final with HMAM (f) precision.

To analyze the power of sparse reconstruction over DSBF, we generated DSBF images with the same reduced data volume as shown in Figure 3-9. Apparently from Figure 3-9 (c), DSBF showed inability to incorporate the AD feature for ghost suppression under reduced measurement owing to its lower resolution caused by point spread function. Further, it suffers from increased level of unwanted clutters due to the violation on the required antenna spacing and therefore, will not be compared in the proceeding results.

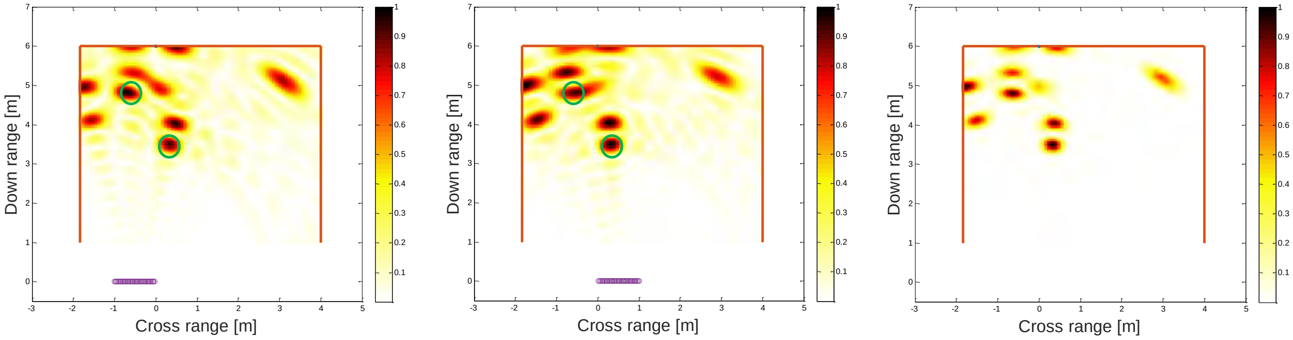

(a) (b) (c)

Figure 3-9: DSBF images (a) subarray1 (b) subarray2 (c) masking.

Using quantitative measures, we evaluate TSCR and TRCP and are summarized in the Table 3-2. For target detection capability, the precisions of this scenario in demonstrated in Figure 3-8 (f).

Table 3-2: TSCR and TRCP [dB] for scenario 1

	TSCR [dB]	**TRCP [dB]**
Initial image	57.4	0.8
Masking	72.3	6.7
WSAM	76.5	9.7
HMAM	78.0	10.5

From Table 3-2 and Figure 3-8 (f), the final images aided by the proposed fusion techniques can dramatically attenuate the effect of the multipath ghosts. Only a threshold value of around 30% can be used to isolate true targets from the surrounding clutters.

B. Scenario 2: Compressed Subapertures with MVM Configuration

In this case, one-fifth of the radar locations were randomly selected from the given subarrays and one-half of the frequency bins were randomly chosen and the same set is transmitted at each selected location for design simplicity. Also, transmitting the same frequency bins across the array allows smooth front wall mitigation which is otherwise becomes tricky. The advantage of using different frequency set is the flexibility to combat the jamming effect across the array. However, given the length of the practical aperture in TWRI, the effect can be neglected.

The subaperture images are depicted in Figure 3-10 (a) and (b) and their corresponding final image generated with WSAM fusion is depicted in Figure 3-10 (c). In WSAM, the fusion assumes 58% of the first subimage and 42% of the first second to effectively suppress the ghosts.

In Figure 3-10 (c), the final image suppresses the multipath ghosts significantly and genuine targets can be clearly detected. This observation is supported by numerical analysis using TSCR and TRCP which show relatively good values enough to detect the targets as summarize in Table 3-3.

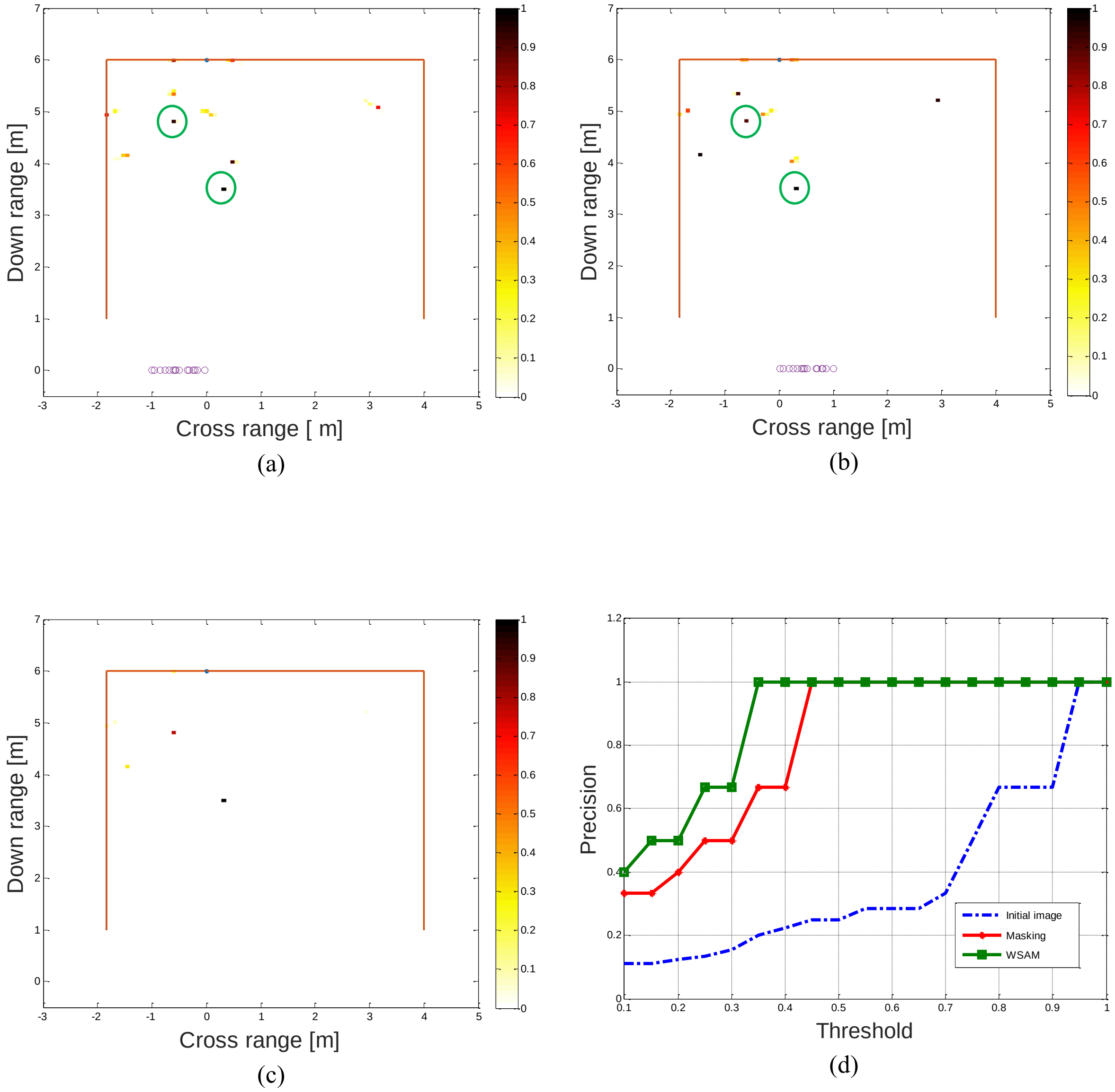

(a) (b) (c) (d)

Figure 3-10: Images for scenario 2 (a) subaperture1 (b) subaperture2 (c) final with WSAM 58% by 42% (d) precision.

The precision curves, which dictate the probability of correct detection are plotted against the threshold values is shown in Figure 3-10 (d). The threshold of around 35% can correctly eradicate the surrounding clutters including ghosts

Table 3-3: TSCR and TRCP [dB] for scenario 2

	TSCR [dB]	**TRCP [dB]**
Initial image	57.7	1.0
Masking	72.4	6.7
WSAM	76.7	10.1

C. Scenario 3: Compressed Subapertures with SVB Configuration

In the above setups, we considered MVM configuration. In this scenario we investigate the effect of SVB configuration. The transmitter is fixed and the receiver locations are randomly selected from the two compressed receiver locations. The corresponding subimages are shown in Figure 3-11 (a)-(b) and the corresponding final image with WSAM is depicted in Figure 3-11 (c) with its quality metrics summarized in Table 3-4.

The precision curves, which compares the number of true targets and the total number of available targets are shown in Figure 3-11 (d). It is noted in Figure 3-11 (d) that the threshold of 15 % suffices as detection threshold with masking. This scenario shows a noticeable increase in the image quality compared to its corresponding MVM counterpart. This is due to the geometrical changing which in turn makes the AD effect more pronounced and also locating some ghost targets outside the area of interest. Numerical values of TSCR and TRCP for this scenario are summarized in Table 3-4.

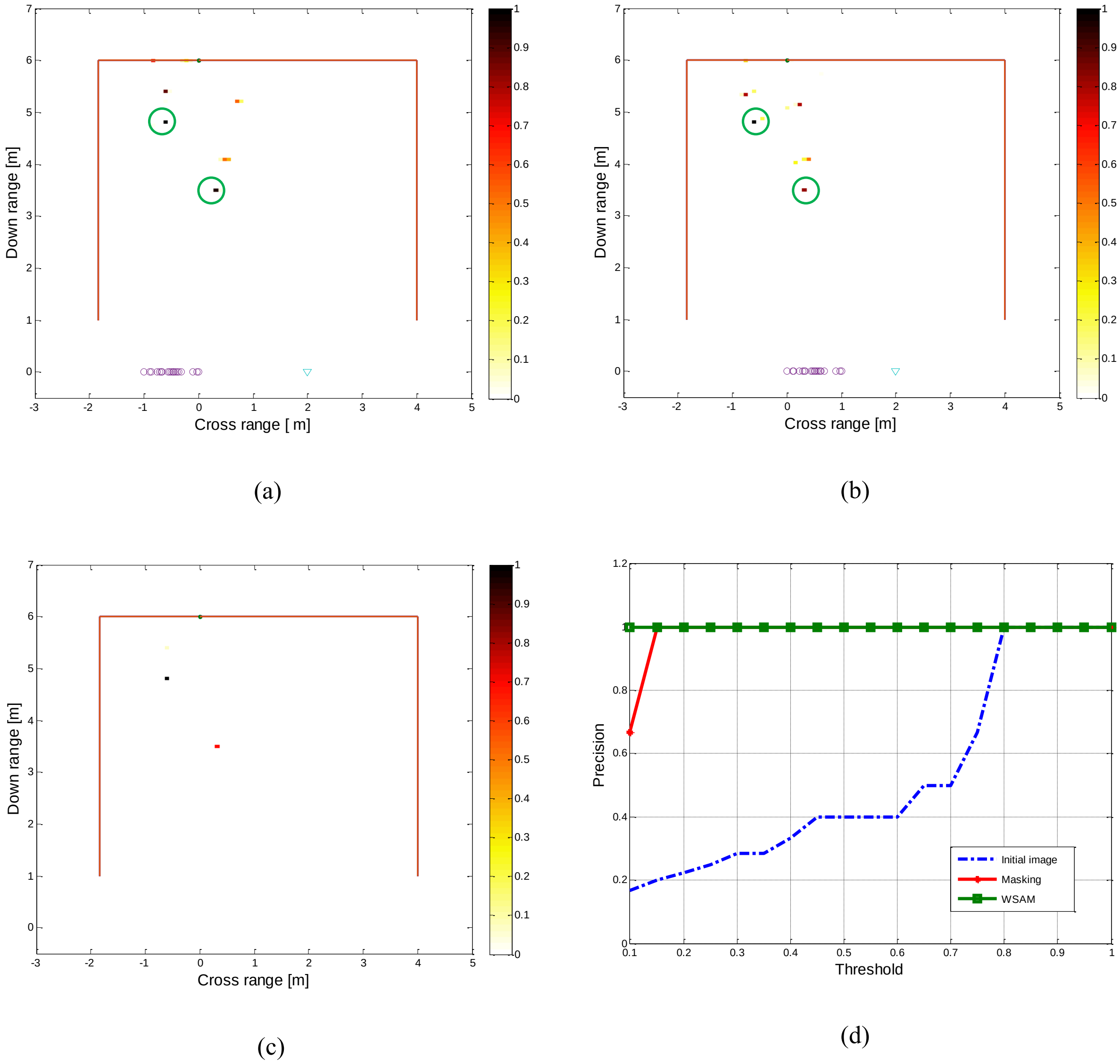

(a) (b) (c) (d)

Figure 3-11: Images using SVB for scenario 3 (a) subaperture1 (b) subaperture2 (c) final with WSAM 44% by 56% (d) precision.

Table 3-4: TSCR and TRCP [dB] for scenario 3

	TSCR [dB]	**TRCP [dB]**
Initial image	62.7	2.0
Masking	89.5	16.9
WSAM	97.3	23.7

D. Scenario 4: Joint Wall-Target Reconstruction with SVB

Using duo-subaperture we can jointly reconstruct the targets and the front wall. This is made possible because in duo-subaperture imaging, only one-half of the array is considered during image reconstruction which reduces the wall clutter significantly. Also, sub-wall images in the corresponding subimages reside in different pixels which naturally suppress its effect and enhance TSCR and TRCP at target locations. The final image restores the intensities of the true targets and the wall is masked out as shown in Figure 3-12.

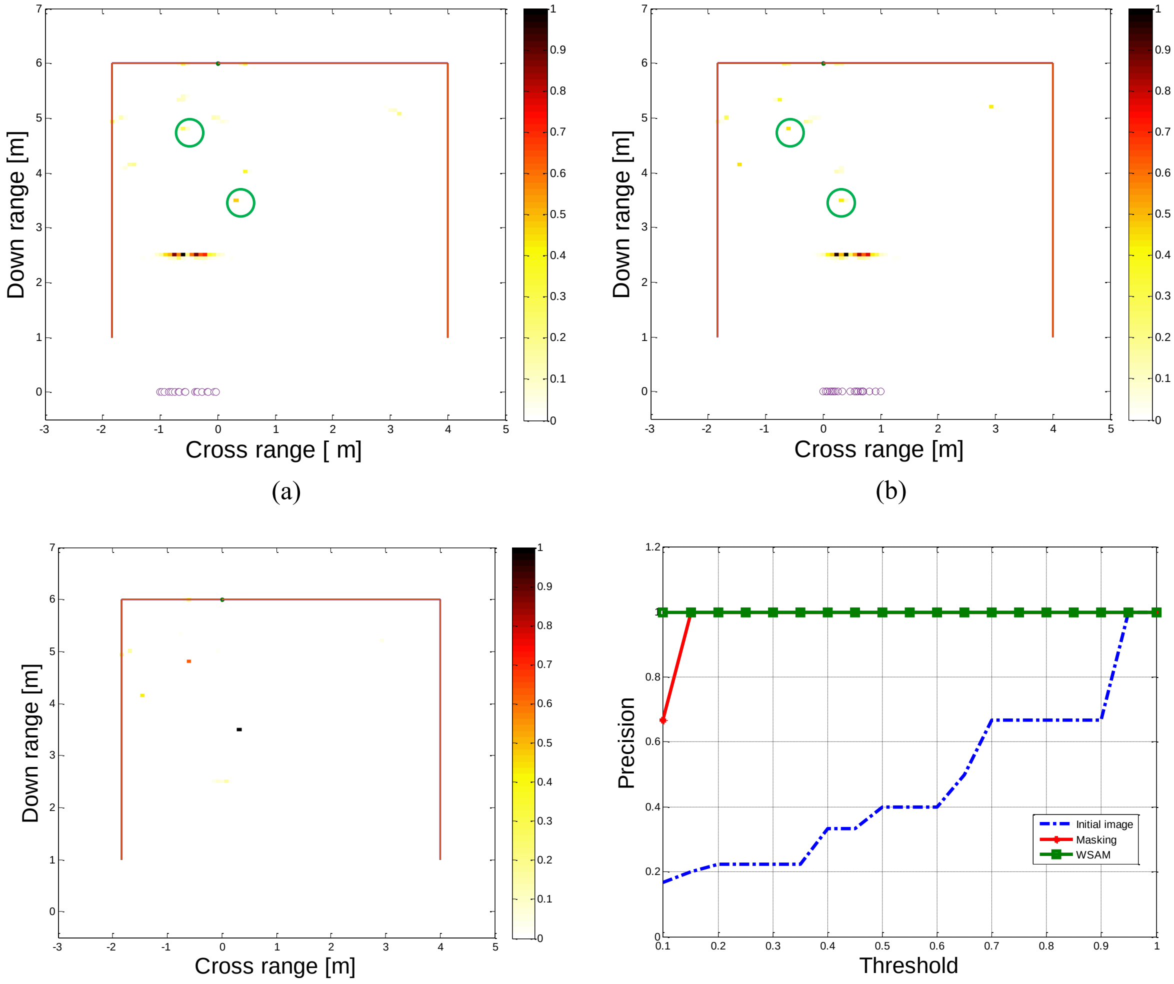

(a) (b)

(c) (d)

Figure 3-12: Images using SVB for scenario 4 (a) subaperture1 (b) subaperture2 (c) final with WSAM (d) precision.

The precision in Figure 3-12 (d) demonstrates the effectiveness of the method without wall mitigation. Certainly, the cost of wall mitigation has been reduced however, the measurement volume might increase as the scene becomes less sparse. With WSAM fusion, threshold of less than 10% is sufficient to identify the true targets.

From the simulated scenarios, the proposed method can effectively suppress multipath ghosts. In the next sub-section, the real experimental data is used to evaluate the effectiveness of the method.

3.4.2. Experimental Results

A. Experimental Setup

A wideband SAR system was set up in a semi-controlled room at KFUPM-EE department for multipath analysis to validate the proposed ghost suppression method, a schematic sketch of the room is shown in Figure 3-13. The moving platform is controlled by a microcontroller system which receives commands from the PC via Bluetooth as demonstrated using block diagrams in Figure 3-14. Operational parameters were selected such that they conform to the recently published works [1], [48]. A SAR was deployed to cover 67 equally spaced locations with an inter-element spacing of 2.5cm along the x-axis. A stepped frequency signal occupying a spectrum between 1 and 3GHz with 201 frequency points was used for scene interrogation. This allows a range resolution of 7.5cm with maximum unambiguous range of $15m$. The background information was first captured for clutter mitigation including the front wall. Two metallic cylinders were placed at $(-0.75, 2)\ m$ and $(0.5, 3)\ m$ as shown in the setup and room layout given by Figure 3-13 with the origin taken at the center of the aperture. The room has two protruding corners of reinforced concrete pillars near the back side. The imaged region is chosen to be $4 \times 5m^2$.

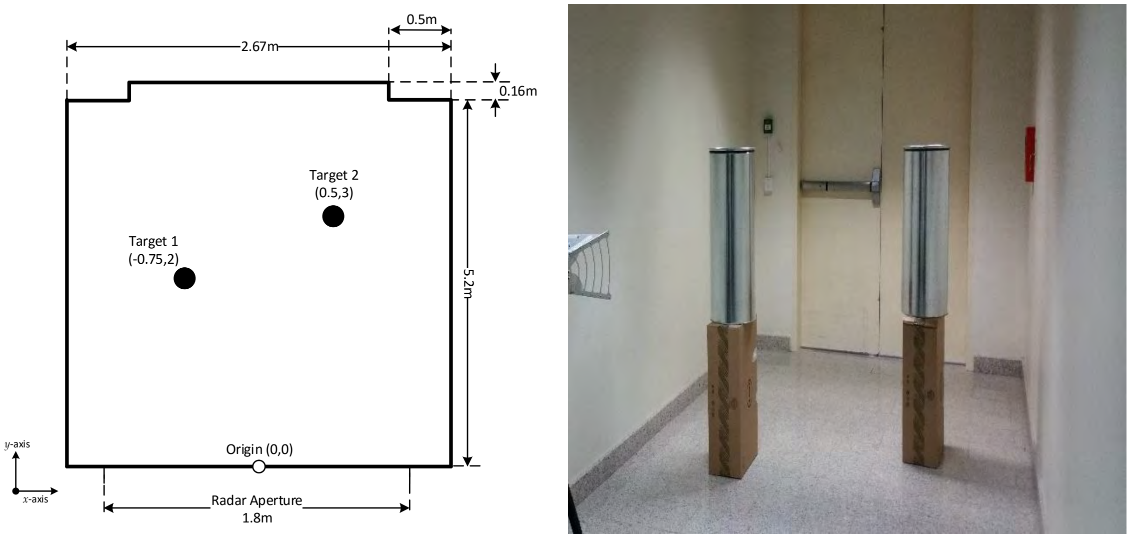

(a) (b)

Figure 3-13: The scene (a) room layout (b) experimental setup.

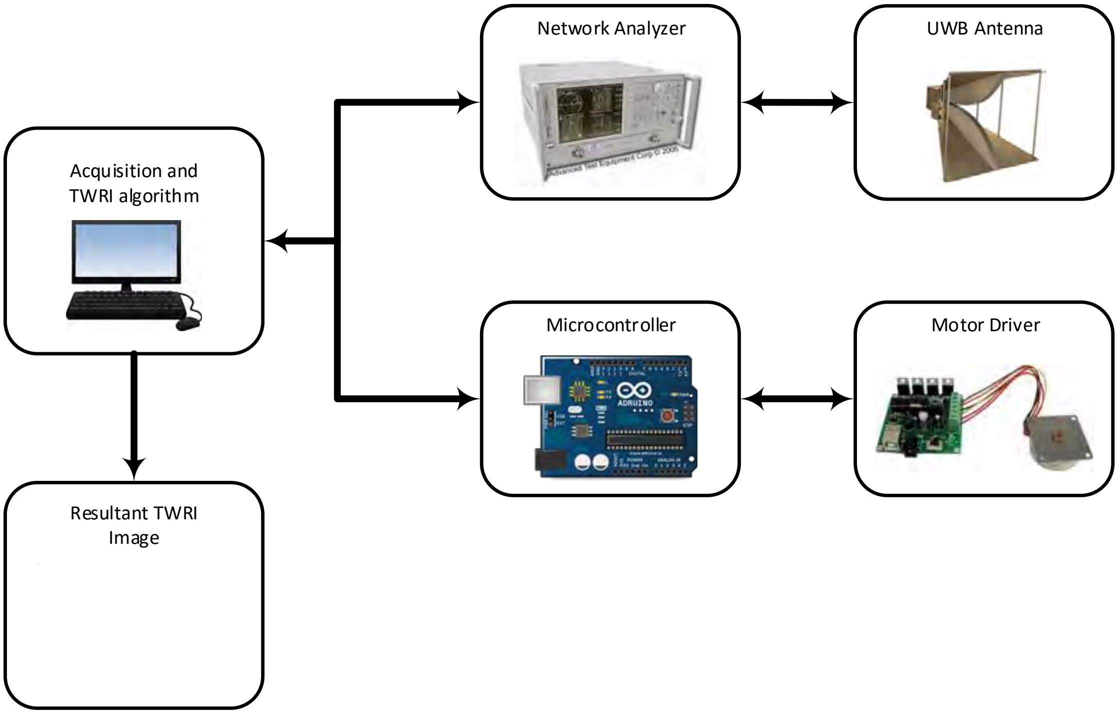

Figure 3-14: Radar imaging system layout.

The image generated using DSBF with full data volume and CS using 12.5% of the data volume show the effect of multipath ghosts as depicted in Figure 3-15, which need to be suppressed for correct scene interpretation.

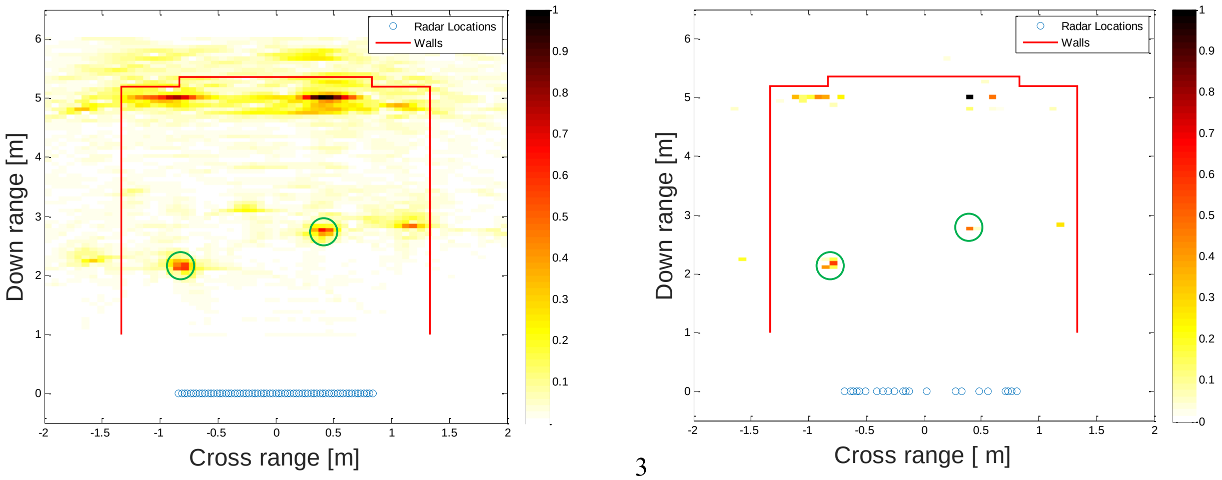

(a)

(b)

Figure 3-15: Images (a) DSBF with full data volume (b) CS reconstruction with 12.5% data volume.

B. Multipath Ghost Suppression

Again, we considered duo-subaperture in which one-fourth of the frequency were randomly transmitted and only one-half of the radar locations randomly chosen from the given array. The final image is obtained using WSAM fusion which shows significant ghost reduction with all true targets correctly reconstructed despite the directivity challenge of the horn antenna as shown in Figure 3-16. This observation alludes that in real application, the subapertures need to be carefully chosen otherwise some real targets might be invisible by the radar system. Quantitative performance measures, TSCR and TRCP summarized in Table 3-5 indicate the effectiveness of the suppression method.

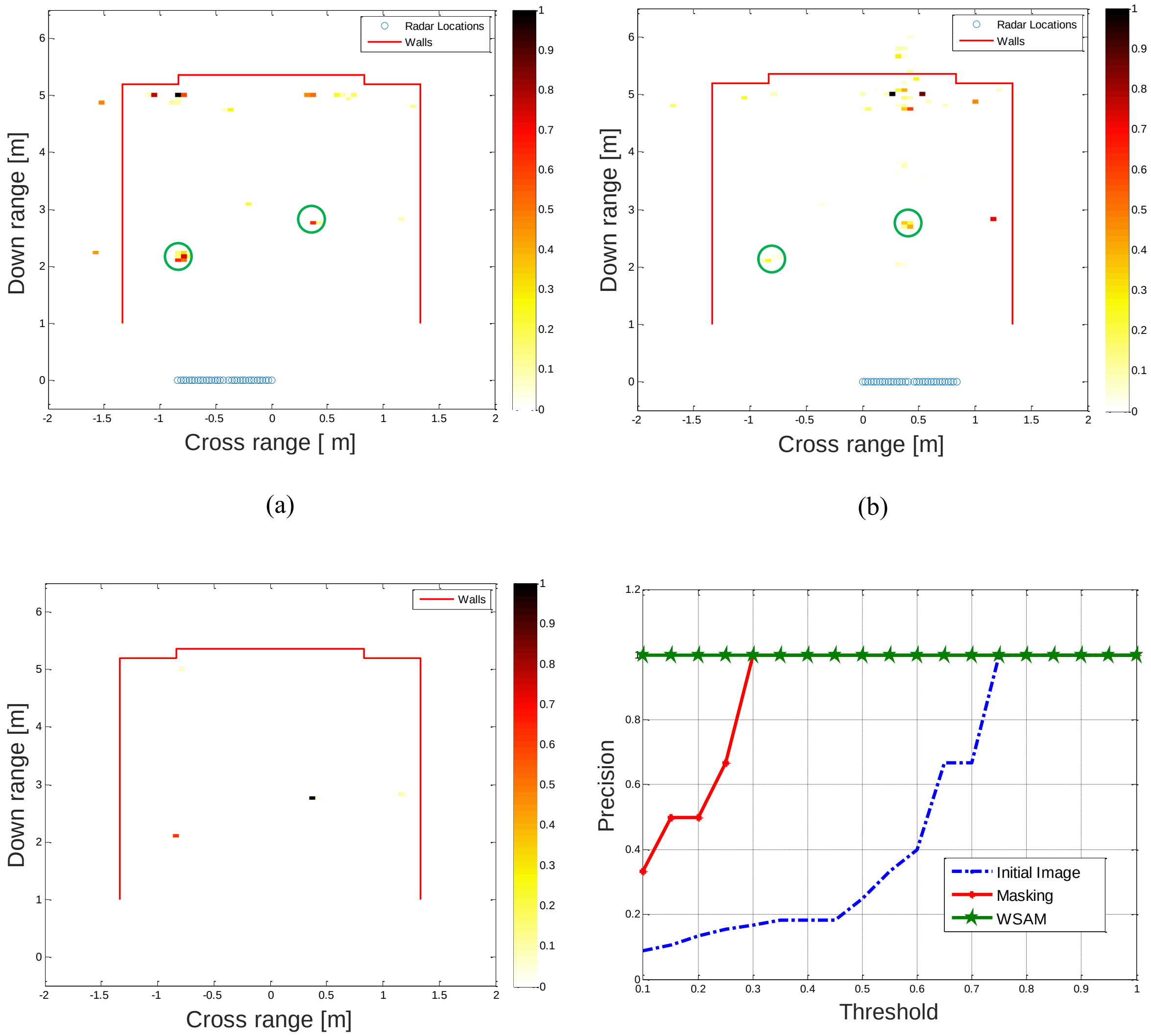

(a) (b)

(c) (d)

Figure 3-16: Images (a) subaperture1 (b) subaperture2 (c) final with WSAM (d) precision.

The target detectability using precision was also analyzed. Precision gives a good indication of how well is the method by comparing the expected number of targets and the number of reconstructed targets. The unit precision means the number of targets in the final image is exactly the same as the expected. The variation of the precision value with the possible threshold is given in the precision curves in Figure 3-16 (d).

Table 3-5: TSCR and TRCP [dB] for real experimental data

	TSCR [dB]	**TRCP [dB]**
Initial image	57.5	2.6
Masking	77.6	10.9
HMAM	88.0	20.2

3.4.3. Comparison with the Related Works

Comparing with recently published works, our method shows satisfactory tradeoff between image quality improvement and complexity reduction. In [22], the authors achieved optimal tradeoff between improvement factor (IF) of 24.29dB and target improvement factor (TIF) of 0.29dB when using single view multistatic radar with multiplicative/additive fusion of seven subarray images. This is due to point spread function in DSBF algorithm which significantly lower its resolution. Besides, the images using DSBF suffers from increased level of unwanted clutters. This work, which employed compressed duo-subarray under CS framework achieved 34.6dB of IF and 21.7dB of the TIF utilizing only around 6% of the total measurement. Moreover, unlike in [22] where the authors tackled only multipath ghosts due to target interactions, this work considered multipath due to side walls and front wall reverberation as well.

In [1], the authors achieved the best suppression with non-overlapping group sparse approach. It returned TSCR and TRCP of 95.0dB and 25.0dB, respectively, with only 3% of the total measurement. With nearly equal volume, the proposed work achieved 97.3dB and 23.7dB of the same metrics using WSAM image fusion strategy. In addition to front wall and side wall reflection considered in [1], the proposed approach considered target-to-target interaction as well which gives additional credit.

3.5.Conclusion

The chapter presented the formulation and analysis of the ghost suppression method exploiting AD feature using duo-subapterure. The recoverability of the sensing matrix has been investigated for different image resolutions. The method has been scrutinized under different possible scenarios using MATLAB simulation and real measurements and it bodes well in view of effectiveness and design simplicity as compared to recent findings. The proposed subarray selection has two inherent challenges; limited subaperture length which may results to miss genuine targets when using directional antennas and the second is the performance instability due to the random selection of the radar locations. The randomness on the other hand is preferred by CS algorithms. Additionally, the effectiveness of the AD based method depends on the selection of the radar locations and configuration of the arrays as well. To overcome the said challenges, we proposed sparse arrays based on Pythogorean triple coprime numbers to ensure nearly constant performance with increased crossrange resolution and design simplicity. In the subsequent chapter, the design and analysis of the sparse arrays based on coprime numbers will be introduced.

3.6.List of Publications

1. A. T. Abdalla, A. H. Muqaibel, S. Al-Dharrab, “Aspect dependent multipath ghost suppression in TWRI under compressive sensing framework” ICCSPA’15, Sharjah UAE, 2015.

2. A. T. Abdalla and A. H. Muqaibel, “Multiple Target Sparse Reconstruction in TWRI Utilizing Ghost’s Aspect Dependence Feature”, in 2015 IEEE International RF and Microwave Conference (RFM 2015), Kuching, Malaysia.
3. A. T. Abdalla and A. H. Muqaibel, “Single-View Bistatic Sparse Reconstruction in TWRI Exploiting Ghost’s Aspect Dependence Feature”, in 2016 IEEE Wireless Communications and Networking Conference (IEEE WCNC2016), Doha, Qatar.
4. A. H. Muqaibel, A. T. Abdalla, Mohammad T. Alkhodary, S. Al-Dharrab, “Aspect dependent efficient multipath ghost suppression in TWRI with compressive sensing” Journal of Radioengineering. Submitted

"Innovation comes about through combining disparate ideas and disciplines in ways that seem weird at first. Get comfortable with weird if you want real innovation to emerge"

Ben Weinlick

CHAPTER 4

PYTHAGOREAN TRIPLE COPRIME-BASED APERTURES WITH SPARSE RECONSTRUCTION IN TWRI

4.1.Introduction

In this chapter, we propose new sparse array configurations using Pythagorean triple coprime integers. If three integers N_1, N_2 and N_3 form a Primitive Pythagorean Triple (PPT), then they are pairwise coprime. An interesting property of such triple is that their squares are also pairwise coprime which helps to manipulate the subapertures dimensions. This may ensures a fair tradeoff between the minimum required number of measurements by CS reconstruction algorithms and the maximum practical aperture length. We suggest two Pythagorean subarrays and evaluate their performance in two different imaging modes: duo-subarray imaging using the proposed subarrays followed by image fusion; and combining subarrays before imaging. In both cases, we consider three combinational modes namely Pythagorean-based Interlaced Sub-Apertures (PISA), Pythagorean-based Displaced Sub-Apertures (PDSA) and Spatial Orthogonal Coprime Arrays (SOCA).

Results based on MATLAB simulation and electromagnetic simulator software show good TSCR and TRCP improvements, and of course, the performance stability is a major supplement to the random subaperture counterpart.

The rest of the chapter is organized as follows: Section 4.2 review the literature on coprime-based arrays. Section 4.3 presents the prototype coprime array structure. Section 4.4 presents the proposed sparse subarrays based on PPT and aperture gain is given in this Section. Section 4.5 evaluates the recoverability of the sensing matrices using the designed subarrays. Section 4.6 presents subarrays configurations using the designed subarrays. In Section 4.7, the results based on MATLAB simulation and electromagnetic propagation software are presented and Section 4.8 summarizes the chapter.

4.2. Literature Review

The effectiveness of the ghost suppression method based on AD feature is determined by the choice of the subapertures. The subapertures are selected such that the resulting images show sufficient ghost shift which makes them identifiable. Different array configurations have been proposed recently aiming at improving the suppression performance [4], [6], [13], [22], [55], [61] as elaborated in Chapter 1.

Recently, coprime based arrays have been proposed in direction of arrival (DOA) estimation and maritime radar applications which offer attractive alternatives for sparse array construction [76]–[80]. Among its attractive features is its simplicity and data reduction capability. The “prototype” coprime array was presented in [76] and its derivatives: extending the number of elements; and arrays displacement followed in subsequent contributions[78], [79]. In [80], the authors employed coprime arrays in maritime imaging to reduce data volume and to increase the range swath.

In some applications, the half-wavelength requirement for the minimum spacing is impractical due to the antenna size, think of parabola antennas. Such example and others make the prototype coprime array not the best candidate. Recently, extensions of the prototype coprime structure have been reported including Coprime Array with Compressed Interelement Spacing (CACIS), Coprime Array with Displaced Subapertures (CADiS) [79] and CADiS which maintains a large interelement spacing but have a small and consecutive equivalent spacing [78]. However, an interesting extension in view of TWRI exploiting AD feature of the multipath ghosts is the coprime array with displaced subapertures (CADiS) as elaborated in [79] and depicted in Figure 4-1. The resulting array allows much larger effective aperture and hence gives high crossrange resolution. In this structure, the two basic arrays are collinearly located with the closest spacing, $R \geq \min\{N_1, N_2\}$.

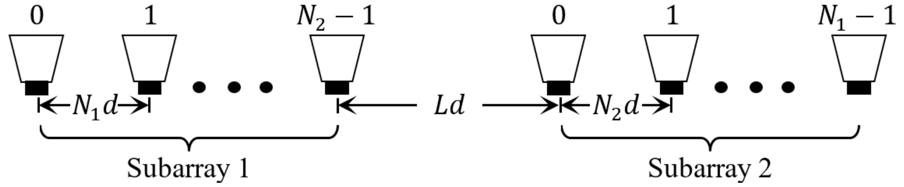

Figure 4-1: Coprime array with displacement.

The challenges with the existing arrays if applied to TWRI is the tradeoff between the minimum number of antenna required to correctly reconstruct the image and the feasible aperture length. To address the challenges we suggest the use of Pythagorean triples coprime based arrays which can tradeoff the two quantities.

Currently, the coprime array is topical in DOA estimation problems due to its design simplicity and inherent sparse structure. It has been successfully employed to increase the Degree of Freedom (DoF) which then increases the number of localized sources [76], [78]–[85]. This can be extended to TWRI as we can get the highest degree of multipath resolvability and hence ghost suppression. Due to the nature of the imaging problems where long arrays are desired, Pythagorean based coprime configurations are proposed. To the best of our knowledge, coprime based configuration in TWRI applications under multipath environment has not been studied yet and Pythagorean triples were never used.

4.3.Coprime Arrays

Two natural numbers, N_1 and N_2 are said to be relatively prime or coprime if $\gcd(n^{N_1}-1, n^{N_2}-1\,) = n^{\gcd(N_1,N_2)}, n > 1$ where the gcd stands for greatest common divisor [86], [87]. The basic coprime array structure is presented in [76], [79] and the references therein, which is referred to as prototype coprime array. It contains two uniform subarrays, whereby one comprises of N_1 sensors with the elements spaced by N_2 units, while the other employs N_2 elements with the spacing of N_1 units between consecutive elements as shown in Figure 4-2. The element spacing, d, in both cases is fixed to $\lambda/2$ which is essential to avoid grating lobes artifacts. The sensor locations are defined according to the following set:

$$X = \{N_1 nd | 0 \leq n \leq N_2 - 1\} \cup \{N_2 md | 0 \leq m \leq N_1 - 1\} \qquad (4\text{-}1)$$

The cardinality of the set X is $N_1 + N_2 - 1$, which signifies the total available sensor locations.

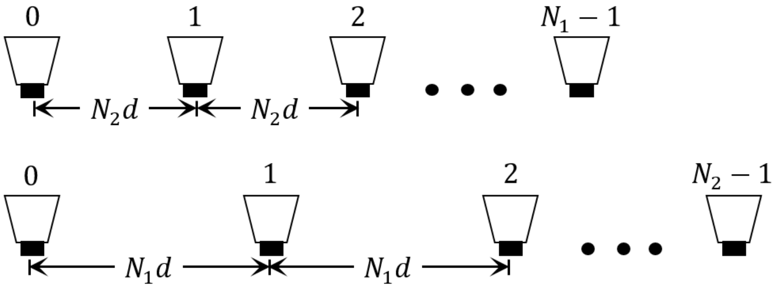

Figure 4-2: Prototype coprime array formation with $N_2 > N_1$.

4.4.Primitive Pythagorean Triples

A triple (N_1, N_2, N_3) is said to be PPT if $\gcd(N_1, N_2, N_3) = 1$. The generation of the PPTs is not trivial, but several ways have been recommended including the famous Barning-Hall tree as narrated in [88]–[90]. Let PPT (N_1, N_2, N_3) be represented as a column vector, when multiplying the PPT with one of the following constants matrices, T_1, T_2 and T_3 then three new PPTs are generated.

$$T_1 = \begin{bmatrix} -1 & 2 & 2 \\ -2 & 1 & 2 \\ -2 & 2 & 3 \end{bmatrix}; T_2 = \begin{bmatrix} 1 & 2 & 2 \\ 2 & 1 & 2 \\ 2 & 2 & 3 \end{bmatrix} \; and \; T_3 = \begin{bmatrix} 1 & -2 & 2 \\ 2 & -1 & 2 \\ 2 & -2 & 3 \end{bmatrix}$$

The process is then repeated using the generated PPTs to produce more triples in a tree fashion. Pythagorean triples found a number of applications in different disciplines including range reduction in software evaluation [88]. In this work, we use PPTs to build sparse arrays for TWRI imaging.

4.4.1. Pythagorean Triple Coprime Based Arrays

We deploy a linear array, X_1, with N_1^2 elements spaced by N_2 units, and an array X_2 with N_2^2 locations spaced by N_1. The two arrays are interlaced to realize the first subaperture, S_1. Then we generate a linear array, X_3 using Pythagoras square, with N_3^2 elements spaced out by N_3 units. The second subaperture, S_2 is obtained by taking all elements in X_3 excluding its intersection with the first subaperture. The configurations X_1, X_2 and X_3 are depicted in Figure 4-3. Mathematically we can write:

$$X_1 = \{n_1 N_2 | 1 \leq n_1 \leq N_1^2 \}$$

$$X_2 = \{n_2 N_1 | 1 \leq n_2 \leq N_2^2 \} \tag{4-2}$$

$$X_3 = \{n_3 N_3 \mid 1 \leq n_3 \leq N_3^2 \}$$

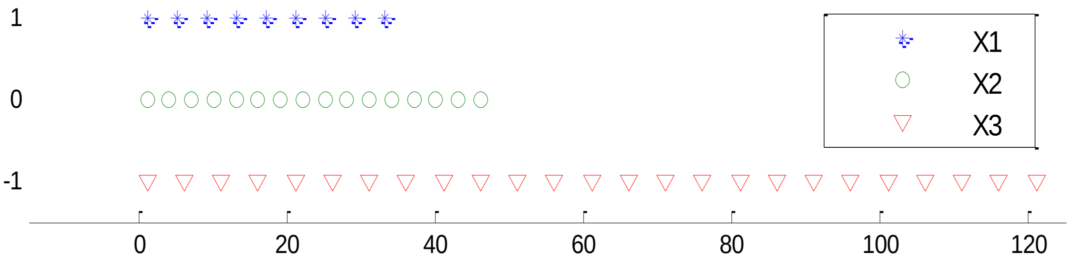

Figure 4-3: Configurations for X_1, X_2 and X_3 for $N_1 = 3$, $N_2 = 4$ and $N_3 = 5$.

The first subaperture, S_1 is defined as:

$$S_1 = X_1 \cup X_2$$

$$|S_1| = N_1^2 + N_2^2 - N_1 = N_3^2 - N_1 \tag{4-3}$$

Similarly, the second subaperture is defined as:

$$S_2 = X_3 - (X_3 \cap S_1)$$

$$|S_2| = N_3^2 - \frac{N_1^2 - 1}{N_2} - \frac{N_2^2}{N_1 + 1} - 1 \tag{4-4}$$

Figure 4-4 shows the models of the two subapertures for $N_1 = 3$, $N_2 = 4$ and $N_3 = 5$. It is observed that the two subapertures pick different radar locations which reduces the correlation of their corresponding sensing matrices which is not guaranteed in random selection modality. More importantly, the resulting subapertures exhibit inherent randomness which improves the sensing matrix.

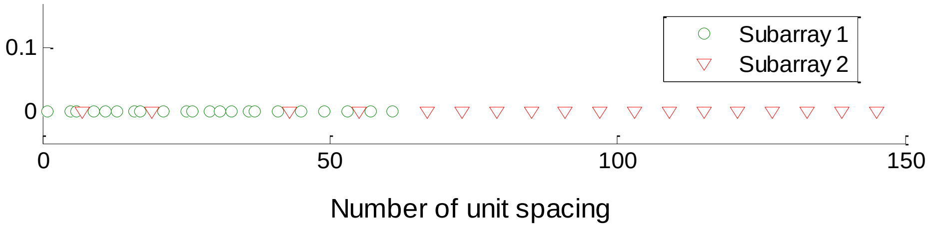

Figure 4-4: Pythagorean based subapertures for $N_1 = 3$, $N_2 = 4$ and $N_3 = 5$.

4.4.2. Pythagorean Aperture Gain

When using the prototype coprime array, the total number of active elements which determines the radar locations is $N_1 + N_2 - 1$ [76]. With the proposed Pythagorean based, the number of active elements, $\widehat{N}$, is given by:

$$\widehat{N} = \min\left\{N_3^2 - N_1, N_3^2 - \frac{N_1^2 - 1}{N_2} - \frac{N_2^2}{N_1 + 1} - 1\right\} \tag{4-5}$$

We can define aperture gain, G, as the ratio of the $\widehat{N}$ to the number of active elements in prototype case as:

$$G = \frac{\min\left\{N_3^2 - N_1, N_3^2 - \frac{N_1^2 - 1}{N_2} - \frac{N_2^2}{N_1 + 1} - 1\right\}}{N_1 + N_2 - 1} \tag{4-6}$$

To select the suitable PPT we need to impose additional conditions to the number of active elements and if possible the aperture gain. If the required aperture when using CS is lN as in Chapter 3, then PPTs are selected such that:

$$\min\left\{N_3^2 - N_1, N_3^2 - \frac{N_1^2 - 1}{N_2} - \frac{N_2^2}{N_1 + 1} - 1\right\} \geq lN \tag{4-7}$$

4.5.Sensing Matrices Design and Their Properties

Unlike random radar selection scenarios, in this case the measurement matrix is designed using predefined radar locations based on the designed arrays above.

Suppose $\boldsymbol{x}_l = \left[x_1, x_2, \dots, x_{|S_l|}\right]^T$ where $x_i \in S_l$, $i = 1, \dots, |S_l|$ represents the radar locations for the l^{th} subaperture, $l = 1,2$. The under sampling matrix, D_l of the l^{th} subaperture is a block identity matrix of size MN with all block rows deleted but $|S_l|$. Mathematically, when J random frequencies are transmitted, we can write:

$$\begin{gathered} D_l \in I_B^{J|S_l| \times MN} \\ I_B = Blkdiag\left(I_{f_1}, I_{f_2}, \dots, I_{f_M}\right) \\ I_{f_j} \in \{0,1\}^{J \times M} \end{gathered} \tag{4-8}$$

I_{f_j} is I_M which is an identity matrix of size $M \times M$,with all other rows randomly deleted but J. In this work we set $\mathrm{I}_{f_1} = \mathrm{I}_{f_2} = \cdots = \mathrm{I}_{f_M}$ for design simplicity.

Having designed **D**, the sensing matrix **A** is then evaluated using $\mathbf{A} = \mathbf{D}\boldsymbol{\Phi}^{(0)}$.

To evaluate the recoverability of the given sensing matrix, we employ mutual coherence of the sensing matrix as defined in Chapter 3. The effectiveness of the sensing matrices of the corresponding subapertures under different measurement volumes with different resolutions for a discretized room of dimension $5 \times 4m^2$ is analyzed. Since the arrays are sparse, the measurement volumes are limited to the number of available radar locations.

The mutual coherence values are better under lower resolution and smaller data volume. For higher resolution case, the coherence values are relatively high but again better than in the previously published works as summarized in Table 4-1. The Table 4-1 shows the mutual coherence values of the sensing matrix against the measurement volumes (in percentage) for image resolutions of 32×32 pixels and 64×64 pixels using subaperture1 and subaperture2. The coherence values were also compared with the conventional CS with equal data volumes. It should be noted that the mutual coherence is only a sufficient but not necessary condition to ensure perfect reconstruction. Using MATLAB simulation and electromagnetic propagation software data, we obtained very good image quality using similar measurement matrices.

Table 4-1: Mutual coherence of subaperture1 and subaperture2

	Subaperture1		**Subaperture2**		**Random**	
Meas. vol (%)	32×32	64×64	32×32	64×64	32×32	64×64
3	0.7302	0.9283	0.3212	0.7032	0.6248	0.9160
5	0.7315	0.9301	0.3301	0.7095	0.6521	0.9198

The first row of Figure 4-5 shows the correlation of a single column with other columns using three array configurations for image resolutions 32×32 pixels and the second row shows the same quantity when resolution changed to 64×64 pixels. The measurement volume in each case was around 5%. The selected columns are column 500 for the case of 32×32 pixels and 2000 for the case of 64×64 pixels for demonstration. It is evident from the figure that subaperture2 yields lower column correlation than the other which ensures good reconstruction.

The sparse arrays make the interelement spacing greater than $\frac{\lambda}{2}$ which is suggested in antenna theory to avoid grating lobes. These proposed arrays are therefore, suitable for sparse reconstructions which are less affected by the grating lobes. To utilize the AD feature, we investigate two scenarios; reconstructing two images using the designed subarrays followed by image fusion and second combining the subarrays and then reconstruct the images.

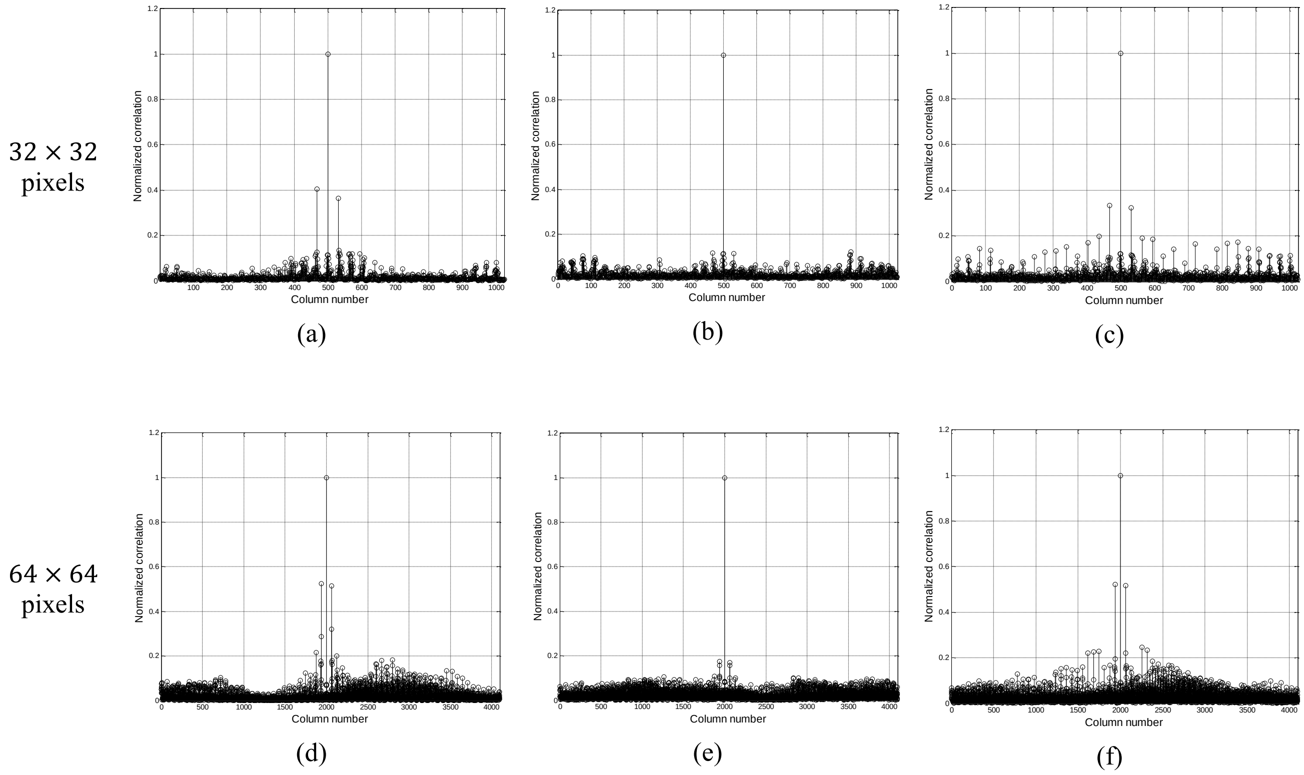

Figure 4-5: Sample correlation of the sensing matrices using (a) subaperture1 (b) subaperture2 (c) Random selection (d) subaperture1 (e) subaperture2 (f) Random selection.

When performing duo-subarray imaging using the designed arrays, the modified subimage, $\check{\mathbf{s}}_i^{(0)}$, can be reconstructed sequentially using CS algorithms as in [58], [59] or concurrently to speed up the reconstruction process.

The reconstructed vectors, $\check{\mathbf{s}}_i^{(0)}$, are obtained by solving optimization problem (2.18). If duo-subarrays are used, then the reconstructed subimages are effectively combined using one of the proposed fusion techniques given on Section 3.3 to yield a final image.

4.6. Arrays Configurations

We examine three different array configurations: PISA, PDSA and Spatial Orthogonal Coprime Array (SOCA).

In PISA, the two Pythagorean coprime triple arrays are amalgamated to form a long array as shown ned $\boldsymbol{x} =$ $[x_1, x_2, ..$

In PDSA, t t the two subaperture in Figure 4-6. If $\tilde{S}_2$ i from $\boldsymbol{x} =$ $[x_1, x_2, ..$

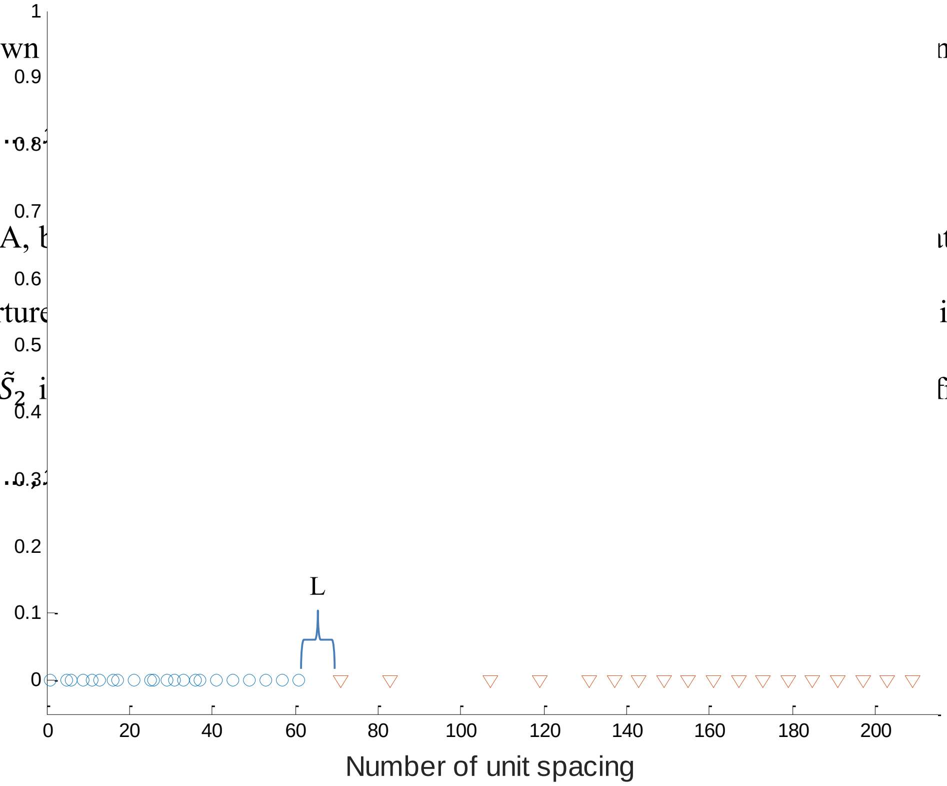

Figure 4-6: PDSA configuration.

For the SOCA, the two arrays are located such that they are perpendicular to each other as shown in Figure 4-7 which increases the DoF in two dimensions. The advantage of the SOCA it covers less space making it attractive to the real applications. However, the limiting factor of this configuration is the standoff distance making it not applicable when larger array is desired. It also requires the knowledge of the background to eliminate the effect of the front wall as spatial filtering technique will no longer be effective. The centers of the two arrays assume the system origin. The radar location, (x, z) is a vector with $x =$

$\left[x_1, x_2, \dots, x_{N_H}\right]^T$ and $z = \left[z_1, z_2, \dots, z_{N_v}\right]^T$ from the horizontal and vertical arrays, respectively.

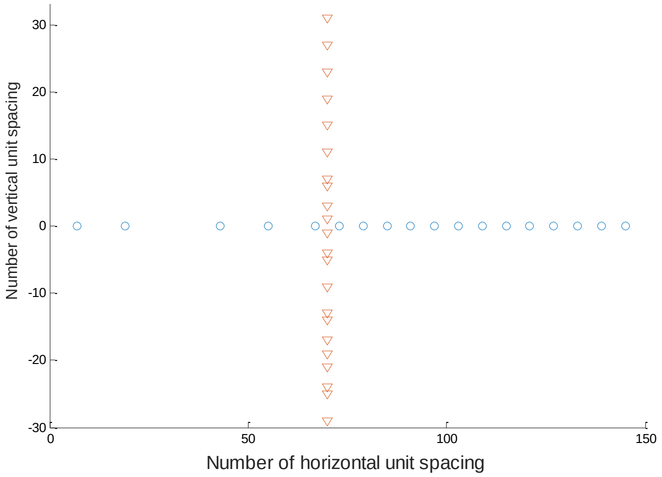

Figure 4-7: SOCA configuration.

4.7.Results and Discussion

In this section, we evaluate the effectiveness of the proposed arrays structures using MATLAB® simulation and electromagnetic simulator, WirelessInsite. In both cases, a total of six different scenarios were realized based on the proposed array configurations as summarized in Figure 4-8. Duo-subarray imaging followed by strategic fusion and combine the subarray and then imaging using the combined aperture for SIPA, SDPA and SOCA configurations are studied.

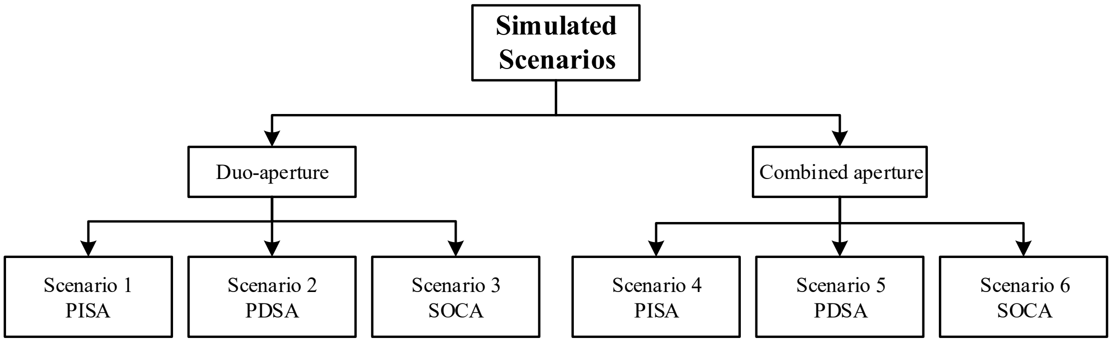

Figure 4-8: Simulated scenarios using duo-aperture and combined aperture.

For both MATLAB® simulation and electromagnetic software, we assume the same measurement setup and room layout depicted in Figure 4-9. The left and right sidewalls of the room reside at crossranges of $-3m$ and $3m$, respectively, while the back wall is at $6m$ downrange. There is a front wall $2m$ away and parallel to the array with thickness $d = 20cm$ and relative permittivity, $\varepsilon_r = 7.67$ as in [1], [20]. A series of 201 monochromatic waves occupying a spectrum between 1 and 3GHz were used to define a UWB signal which gives a range resolution of $7.5cm$ and unambiguous range of up to $15m$. An array of 4m with $0.019m$ interelement spacing was used to interrogate the scene. For the PPTs, $N_1 = 3, N_2 = 4$ and $N_3 = 5$ are used to realize the two Pythagorean subarrays. Only ceiling and floor reflections were covered up leaving the rest of the surrounding walls active. Two metallic cylinders of diameter $0.2m$ and $0.6m$ long are used as targets located at $(0.5, 4)m$ and $(-1.5,4)m$ as shown in Figure 4-9. The background information of the empty scene was first measured for comparison to eliminate the effect of front wall and other stationary clutters. For both, MATLAB simulation and electromagnetic software data, one-fourth of the frequency bins were used for data reduction.

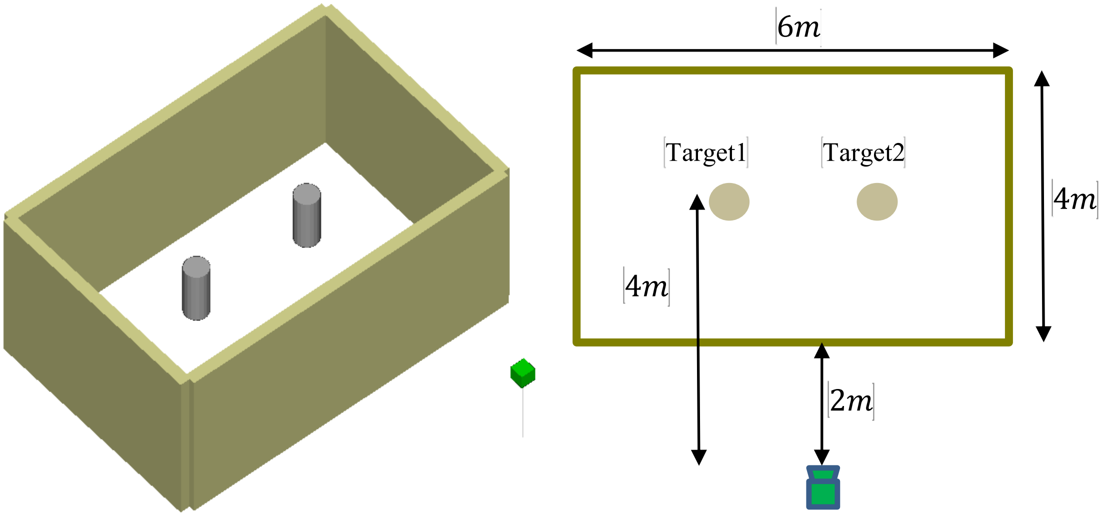

(a) (b)

Figure 4-9: Setting and scene top-view layout (a) 3D view (b) 2D detailed view.

4.7.1. MATLAB Simulation

In the MATLAB simulation measurements, white noise of 0 dB SNR was added to the simulated measurement. The DSBF image with full data volume is generated for comparison and depicted on Figure 4-10. To analyze the quantitative performance of the proposed reconstruction methods we use the three performance metrics defined earlier: TSCR, TRCP and precision.

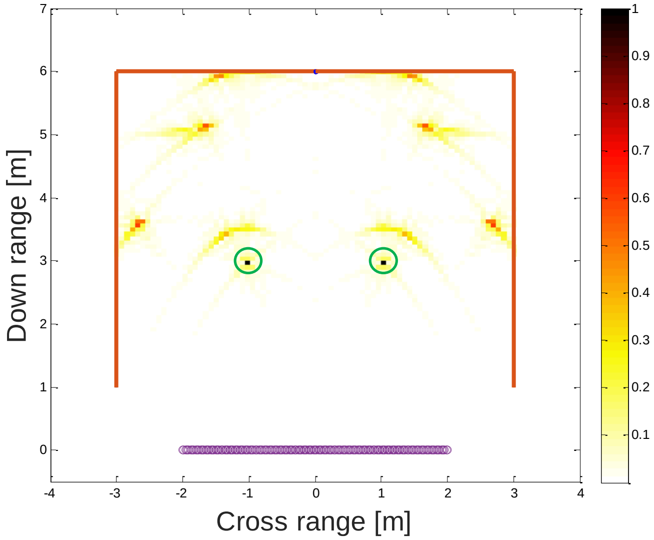

Figure 4-10: DSBF image with full data.

A. *Scenario 1: Duo-Subaperture Imaging with PISA*

In this case, a pair of subimages were captured using the designed subarrays when their corresponding subapertures are interlaced forming a PISA configuration and their corresponding subimages are shown in Figure 4-11 (a) and (b). Then the two subimages are combined using WSAM fusion strategy and the result is shown in Figure 4-11 (f). The Figure 4-11 contains five subimages of the individual subapertures and four final images using PISA, PDSA, SOCA configurations and the random CS is used for comparison. The Figure 4-11 (d) shows that the ghosts have been suppressed with TSCR and TRCP of 86.1dB and 8.0dB, respectively, as summarize in Table 4-2. The precision curve suggests a threshold of around 40% for correct target detection as depicted in Figure 4-12.

B. *Scenario 2: Duo-Subaperture Imaging with PDSA*

In this scenario, the second subarray is displace before imaging forming PDSA configuration. The subimages 1 and 2 in this case are depicted in Figure 4-11 (a) and (c), respectively, and the final image using WSAM fusion is shown in Figure 4-11 (g).

Comparing with PISA, the PDSA configuration showed better results in terms of ghost suppression as the AD effect is more pronounce. The ghosts have been significantly reduced with TSCR of 88.5dB and TRCP of 17.7dB as summarize in Table 4-2. The precision curve shows that with PDSA no post-processing is required for correct target detection as shown in Figure 4-12.

C. Scenario 3: Duo-Subaperture Imaging with SOCA

With SOCA configuration, the vertical array was placed such that the closest antenna has standoff distance of around one meter. Figure 4-11 (a) and (e) show the subimages of subapeture1 and subaprture2, respectively, and in Figure 4-11 (h) is the final image with WSAM fusion. The ghosts have been significantly reduced with TSCR of 88.9dB and TRCP of 13.0dB as summarize in Table 4-2. The TRCP suggests that targets can be detected correctly with small threshold of about 15% as shown by the precision curve in Figure 4-12. The challenge with SOCA configuration is the standoff distance limitation when long array is required and also the front wall mitigation complexity, which jeopardize its feasibility.

Based on qualitative and quantitative results, duo-subaperture imaging with PDSA outperforms the PISA, SOCA and random CS configurations.

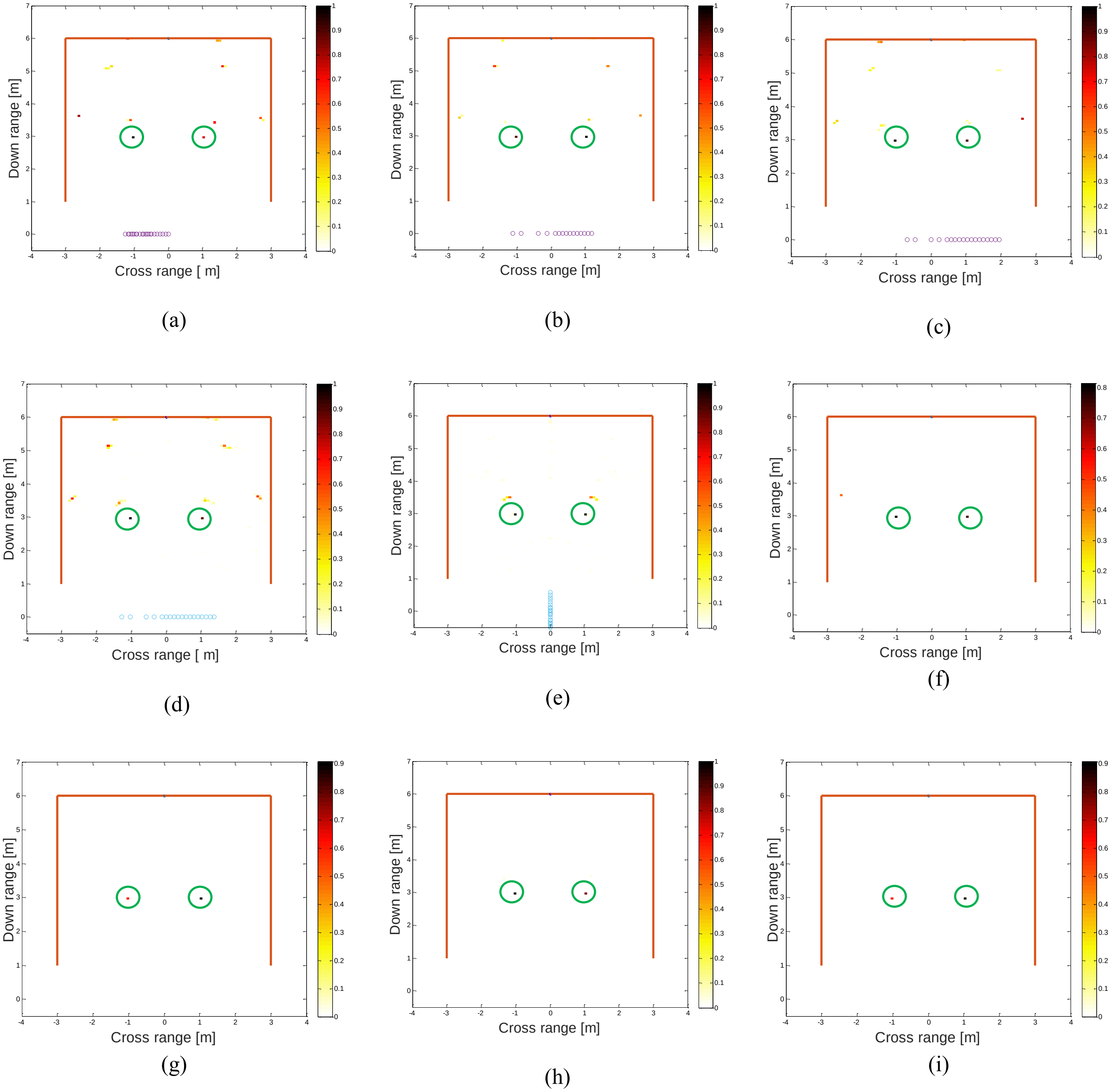

(a) (b) (c)

(d) (e) (f)

(g) (h) (i)

Figure 4-11: Images for MATLAB simulation: (a) subaperture1 (b) subaperture2 (c) displaced subaperture2 (d) horizontal subaperture (e) vertical subaperture (f) PISA (g) PDSA (h) SOCA (i) Random CS.

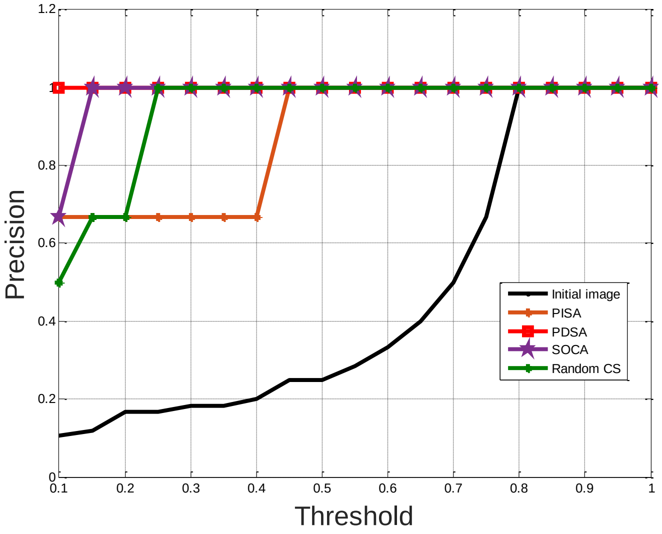

Figure 4-12: Precision curves for duo-subarray using PISA, PDSA, SOCA and Random CS configurations.

D. Scenario 4: Combined Aperture Imaging with PISA

Instead of employing duo-subaperture imaging, in this case we combine the two subarrays to realize a combined array using PISA configuration and the resulting image is given in Figure 4-13. The Figure 4-13 shows four images for combined subapertures, PISA, PDSA, SOCA and random CS configurations. The resulting image in this scenario is shown in Figure 4-13 (a) with TSCR and TRCP of 52.6dB and 6.9dB, respectively, as summarized in Table 4-2. However, post-processing is needed for correct target detection as shown by the precision curves in Figure 4-14.

E. Scenario 5: Combined Aperture imaging with PDSA

In this case, the two subarrays are amalgamated following PDSA approach as described in the previous sections. The resulting image is depicted in Figure 4-13 (b) which shows a noticeable improvement in the quality compared to PISA using TSCR and TRCP performance metrics as summarized in Table 4-2 and supported by the precision curves in Figure 4-14. Its TSCR and TRCP are 49dB and 7dB, respectively.

F. *Scenario 6: Combined Aperture imaging with SOCA*

In this scenario, the subarrays are first merged using SOCA configuration described previously. The system origin was taken at the centers of the arrays and the measurements were collected in ascending order of the radar index starting with horizontal array. The SOCA based image is depicted in Figure 4-13 (c) with TSCR of 49.2dB and TRCP of 6.8dB as shown in the Table 4-2.

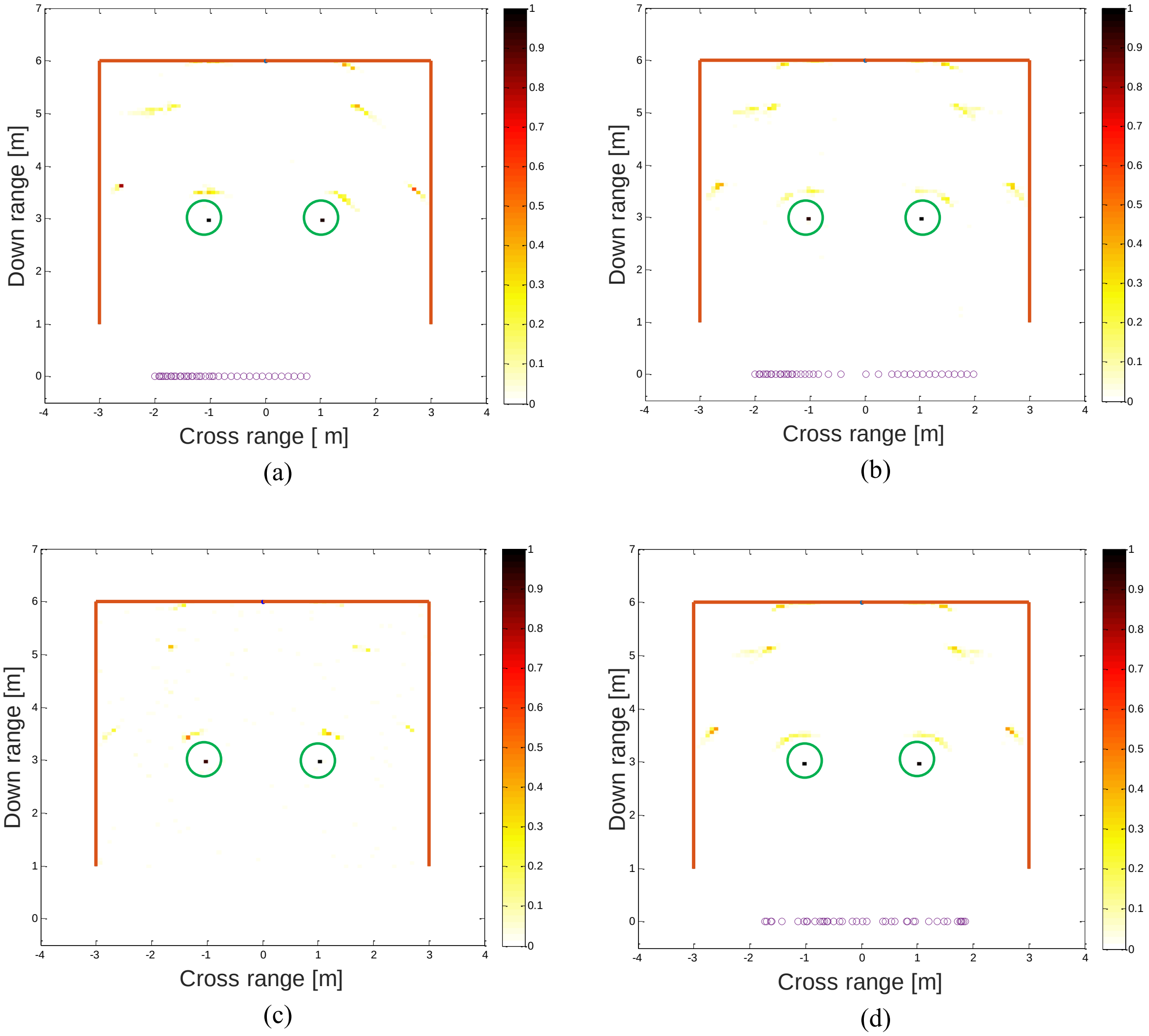

(a) (b) (c) (d)

Figure 4-13: Images using combined array with (a) PISA (b) PDSA (c) SOCA (d) Random CS.

Based on MATLAB simulation, the duo-subaperture based imaging outperforms the combined array imaging counterparts. Taking PDSA as an example, there in a TSCR gain of about 39.5dB and TRCP gain of 10.7dB. These quantitative results suggest that duo-subaperture with PDSA is the best configuration with TWRI applications.

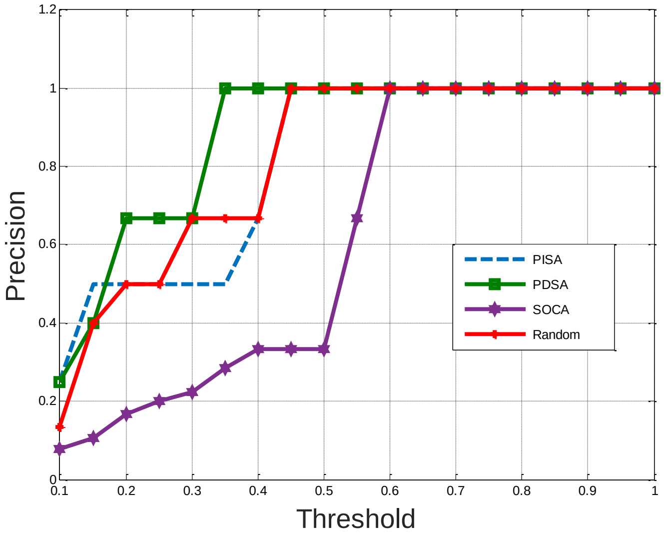

Figure 4-14: Precision curves for combined arrays with MATLAB simulation.

Table 4-2: TSCR and TRCP [dB] for combined and duo-apertures for MATLAB simulation

	Combined Aperture		**Duo-Subaperture**	
	TSCR [dB]	TRCP [dB]	TSCR [dB]	TRCP [dB]
PISA	52.6	6.9	86.1	8.0
PDSA	49.0	7.0	88.5	17.7
SOCA	49.2	6.8	88.9	13.0

4.7.2. Electromagnetic Propagation Software Simulation

A TWRI SAR system was set up under semi controlled environment using WirelessInsite software to demonstrate the effectiveness of the coprime arrays under practical scenarios. Similar setup as in the MATLAB simulation was adopted. Again six scenarios were examined as shown in Figure 4-9.

The results when using duo-subaperture imaging with PISA, PDSA and SOCA are shown in Figure 4-15. The Figure 4-15 contains five subimages from the individual subapertures and four final images based on PISA, PDSA and SOCA configurations, the random CS is used for comparison. Figure 4-15 (a) and (b) show the images of the primary subapertures and Figure 4-15 (c) is the image of the displaced subaperture2. Figure 4-15 (d) and (e) are the images of the horizontal and vertical subapertures for the SOCA configuration. The final images using PISA, PDSA and SOCA configurations are shown in Figure 4-15 (f), (g) and (h), respectively. The image using the random CS is depicted in Figure 4-15 (i) for comparison assuming one realization. The three images show good quality in terms of ghost suppression with quantitative measures summarized in Table 4-3 and supported by the precision curves as shown in Figure 4-16. PDSA shows better TRCP of 20dB compared to PISA and SOCA configurations. Figure 4-15 (i) shows the final image when using random selection which returns the TSCR and TRCP of 91.1dB and 15.7dB, respectively, as summarized in Table 4-3.

Also we implemented the combined arrays using PISA, PDSA and SOCA configurations emulating scenarios 4-6. The resulting images are respectively shown in Figure 4-17 (a), (b) and (c). The random selection configuration shown in Figure 4-17 (d) is presented for comparison.

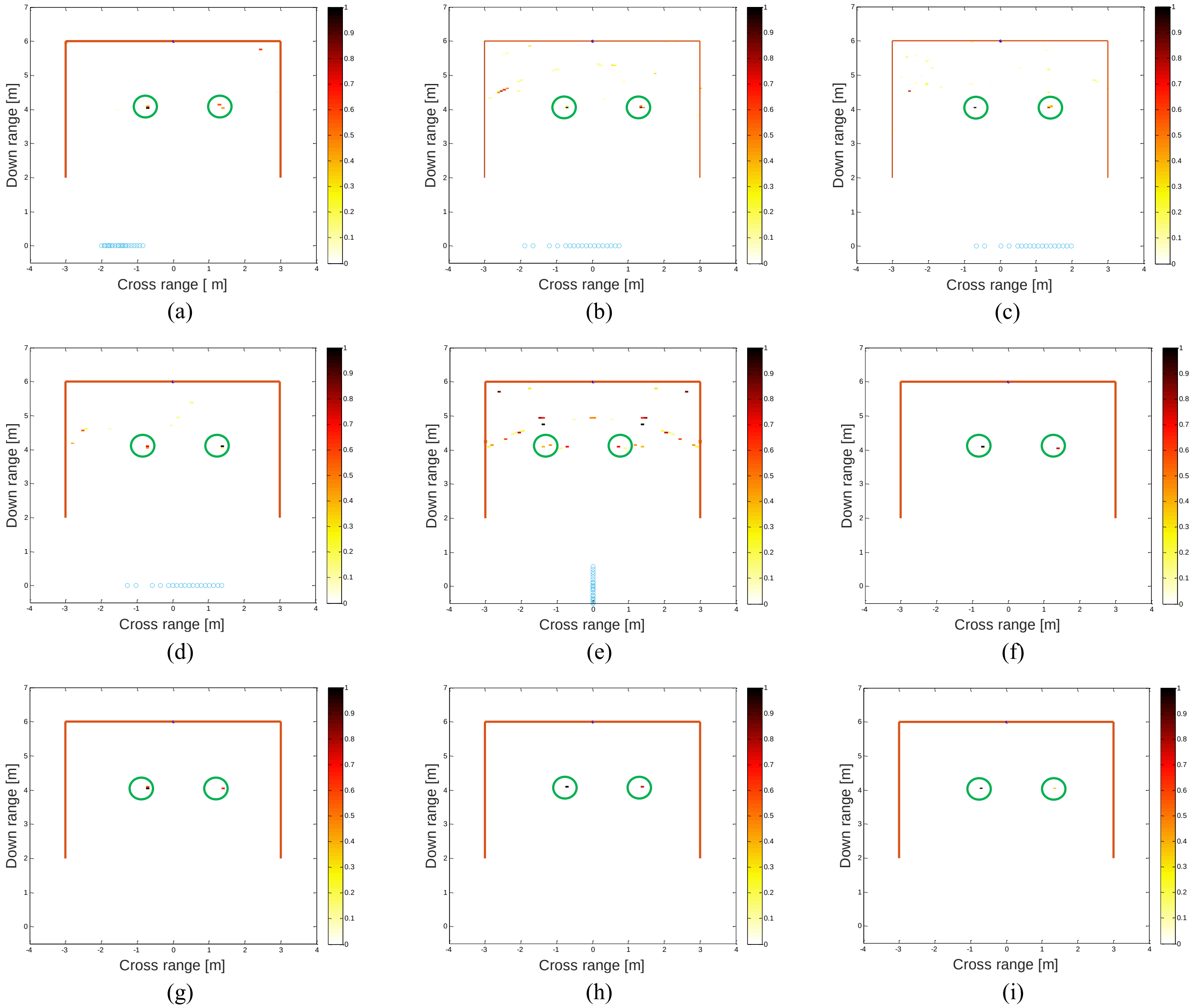

(a) (b) (c)

(d) (e) (f)

(g) (h) (i)

Figure 4-15: Final Images using: (a) subaperture1 (b) subaperture2 (c) displaced subaperture2 (d) horizontal subaperture (e) vertical subaperture (f) PISA (g) PDSA (h) SOCA (i) Random CS.

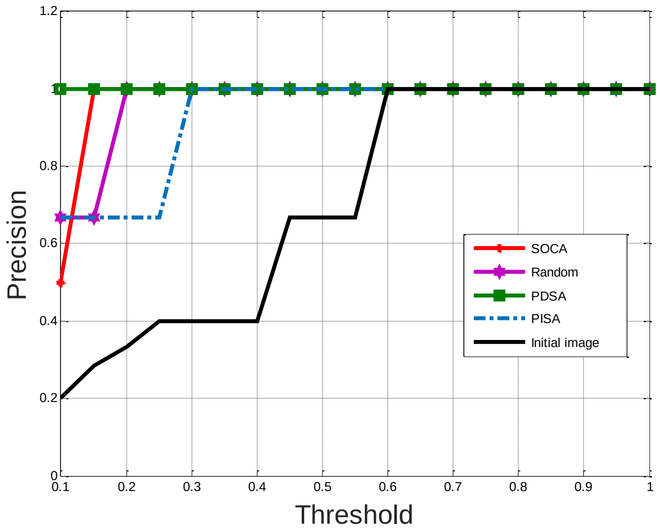

Figure 4-16: Precision curves for duo-subaperture imaging with electromagnetic software data.

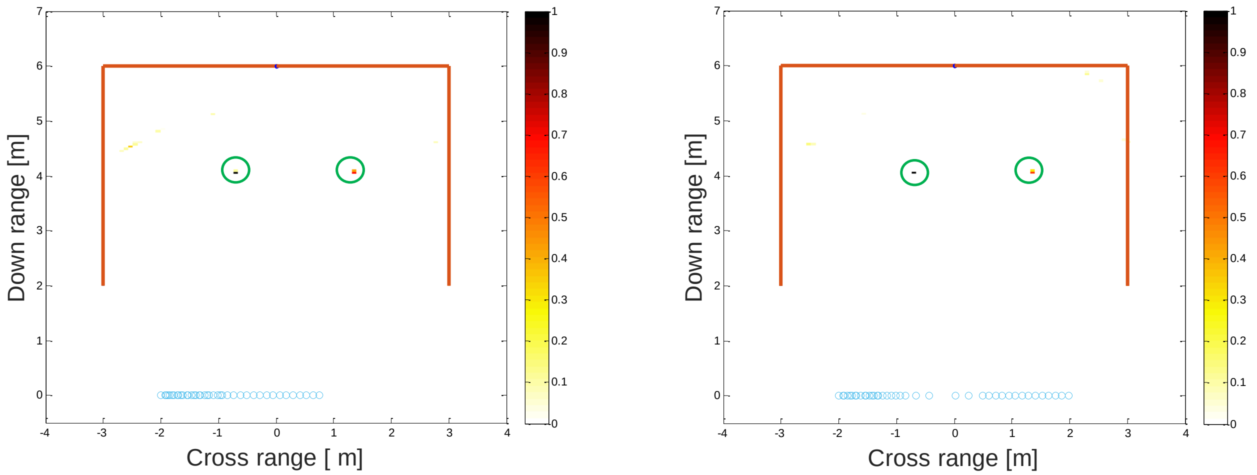

(a) PISA

(b) PDSA

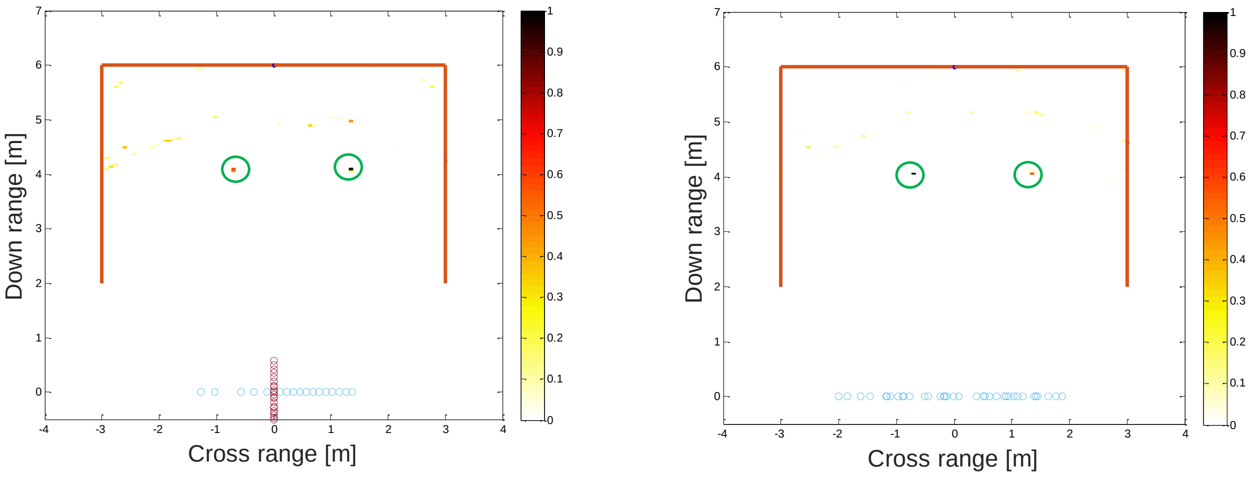

(c) SOCA

(d) Random CS

Figure 4-17: Images using combined aperture (a) PISA (b) PDSA (c) SOCA (d) Random CS.

To quantify the performance, TSCR and TRCP are evaluated for combined array based configuration and summarized in Table 4-3. In this context, the reconstructed ghosts are treated as clutters. From Table 4-3, the PDSA shows relatively good results of TRCP of 10.3dB compared to other configurations. The SOCA configuration on the other hand, is highly cluttered reducing the image quality significantly. The duo-subarray based configuration by far show good performance compared to their combined arrays counterparts as summarize in Table 4-3 and precision curves in Figure 4-18. It should be noted that the random based subimage was only taken once and on average its quality is expected to reduce noticeably.

Table 4-3: TSCR and TRCP [dB] for combined and duo-apertures imaging based on electromagnetic software

	Combined Aperture		**Duo-Subaperture**	
	TSCR [dB]	TRCP [dB]	TSCR [dB]	TRCP [dB]
PISA	70.8	8.0	93.1	15.0
PDSA	70.9	10.3	91.8	20.0
SOCA	58.9	6.5	88.9	17.6
CS	66.5	7.7	91.1	15.7

The TRCP values are reflected in the precision curves in Figure 4-18. The precision gives information on the probability of correct target detection in the presence of ghosts and other clutters. It is noted in Figure 4-18 that the threshold of around 35% is enough to correctly detect genuine targets in the presence of the clutters using combined array PDSA showing the strength of the coprime based arrays.

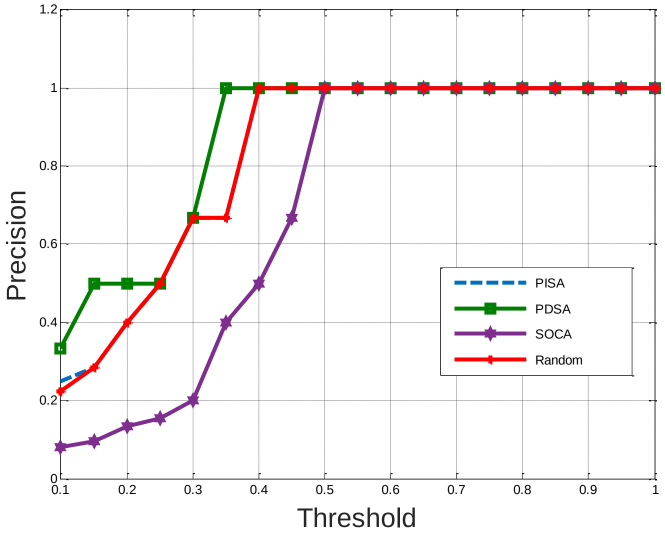

Figure 4-18: Precision curves for combined arrays with electromagnetic software data.

4.8. Conclusions

In this chapter, we proposed coprime arrays based on the Pythagorean triple for TWRI applications and their recoverability were studied by evaluating the mutual coherence of their sensing matrices. We investigated the performance of the proposed subarrays under multipath environment. Two subarrays were proposed using pairs of coprime numbers derived from PPTs and their effectiveness on TWRI applications under multipath environment were studied.

Two imaging modalities were examined: using pair of proposed subapertures followed by effective image fusion; and fusing the two subapetures before imaging approaches. The former approach demonstrated outstanding performance in terms of multipath ghost suppression particularly with PDSA configuration using both MATLAB simulation and electromagnetic propagation software data attaining TRCP of about 20dB. The latter however, gave an acceptable results particularly when using the electromagnetic software data. This result alludes that it can be effective in real applications where the side wall attenuate the signal unlike in MATLAB simulation where the side walls were taken as perfect reflectors. Taking the directionality of the UWB antenna into account, the PISA will be the best candidate in practical applications. If background information is known beforehand, SOCA configuration will offer the best option.

Up to this far, the target is assumed to occupy a single pixel of the given scene. This assumption is limited in some other practical applications where target occupy more than one pixel. In the subsequent chapter, extended target will be considered in which case a target is assumed to occupy more than one pixel instead. The notion of the extended target reconstruction will be presented in a different perspective with and without multipath contributions.

4.9. List of Publications

1. A. T. Abdalla and Ali. H. Muqaibel, "Through-the-Wall Radar Imaging Exploiting Pythagorean Coprime-Based Apertures with Sparse Reconstruction", Digital Signal Processing. Submitted
2. A. T. Abdalla and Ali. H. Muqaibel, "Multipath Ghost Suppression in TWRI Exploiting Aspect Dependence Feature with Pythagorean Triple Coprime-Based Arrays", to be submitted

> *"...dealing with extended targets is more challenging. First, the assumption of independent scattering centers as used in geometrical optics is violated. Second, the reflections occur at different points of the target when observed via various paths. In effect, the images associated with the various paths do not perfectly overlap anymore. Hence, a novel concept of approximate group sparsity would be needed to account for this effect..."*
>
> **Leignering** [60]

CHAPTER 5

EXTENDED TARGETS MODELLING AND BLOCK AGNOSTIC SPARSE RECONSTRUCTION IN TWRI: A DIFFERENT PERSPECTIVE

5.1.Introduction

Unlike in Point Targets (PTs), the received signal from Extended Target (ET) is an integration of the scattered signals from various parts of the same target. As such, a more general model needs to be proposed to encompass the ETs as the previous point-like assumption does not hold. This chapter will review the recent approaches on ETs imaging and reconstructions in TWRI and propose a new suitable model.

It is clear from the literature that ET modeling and reconstruction under CS framework have not been extensively studied yet. A handful of contributions have pointed the issue out without thorough analysis and formulations [41], [91]. The current reconstruction methods require the constant block size assumption, the size and number of the blocks. If statistical information of the signal is to be used, they assume Gaussian distribution.

In this chapter, we suggest a different but realistic ET reconstruction approach based on agnostic block sparsity. We implement the recently proposed block sparse reconstruction algorithm which is target agnostic with varying block sizes to the TWRI problem. The algorithm, Block Support Agnostic Bayesian Matching Pursuit (BlockSABMP), was first presented by Mudassir Masoud and Tareq Al-Naffouri who first proposed the algorithm in [57]. To the best of our knowledge this algorithm has not been used in TWRI application and due to its properties its introduction can reinvigorate the field. We modify the signal model and present mathematical formulation describing the ground truth as block sparse vector with unknown block sizes and the target distribution. The variation of the block sizes in the image vector reflects complex shaped target in the original scene. Further, in the case of multiple ETs, they are not necessarily have to follow the same distribution and therefore, the overall target distribution will not be straightforward.

The rest of this chapter is organize as follows: Section 5.2 presents the literature review. The new extended target model based on block sparse structure is developed in Section 5.3. Section 5.4 presents the block sparse reconstruction based on minimum mean square error estimation. Section 5.5 generalizes the model under multipath presence. Section 5.6 defines the performance metrics and their significances are enumerated. Two performance measures are defined: Normalized Mean Square Error (NMSE) and Earth Mover's

Distance (EMD). Results based on MATLAB simulation and experimental data are given is Section 5.7 and Section 5.8 summarizes the chapter.

5.2.Literature Review

A common target model in radar imaging literature obeys the PT assumption in which, a target is hypothesized to occupy a single pixel. In contrast, some targets may occupy more than one pixel and termed as ET [10], [38], [92], [93]. This clustering of the target pixels can be exploited to enhance the reconstruction performance [68], [94], [95].

The ET is described using two parameters: the target length (extent) and the target reflection coefficient [10], [92]. In the literature, two types of reflection coefficients' distributions have been considered: assuming constant value distribution across the entire target extent and the Gaussian distribution [10]. The constant value coefficient implies that the energy of the reflected signal across the entire target is the same. On the other hand, the Gaussian distributed coefficients implies that the energy of the reflected signal is most pronounced at the center of the targets [10] as summarized in Figure 5-1. However, the two assumptions do not apply in wide range of real TWRI applications and we therefore, claim in this work that it is fair and realistic to assume unknown distribution for the reflection coefficients, *target agnostic*, instead.

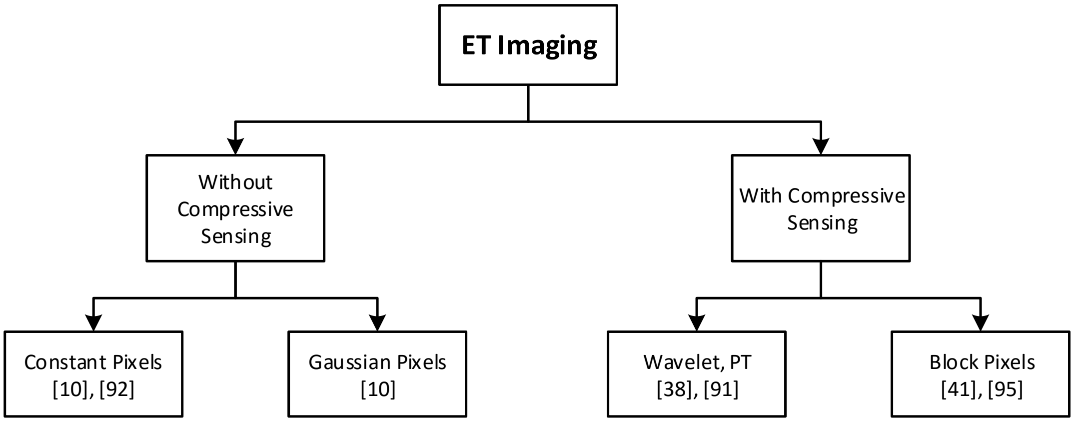

Figure 5-1: Summary of the literature review in ET imaging.

To the best of our knowledge, ET modeling with sparse reconstruction in TWRI have not been rigorously studied yet. A few recent contributions on ETs under CS are available [41], [91], [93] . For the CS-based reconstruction, there are two main suggested approaches to deal with ETs which are wavelet decomposition [91] and block sparsity approaches [41] as shown in Figure 5-1. A contribution based on wavelet transform was given in 2011[91] alluded that the wavelet transform didn't bode well following some challenges. On the other hand, [41] proposed block sparsity as a solution to the ET problem. The author suggested the use of block sparse reconstruction algorithm mentioning a Block OMP (BOMP) as an example with no detailed information. In [5], the authors exploited the group sparsity due to the multi-polarization sensing modality, and the clustering sparsity due to the target spatial extent using modified clustered multi-task Bayesian compressive sensing. These proposals are only applicable for rectangular shaped targets as all blocks in the image vector assumed to carry equal number of active pixels. In real TWRI applications, we are dealing with more complex targets like humans, rifles, to name a few, whose shapes cannot be well approximated by rectangular shapes. This calls for a more generalized model.

In TWRI applications, the target size, the number of behind the wall targets and even their reflectivities distributions are unknown in priori. In multiple target scenario with non-homogeneous scene, the overall pixel value distribution becomes complicated even if the distributions of the individual target's reflectivities are known. This is due to the vectorization of the ground truth by concatenating the columns of the discretized version of the ground truth which results into chunks (blocks) of pixels drawn from different distributions. The overall pixel value distribution will challenge the applicability of reconstruction algorithms which work under particular type of distribution.

In this chapter, we suggest a different ET reconstruction based on block sparsity with varying block sizes to mimic real TWRI applications. The additional advantage with such model is that if the scene comprises of mixture of PTs and ETs, it can reconstruct both concurrently by treating PTs as blocks of size one contrary to the existing approaches where the two are reconstructed independently as in [10]. Additionally, dealing with complex shaped targets, it is of interest to correctly recover the shape of the target for correct image interpretation and therefore, algorithm which ensures minimum error is highly desired. With the aforementioned facts on the target's reflectivity behaviors, the appropriate reconstruction algorithm in TWRI is desired to satisfy at least the following properties:

a) It should minimize the mean squared error to ensure correct image reconstruction (Bayesian based approach).

b) It should work under varying block sizes scenario to incorporate complex shaped targets and heterogeneous ground truths.

c) It should work under unknown target distribution as the information is either hardly available or might be mathematically intractable.

These facts naturally suggest a recently proposed block sparse reconstruction algorithm which is distribution agnostic with varying block sizes, BlockSABMP, to be the appropriate candidate in TWRI. To accomplish the task, the ET received signal model needs to be reformulated as block sparse vector.

5.3. Received Signal Model

In this subsection, we develop an ET signal model for 2D imaging. An example of an ET which extend in both, range and crossrange directions is depicted in Figure 5-2(a). The pixel value distribution is assumed to be unavailable in priori. The assumption is justifiable in TWRI applications as in multiple targets scenario the vector of the scene (ground truth) which is obtained by concatenating columns of the scene matrix as shown in Figure 5-2 (b) may have complicated reflectivity distributions.

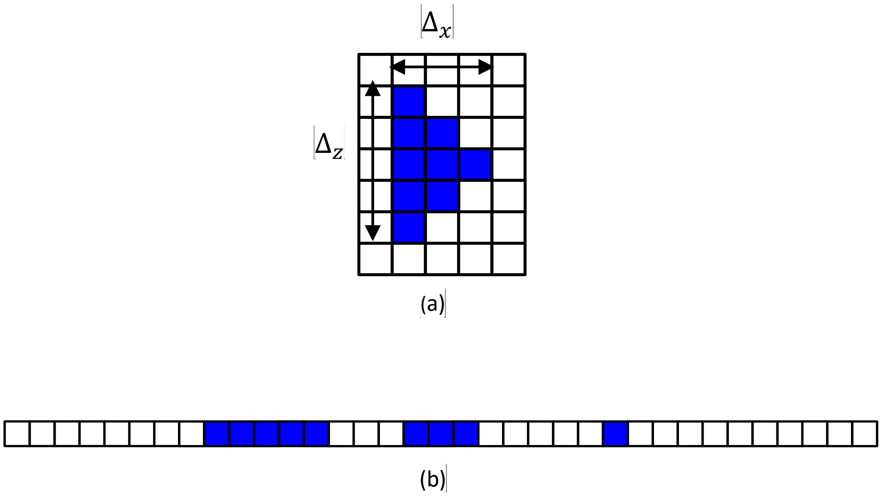

Figure 5-2: Block representation of extended signal (a) the original scene (b) vectorized scene.

Consider a SAR of N locations which transmits M equally spaced monochromatic waves at each location for the scene interrogation as shown in Figure 2.2. The target in this case is assumed to span an area of $\Delta x \times \Delta z$ along the crossrange and downrange directions. From the PT received signal (2.7), the total return at the n^{th} radar location due to Q ETs taking into account the spatial extents when the m^{th} frequency, f_m, is transmitted can be expressed as:

$$y[m,n] = \sum_{q=0}^{Q-1} \int_0^{\Delta x} \int_0^{\Delta z} \sigma_{q_{xz}}\, exp(-j2\pi f_m \tau_{xzn}) dxdz + v(m,n) \tag{5-1}$$

where $\sigma_{q_{xz}}$ is the reflectivity of the point (x,z) laying on the q^{th} parget and $\tau_{xzn}$is its corresponding delay.

For high resolution image, we subdivide the scene into small sized pixels, N_x and N_y in crossrange and downrange, respectively. The response in (5-1) can be expressed as:

$$y[m,n] = \sum_{q=0}^{Q-1} \sum_{p=0}^{N_x N_y - 1} \sigma_{pq} \exp\left(-j2\pi f_m \tau_{pn}\right) + v(m,n) \tag{5-2}$$

where σ_{pq} refers to the reflectivity of the p^{th} pixel laying on the q^{th} ground truth. We model the scene as a sum of disjoint ground truths for evolutionary simplification. In matrix form, we can write (5-2) as:

$$\begin{gathered} \mathbf{y} = \mathbf{\Phi} \boldsymbol{s}_1 + \mathbf{\Phi} \boldsymbol{s}_2 + \cdots + \mathbf{\Phi} \boldsymbol{s}_{Q-1} + \mathbf{v} = \mathbf{\Phi} \mathbf{s} + \mathbf{v} \\ \mathbf{s} = \mathbf{s}_0 + \mathbf{s}_1 + \cdots + \mathbf{s}_{Q-1} \end{gathered} \tag{5-3}$$

$\mathbf{y} = (y[0,0], y[1,0], \ldots y[M-1,0], y[0,1], \ldots\, y[M-1, N-1])^T$, $\mathbf{s}_{\boldsymbol{q}} \in \mathbb{C}^{\boldsymbol{N_x N_y \times 1}}$, is a vector of reflectivities, σ_{pq} of the q^{th} ground truth and the entries of the matrix $\mathbf{\Phi} \in \mathbb{C}^{MN \times N_x N_y}$ are defined as:

$$\begin{gathered} [\mathbf{\Phi}]_{ip} = \exp\left(-j2\pi f_m \tau_{pn}\right) \\ m = i \bmod M, \qquad n = \left\lfloor \frac{i}{M} \right\rfloor, \qquad i = 1,2,..MN-1 \end{gathered} \tag{5-4}$$

In the presence of multipath, the received signal when m^{th} frequency is transmitted at n^{th} location is the summation of all pixels contributions for all possible returns. Suppose there are $R-1$ multipath returns, then $y[m,n]$ is given by:

$$y[m,n] = \sum_{r=0}^{R-1} \sum_{q=0}^{Q-1} \sum_{p=0}^{N_x N_y - 1} \sigma_{pq}^{r} \exp\left(-j2\pi f_m \tau_{pn}^{r}\right) + v(m,n) \tag{5-5}$$

In matrix notation, we can generalize (5-5) as:

$$\begin{gathered} \mathbf{y} = \mathbf{\Phi}\boldsymbol{s}^{(0)} + \mathbf{\Phi}\boldsymbol{s}^{(1)} + \cdots \mathbf{\Phi}\boldsymbol{s}^{(R-1)} + \mathbf{v} \\ \mathbf{s}^{(r)} = \boldsymbol{s}_0^{(r)} + \boldsymbol{s}_1^{(r)} + \cdots \boldsymbol{s}_{Q-1}^{(r)} \end{gathered} \tag{5-6}$$

where $\mathbf{s}^{(r)}$ is the image vector as viewed by the r^{th} multipath return and all other symbols carry their usual meanings. Analogous to [57], $\mathbf{s}$ is further modeled as Hadamard product, $\boldsymbol{s} = \boldsymbol{s_A} \odot \boldsymbol{s_B}$, where $\boldsymbol{s}_A$ is the vector of target's reflectivity values with unknown distribution and $\boldsymbol{s}_B$ is the binary vector with Bernoulli's distribution indicating the presence or absence of a given target pixel.

When the ground truth, $\mathbf{s}$, comprises of Q independent and complex shaped ETs, is discretized and vectorized by appending its columns, the result is a tall vector with K active blocks of varying length and probability density function (pdf) as shown in Figure 5-2. The pdf of the k^{th} block (chunk of pixels) in $\boldsymbol{s_A}$, f_{s_k} is not necessarily $= f_{sj}$ for $k \neq j$. Since the chunks of pixels are disjoint, then the probability distribution of the overall vector $\boldsymbol{s_A}$, f_s is given by:

$$f_s = \begin{cases} f_{s1} & 0 < x < x_0 \\ f_{s_2} & x_0 < x < x_1 \\ \vdots & \vdots \\ f_{sK} & x_{K-1} < x < x_K \end{cases}$$

$$f_s = \sum_{k=1}^{K} f_{sk} \times [u(x_k - x_{k-1})] \tag{5-7}$$

where $|x_{k-1} - x_k|$ signifies the length of the k^{th} block of pixels, which is not necessarily the same for different values of k. Even if the distribution of each target is known in prior, the overall distribution of the vectorized scene is not straight forward and therefore, Bayesian algorithms which assume Bernoulli-Gaussian or Bernoulli-Laplacian for the signal $\boldsymbol{s_A}$ will be challenged.

The image vector reconstruction for ETs can be molded as a block sparse signal reconstruction problem.

5.4.Block Sparse Image Vector Reconstruction

Using undersampling matrix, $\mathbf{D}$, to reduce the amount of information in (5-6), we define the compressed observation as, $\bar{\mathbf{y}}$ as:

$$\bar{\mathbf{y}} = \mathbf{D\Phi}\,\mathbf{s} + \bar{\mathbf{v}} \tag{5-8}$$

From (5-8), our sensing matrix is defined by the product $\mathbf{D\Phi}$. The minimum mean squared estimate of $\mathbf{s}$, $\check{\boldsymbol{s}}$ is obtained by [57], [68], [69]:

$$\check{\boldsymbol{s}} \triangleq \mathbb{E}[\boldsymbol{s}\,|\bar{\mathbf{y}}] = \sum_{S} p(\mathrm{S}|\bar{\mathbf{y}})\mathbb{E}[\mathbf{s}|\bar{\mathbf{y}}, S] \tag{5-9}$$

where S represents the set of target pixels. To obtain the mean squared estimate, we need to evaluate $p(S|\bar{\mathbf{y}})$ and $\mathbb{E}[\mathbf{s}|\bar{\mathbf{y}}, S]$. Since we assume unknown distribution of the image vector, the conditional expectation becomes cumbersome and therefore, it is approximated using best linear unbiased estimator given by [57]:

$$\mathbb{E}[\boldsymbol{s}|\bar{\boldsymbol{y}}, S] \leftarrow \left[(\mathbf{D\Phi})_{\boldsymbol{S}}^{\boldsymbol{H}}(\mathbf{D\Phi})_{\boldsymbol{S}}\right]^{-1}(\mathbf{D\Phi})_{\boldsymbol{S}}^{\boldsymbol{H}}\bar{\boldsymbol{y}} \tag{5-10}$$

The conditional probability, $p(\bar{\mathbf{y}}, S)$ on the other hand is obtained using Bayes' rule:

$$p(S|\bar{\boldsymbol{y}}) = \frac{p(\bar{\boldsymbol{y}}, S)p(S)}{p(\bar{\boldsymbol{y}})} \tag{5-11}$$

The denominator, $p(\bar{\boldsymbol{y}})$, is a common factor to all posterior probabilities and can therefore be ignored. As the target pixels are activated according to Bernoulli's distribution with success probability, say γ, we can write:

$$p(S) = \gamma^{|S|}(1-\gamma)^{N_x N_y - |S|} \tag{5-12}$$

The likelihood, $p(\bar{\boldsymbol{y}}, S)$ when the target's distributions are unknown is approximated by projecting $\bar{\boldsymbol{y}}$, onto the orthogonal complement space of $(\mathbf{D\Phi})_{\boldsymbol{S}}$. Following simplification in [57], $p(\bar{\boldsymbol{y}}, S)$ can be simplified to:

$$p(\bar{\mathbf{y}}, \mathrm{S}) \approx \exp\left(\frac{-1}{2\sigma_w^2} \|\mathrm{P}_S^{\perp}\bar{\mathbf{y}}\|^2\right) \tag{5-13}$$

where $\mathrm{P}_S^{\perp} = \mathrm{I} - \mathrm{P}_\mathrm{S} = \mathrm{I} - (\mathbf{D\Phi})_{\boldsymbol{S}}\left[(\mathbf{D\Phi})_{\boldsymbol{S}}^{\boldsymbol{H}}(\mathbf{D\Phi})_{\boldsymbol{S}}\right]^{-1}(\mathbf{D\Phi})_{\boldsymbol{S}}^{\boldsymbol{H}}$

where$(\mathbf{D\Phi})_{\boldsymbol{S}}$ is a matrix formed by selecting columns of $\mathbf{D\Phi}$ indexed by support S. The algorithm starts by finding the optimal support of unit size and then grow the block around the given support as elaborated in [57]. The dominant target pixel selection metric, $\mathcal{V}(S)$ is defined according to [68]:

5.5.Performance Metrics

To evaluate the quantitative performance, we employ two metrics: Normalized Mean-Squared Error (NMSE) and Earth Mover's Distance (EMD).

5.5.1. Normalized Mean Square Error

The Normalized Mean-Squared Error (NMSE) between the estimated scene, $\check{\boldsymbol{s}}$, and the ground truth, $\boldsymbol{s}$, amounts for the deviation between estimated and the true image vector. Mathematically, it is given by [57]:

$$\mathrm{NMSE} = \frac{1}{T}\sum_{t=1}^{T} \frac{\|\check{\boldsymbol{s}}_t - \boldsymbol{s}\|_2^2}{\|\boldsymbol{s}\|_2^2} \tag{5-14}$$

where T is the number of Monte Carlo runs for averaging the quantity.

5.5.2. Earth Mover's Distance

To evaluate the image quality of the reconstructed scene, NMSE alone is not enough as it does not ensure the pixel locations in the image, thus Earth Mover's Distance (EMD) was defined as generalized metric. The EMD signifies the level of dissimilarity between distributions and in this context returns the amount of image intensity that has to be moved to convert one image to the other by moving distribution mass around. Lately, EMD became a popular metric for the image comparison [41], [60]. MATLAB implementation of this metric is available from MATLAB Central File Exchange website [96].

5.6. Results and Discussion

In this section we present results based on MATLAB simulation and experimental data. In the simulation, four scenarios were implemented. An ET with complicated shape which results into blocks of varying length when the scene is vectorized. The second scenario assumes the Rayleigh distribution of the target pixels. The third scenario simulates the heterogeneous scene containing PTs and ET and we perform join reconstruction and the forth simulates multipath scenario. For the experimental part, a semi-controlled environment was used to evaluate the performance.

5.6.1. MATLAB Simulation

A uniform linear monostatic array composed of 77-elements with aperture length of $2m$ is deployed to capture the image of the scene. The center of the array assumes the system origin. A series of 201 monochromatic waves occupying a spectrum between 1 and 3GHz was employed for scene interrogation. Only one fourth of the frequency bins and one half of the radar locations (making 12.5% of the total data volume) were used to capture the image of the scene where the imaged area was $4 \times 4m^2$. We assume no multipath case and the front wall contribution was suppressed by spatial filtering as in [48]. Additive white Gaussian noise with SNR of 20dB was added on the measurement and the reconstructed image is compared with DSBF under the same reduced measurement volume, conventional CS algorithm and Block OMP (BOMP) algorithm. Since there are various versions of block sparse algorithms, we selected BOMP as it was suggested in TWRI literature as a possible candidate [41].

Four different scenarios were simulated and the block agnostic approach was compared with selected existing approaches:

A. Complex Target with Constant Valued Reflectivity

In this case, a complex shaped target is simulated as shown in Figure 5-3. The image is reconstructed using one-fourth of the frequency bins and one-half of the radar locations, both were selected randomly. The image of the scene using the block agnostic is of high quality compared to that of conventional CS and conventional block as shown in Figure 5-4. Figure 5-4 (a) shows the reconstructed image using DSBF with reduced data volume which is highly cluttered due to the point spread function and grating lobes artifacts. The conventional CS which works under PT assumption does not well reconstruct the image as depicted in Figure 5-4(b). Also, the conventional block which works under equal block sizes assumption fail to correctly reconstruct the complex shaped target for the given data volume as shown in Figure 5-4(c). The relatively poor performance of the conventional equal block sizes assumption is due to the fact that when the scene containing complex shaped target is vectorized it results into a vector having different block sizes.

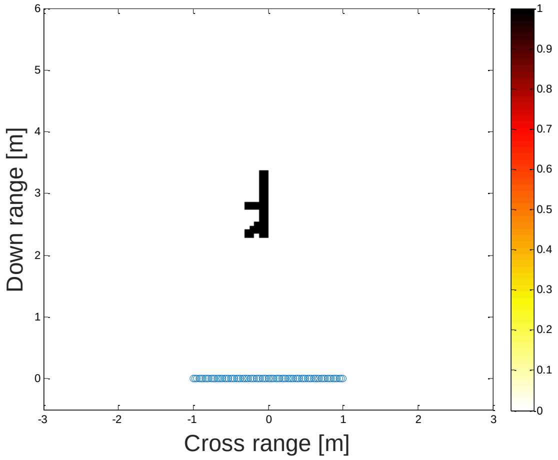

Figure 5-3: The original scene with complex shaped target.

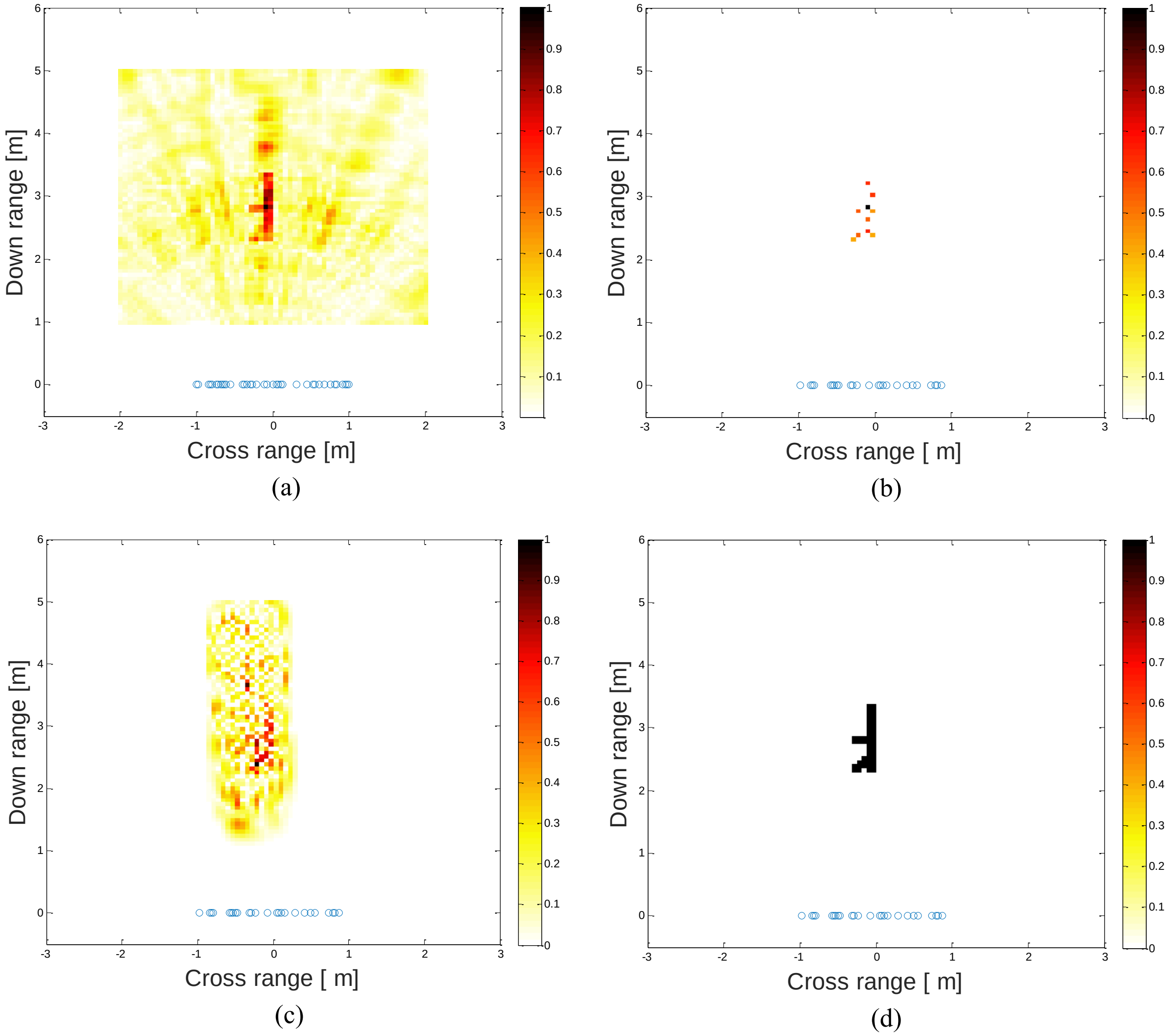

(a)

(b)

(c)

(d)

Figure 5-4: Images for uniform target (a) DSBF (b) Conventional CS (c) BOMP (d) Block Agnostic.

To quantify the performance, NMSE and EMD were evaluated and averaged to 50 Monte Carlo runs. Figure 5-5 (a) shows the variation of NMSE with the measurement percentage volume. The DSBF show the worst performance as expected due to the point spreads function and grating lobes artifact under reduced radar locations. The conventional CS shows nearly the same performance as it returns equal number of pixel each time. The block agnostic shows the lowest error and the error improves significantly with the increase in data volume. For the EMD, the block agnostic shown in Figure 5-5 (b) shows better results and it signifies that the approach ensures both the amplitude and the shape of the target. Due to its bad performance, the DSBF is not shown in the EMD curves.

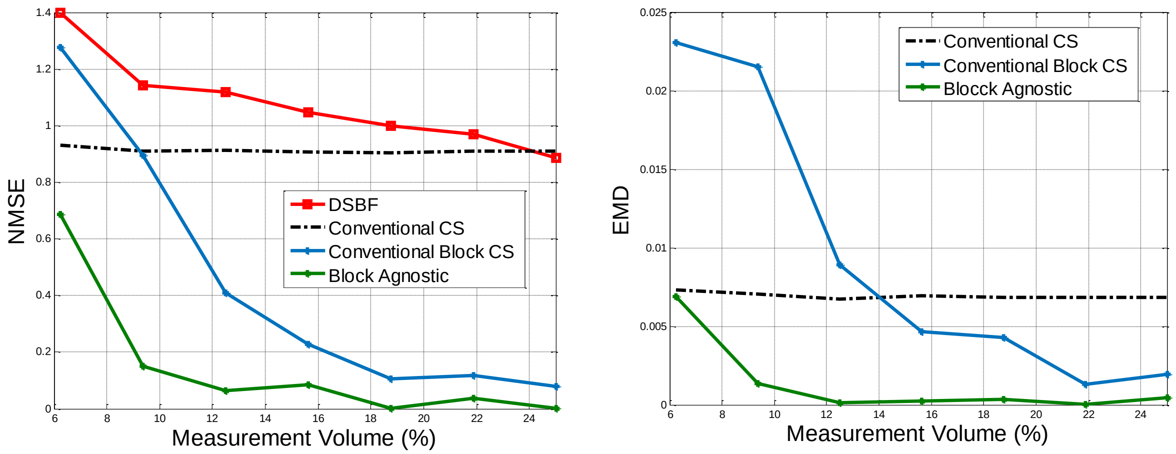

(a) (b)

Figure 5-5: Performance metrics (a) NMSE (b) EMD.

B. *Rayleigh Distributed Target Reflectivity*

In this case an ET whose pixels values are drawn from Rayleigh distribution is assumed as shown in Figure 5-6. Figure 5-6(a) shows the ground truth to be imaged and Figure 5-6(b) shows example of the pixel value distribution.

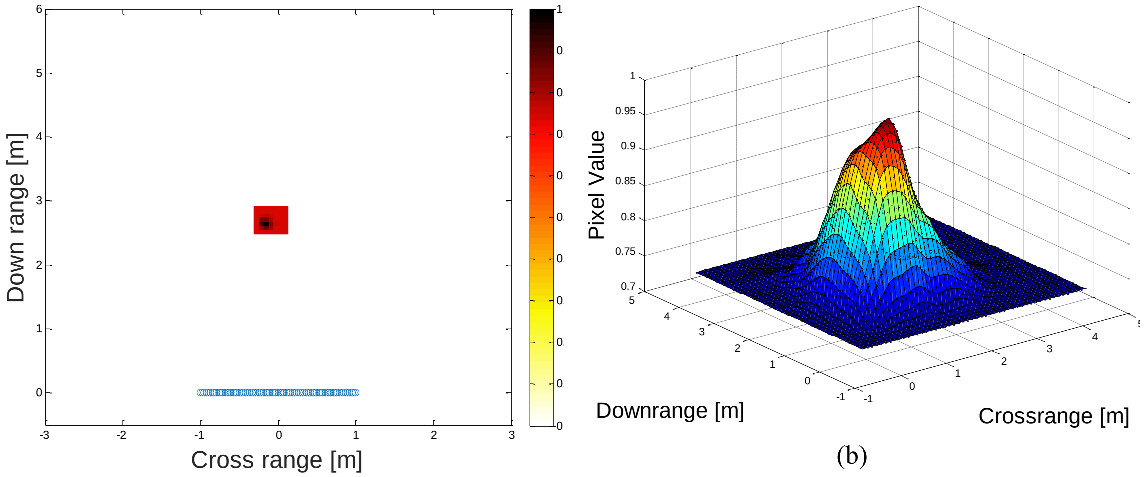

(a)

(b)

Figure 5-6: (a) the scene (b) pixel value distribution.

This distribution implies that the deeper the signal traverse the stronger it get reflected which represents a possible class of targets in TWRI applications. Similar measurement volume as in the previous case was used to capture the image. Again, the block agnostic shows a better image quality compared to other simulated methods. As non-agnostic Bayesian based reconstruction algorithms assume Gaussian distribution for the target amplitude, they are not considered here.

Figure 5-7 (a) shows the reconstructed image using DSBF with reduced data volume which is highly cluttered due to the point spread function and grating lobes artifacts. Figure 5-7 (b) is the conventional CS which works under PT assumption and does not well reconstruct the image which does not consider the pixel clustering. The reconstructed image using block agnostic is Figure 5-7 (d) outperforms the conventional block because block agnostic ensures the minimum error.

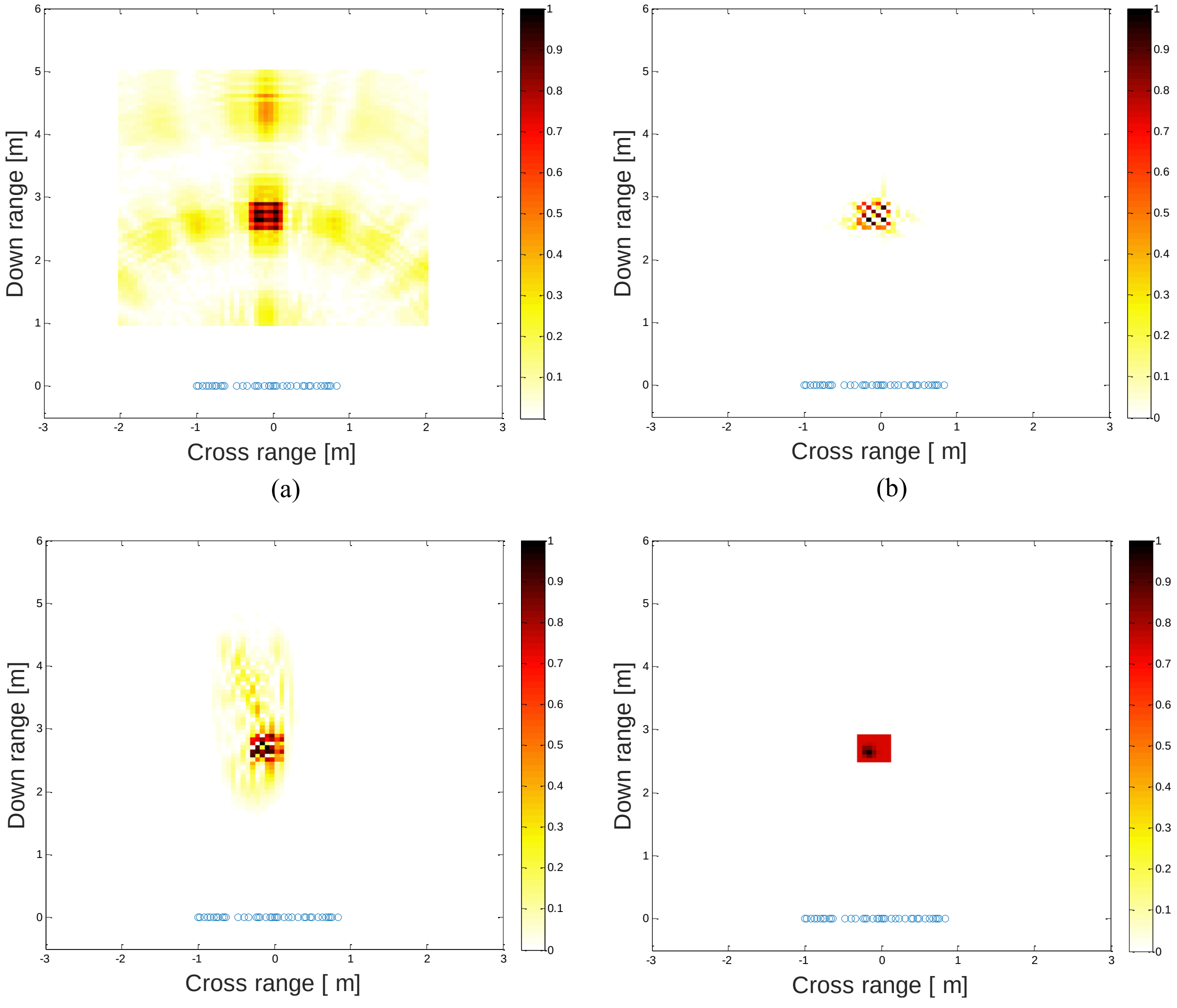

(a) (b)

(c) (d)

Figure 5-7: Images for Rayleigh Target (a) DSBF (b) Conventional CS (c) BOMP (d) Block Agnostic.

The qualitative performance measures: NMSE and EMD support the image qualities shown in Figure 5-8. Figure 5-8 (a) shows the variation of NMSE with measurement volume for different reconstruction approaches and the block agnostic shows good performance due to the fact that it always ensure the minimum error. Figure 5-8 (b) is the variation of EMD with data volume with DSBF excluded due to its worst case performance. Overall, the block agnostic approach shows better performance for both metrics.

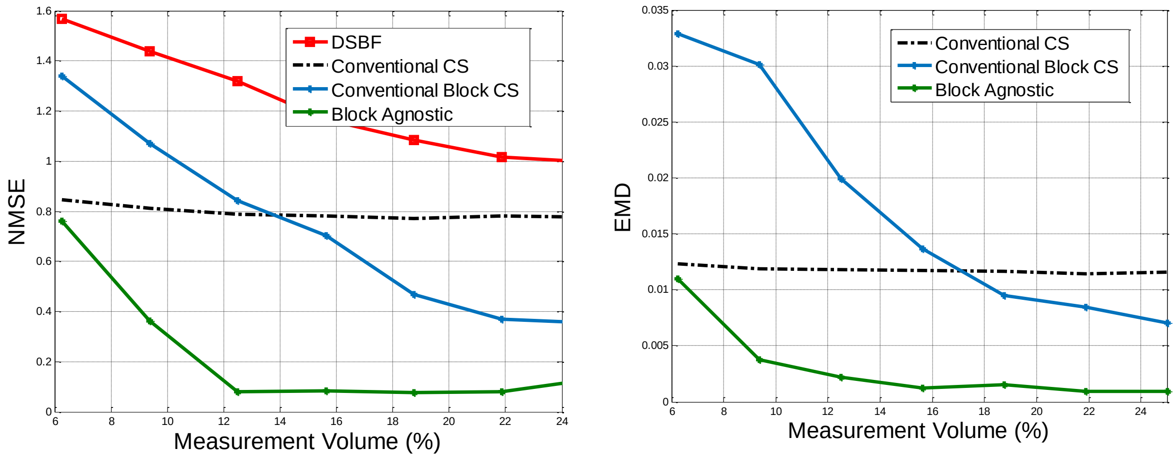

(a) (b)

Figure 5-8: Performance metrics for Rayleigh target (a) NMSE (b) EMD.

C. Joint ET and PT Reconstruction

Another advantage of the proposed reconstruction approach, block agnostic, is its ability to jointly reconstruct PTs and ETs by treating PTs as blocks of single pixel contrary to the previous approaches where the two are reconstructed separately. Consider a ground truth shown in Figure 5-9 containing both PTs and ET.

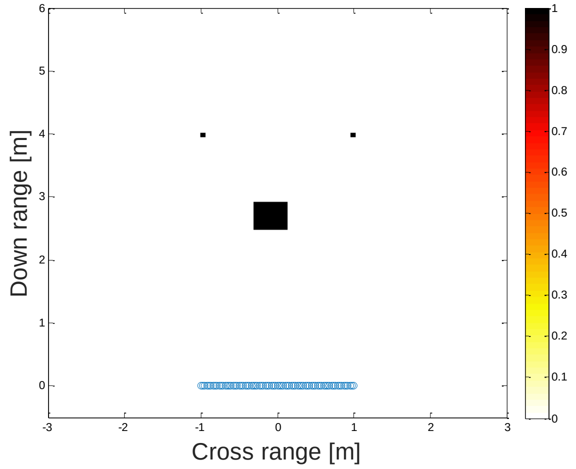

Figure 5-9: Original scene containing PT and ET.

The same amount of reduced data volume was used to capture the image of the scene and the block agnostic yield the best image quality as shown in Figure 5-10. The Figure 5-10

(a) is the image formed using DSBF and Figure 5-10 (b) is the reconstructed image using conventional CS approach. Figure 5-10 (c) is the reconstructed image with conventional block approach and Figure 5-10 (d) represents the reconstructed image with the block agnostic. All images were reconstructed under the same conditions for fair comparison.

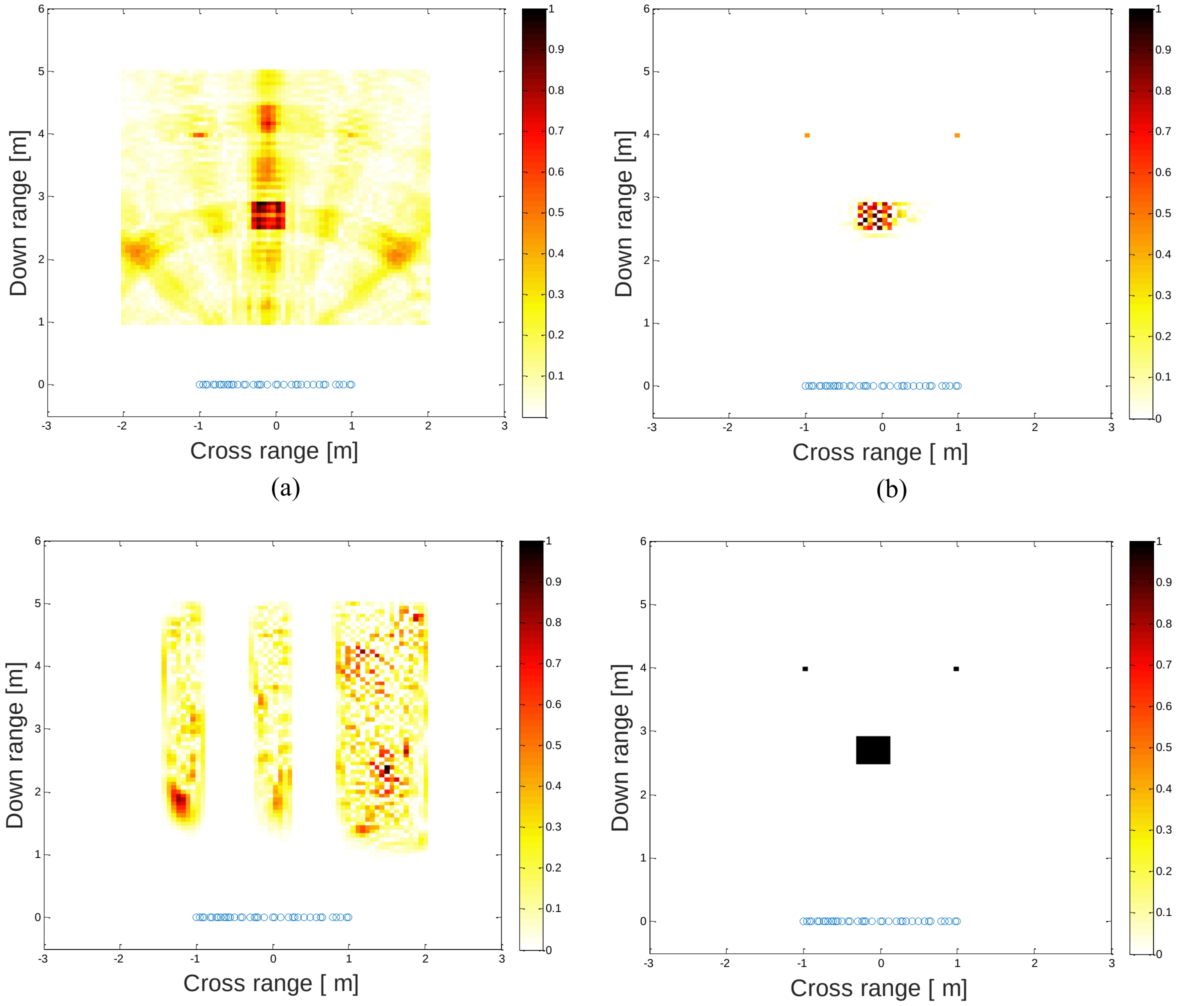

(a) (b)

(c) (d)

Figure 5-10: Images for ET-PT joint reconstruction (a) DSBF (b) Conventional CS (c) BOMP (d) Block Agnostic.

The NMSE and EMD averaged to 50 Monte Carlo runs are shown in Figure 5-11 (a) and (b), respectively, for different data volumes. Both metrics favor the block agnostic. The EMD curve for DSBF shows relatively low performance and it is not shown for clarity.

The curves suggest that the performance can be further improved with expense of increasing data volume.

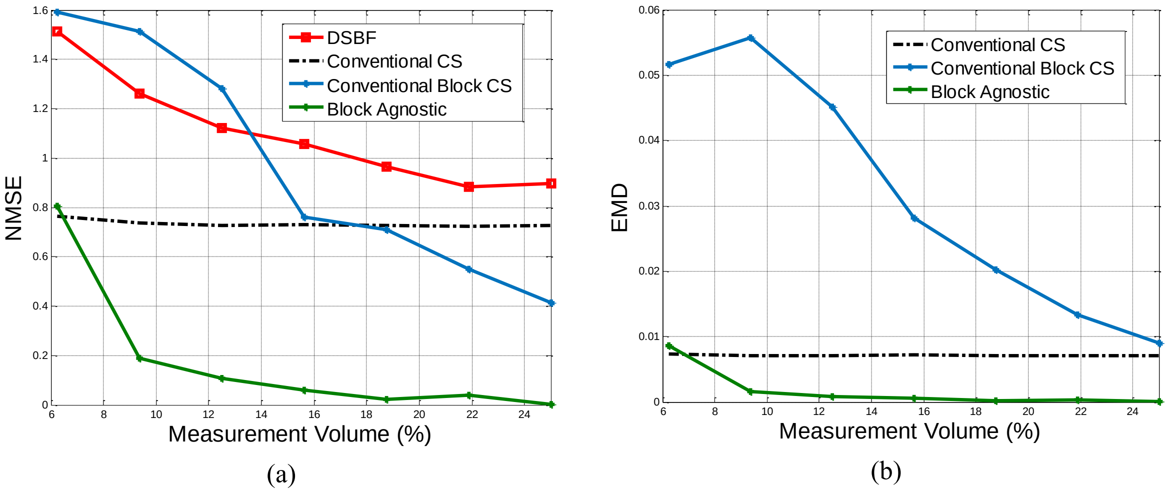

(a) (b)

Figure 5-11: Performance metrics for joint ET-PT reconstruction with data volume (a) NMSE (b) EMD.

D. ET Reconstruction under Multipath Environment

In this scenario, we simulate an ET in an enclosed room of $4 \times 4m^2$ with all walls covered but one due to the measurement constraint. As discussed earlier that in the presence of multipath, the scene becomes less sparse and therefore, may lower the performance of the CS algorithms. The effect becomes more pronounced here contrary to the PT counterpart where the target occupies only a single pixel.

The object of this subsection is twofold: examine the behavior of the proposed reconstruction approach under multipath and evaluate the effectiveness of the proposed ghost suppression for ETs case. A target described by 9 pixels was situated around the center of the room as shown in Figure 5-12 (a). Only 25% of the total measurement were utilized comprised of one half of both radar locations and frequency bins. The DSBF image is depicted in Figure 5-12 (b) for comparison.

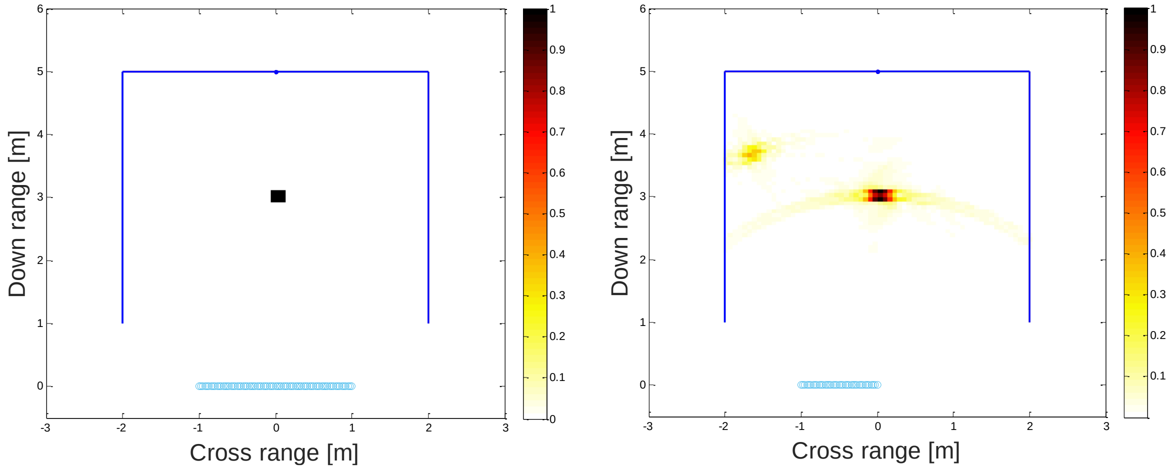

(a) (b)

Figure 5-12: Images under multipath environment (a) original scene (b) DSBF with ghost.

Two subimages were captured using two random subarrays collected from either side of the given array and their corresponding images are shown in Figure 5-13 (a)-(b). The final image following masking the two subimages is shown in Figure 5-13 (c) where the effect of multipath ghost is highly reduced. The simulation setup was repeated for the remaining walls but the conclusion remained the same. The performance of the AD ghost suppression method as presented in Chapter 3 found to decrease with the physical size of the target as the sparsity of the scene decreases with the target size.

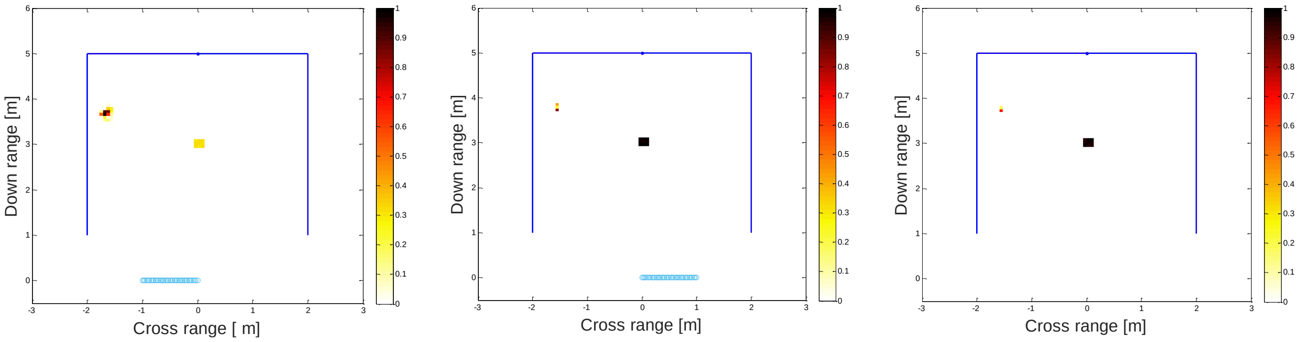

(a) (b) (c)

Figure 5-13: Reconstructed Images under multipath environment (a) Subarray1 (b) Subarray2 (c) Final. image

The NMSE and EMD of the final image were evaluated to quantify the performance and are summarized in Table 5-1. The final image shows the NMSE of about 6% and relatively smaller EMD indicating the close resemblance with the ground truth.

In the following subsection, the block agnostic is evaluated using real experimental data.

Table 5-1: NMSE and EMD for the initial and final images

	NMSE	EMD
Subarray-1	2.1135	17.0000e-04
Subarray-2	0.1028	3.5265e-04
Final Image fusing 1&2	0.0634	2.7127e-04

5.6.2. Experimental Results

An experiment was conducted involving two cylindrical targets of radius $23cm$ using similar experimental setup as in Section 3.4.2. With the resolution of 64×64 pixels, then the target occupies more than one pixel along the crossrange and downrange. Only 12.5% of the measurement volume was used to reconstruct the sparse images using both conventional CS, BOMP and block agnostic algorithms. The imaged area was restricted to $2 \times 3m^2$ reduce the effect of the multipath. Contrary to the conventional CS which failed to predict the extent of the target, the block agnostic algorithm gives more information about the target extent as shown in Figure 5-14 (d).

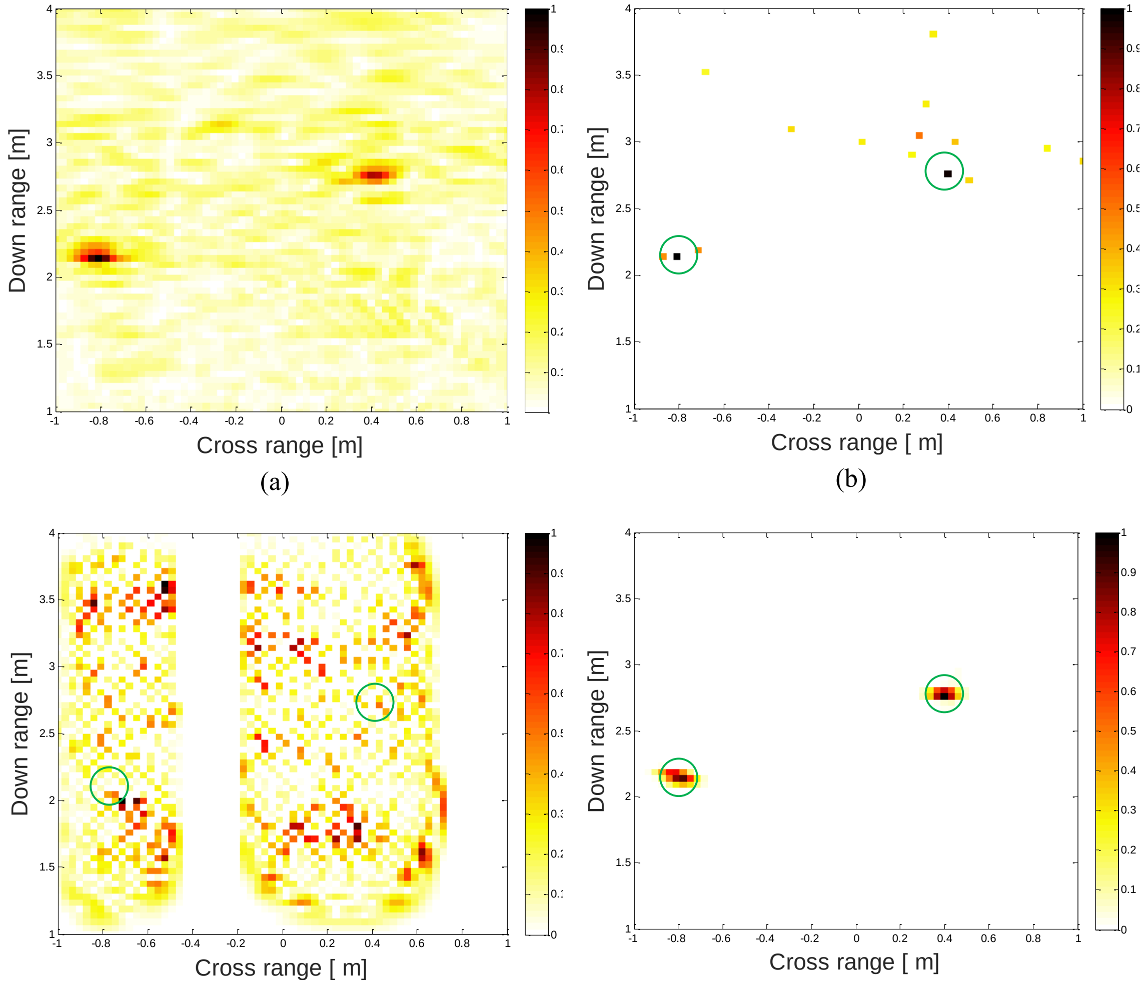

(a) (b)

(c) (d)

Figure 5-14: Images (a) DSBF (b) conventional CS (c) Conventional block sparse reconstruction (d) Block Agnostic.

5.7.Conclusions

In this chapter a different reconstruction algorithm for ETs is suggested based on block agnostic with varying block sizes. The overall ground truth is considered as a sum of disjoint ground truths with different target sizes, shapes and following different probability distributions. The model best reflect the TWRI scenarios where the expected targets may possess complex shapes which when vectorized by concatenating the columns of the discretized version of the ground truth, results into a vector with different block sizes. This feature enables the concurrent reconstruction of PTs and ETs by treating PTs as blocks with only one pixel. Further the model assumes that the distributions of the reflectivity values for the corresponding targets are not necessarily known. This is because in multiple and independent target scenario, consider the target being a human with rifle, then the resulting image vector comprises of chunks of pixels. Each chunk is drawn from different distributions making the overall pixel distribution intractable. Among other attractive features of the block agnostic, it reconstruct the scene using minimum mean squared error estimator which ensures the closest resemblance between the estimated scene and the true scene. Both qualitative and quantitative results based on MATLAB simulations and experimental data show the effectiveness of the block agnostic. However, the size of the target influence the overall performance as it lowers the sparsity of the scene particularly under multipath scenario.

In the subsequent chapter, a new localization scheme which utilizes the virtual radar information is suggested. The future of the scheme is be extended to imaging and reduce the amount of data significantly by incorporating virtual aperture and hence virtual measurement.

5.8.List of Publications

1. A. T. Abdalla, M. T. Alkhodary and A. H. Muqaibel, "Extended Target Modelling and Sparse Reconstruction in Through-the-Wall Radar Imaging: A Different Perspective", to be Submitted

“Deploying a physical or synthesized array aperture could be costly and logistically difficult compared to a less expensive and more flexible single-antenna radar system. In this case, one has to exploit multipath returns resulting from the EM interactions between targets and surrounding walls to enable cross-range estimations. The concept of exploitation is embedded in using the resolvable multipath to create virtual radar units at different locations dictated by the positions of both targets and walls”

Ali Muqaibel [100]

CHAPTER 6

INDOOR TARGET LOCALIZATION USING SINGLE MARGINAL ANTENNA WITH VIRTUAL RADARS SUPPORT

6.1.Introduction

In the last few decades, multipath effect was conceptualized negatively as it only causes signal fading in communication and introduces multipath ghosts in target localization and imaging. However, in modern radar technology, multipath components can be exploited to aid in target detection, tracking, classification, and imaging with increased SCR at genuine target locations [1], [3], [11], [19], [25], [54], [97]–[99]. Multipath exploitation proved itself to be beneficial in through the wall sensing especially in non-line of sight (NLOS) scenarios where the received signal contains only multipath components. Though, according to [2], [75], multipath exploitation in indoor localization has not been extensively studied yet.

In this chapter we present a novel localization method using single antenna and utilizing the multipath returns from virtual radars to localize an indoor target. The method is attractive as it uses only one UWB antenna with simple localization algorithm under smooth reflecting environment. Multipath returns are associated with their respective walls using a simplified residual based algorithm and localization is achieved by solving monostatic loci equations at each radar location for both real and virtual radars.

The rest of the chapter is organized as follows: Section 6.2 reviews the literature. Section 6.3 presents the multipath and received signal models. In Section 6.4, the proposed localization scheme is elaborated and the optimal radar location is developed. The wall association algorithm using a simplified formulation is also described herein and finally Section 6.7 summarizes the chapter.

6.2.Literature Review

In the literature, indoor targets are mainly localized using multipath exploitation with multi antenna or Synthetic Aperture Radar (SAR) systems [11], [19], [25], [97], [99]. Recently, few contributions have been presented utilizing a single antenna instead [54], [100]. Convincingly, localization with single antenna is more attractive as it enhances system flexibility and reduces the system cost greatly. With exception of [54] and [100] who used a single sensor, authors used multi-sensors or synthetic apertures with multipath exploitation to locate or track behind the wall targets.

Reference [11] proposed a SAR-based system to associate and map multipath ghosts to their corresponding true target locations in indoor imaging. In [97], the same authors utilized multipath exploitation to improve and maintain tracking of moving targets behind the walls. In the same year, authors in [25] incorporated MIMO radar system to detect hidden targets while [19] provided a method to localize multipath ghosts which was then used in target classification using multiple antenna array.

Reference [54] developed an algorithm using single-sensor to localize the target taking extra information from the multipath returns. As an extension of [3], in [100] the authors proposed a single-antenna localization scheme which exploits the embedded directivity in UWB antennas to enhance the localization process [100]. They considered first two arrivals and directivity of the antenna to reduce the number of possible target locations from 6 as in [54] down to 4. The main challenge facing the scheme in [54] is the complexity of the wall association algorithm to associate multipath returns with their respective walls.

In [100], their method relies on correlation between the received return and the set of possible signals which are synthesized in priori. In our contribution, we associate the received multipath to their respective walls in a much simpler manner.

This work introduces an effective way of localizing an indoor target using single UWB antenna with the help of Virtual Radars (VRs). VR is a result of the signal reflection from the interior wall, where the return path yields an alternative antenna-target configuration.

Due to their aspect dependence property, specular multipath components exist only at certain radar locations. We intuitively propose the best radar location so that it does not receive multipath return from the respective wall and hence reduces the wall ambiguity significantly. By observing only the direct and first order multipath returns, the target can be localized. In the literature, the target location is the point of intersection of two radar loci: a circle due to the direct return and an ellipses as a result of virtual bistatic configuration.

We consider only monostatic configuration about true and virtual radars. In this case the target location will be the intersection of circles of radii equal to their respective delays. The needed assumption is the knowledge of reflecting geometry which is also made in [54], [98] and [100]. The proposed scheme can be easily extended to 3D following the approach in [71].

6.3. Multipath Propagation Model

Consider the scene model in Figure 6-1 with a single radar, R_0, and three VRs , R_i , $i = 1, 2, 3$. Wall-1 is located along $x = 0$ and the radar system is along $y = 0$ at a distance, d_f from the wall, *standoff distance*. The room dimension is $D_1 \times D_2 m^2$. Let τ_0 represents the time elapsed from R_0 to the target located at $(-x_t, y_t)$.

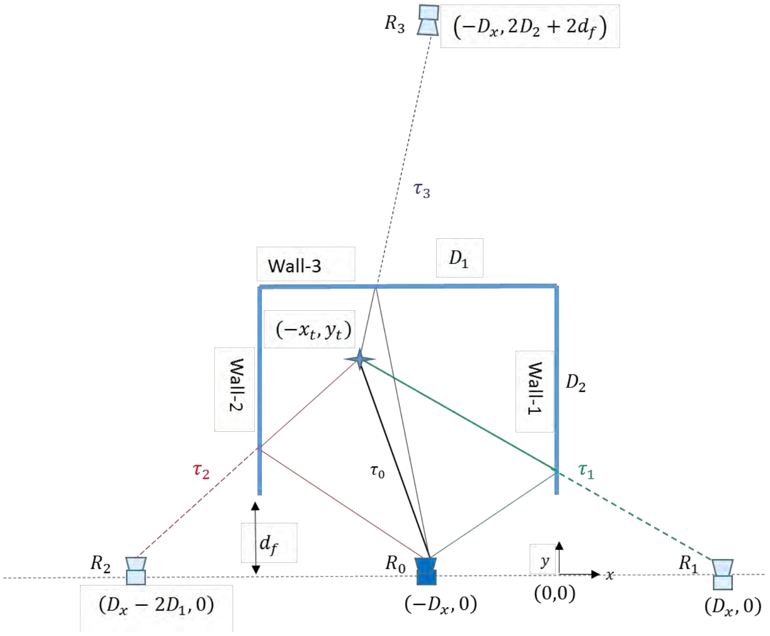

Figure 6-1: Multipath model with virtual radars.

If the radar transmits a UWB signal, $s(t)$, then the received signal, $y(t)$, in the presence of Gaussian noise, $v(t)$, is given by:

$$y(t) = \sum_{i=0}^{R-1} A_i s(t - t_i) + v(t) \tag{6-1}$$

where A_i and t_i are the amplitude and round-trip delay of the i^{th} multipath return, respectively. The time delay from the target to R_i associated with wall- i is defined as $\tau_i = t_i - {}^{t_0}/_{2}, i > 0$. When the signal is transmitted, four possible returns are assumed with the first being the direct return and subsequent ones are the single bounce returns from the walls. The question arises, which return is coming from which wall? In a single target scenario, there are 3! different possibilities of associating the received signal with available walls. We need a proper wall association without which, correct localization will be questionable. The wall association algorithm in [54] is complex particularly with an increased number of returns.

6.4.Proposed Localization Method

Multipath are aspect dependent and they may be observed only at certain radar locations. This characteristic can be utilized to aid in optimally locating the radar system such that the multipath effect is minimized.

6.4.1. Optimum Radar Location

Consider a straight line joining the given target and the VR located at $(D_x, 0)$ through a reflecting point on the wall-1 as shown in Figure 6-1. The equation describing this path is given by:

$$y = -\frac{y_t}{x_t + D_x}x + \frac{D_x y_t}{x_t + D_x} \tag{6-2}$$

The slope and y-intercept of (6-2) change with the radar location, D_x. As the radar moves towards wall-1, the last possible multipath from wall-1 is reflected at the edge of the given wall, at $(0, d_f)$. We need to determine a critical radar location, D_{xc}: a value below which no multipath from wall-1 will be observed by the radar, R_0. This is equivalent to finding D_x when the multipath falls on the edge of wall-1. From (6-2) we can write:

$$d_f = \frac{D_{xc} y_t}{x_t + D_{xc}} \tag{6-3}$$

$$\Rightarrow D_{xc} = \frac{x_t d_f}{y_t - d_f};\ y_t > d_f \tag{6-4}$$

From (6-4) the radar location to avoid multipath due to the presence of wall-1 is a function of target location, $(-x_t, y_t)$. That is, changing target location, the critical location changes for a given d_f. From (6-4), the minimum possible distance of critical location in the vicinity of the wall-1. Therefore, to reduce the effect of multipath due to the presence of wall-1 for all possible target locations, we locate the radar along the side wall, *marginal radar*.

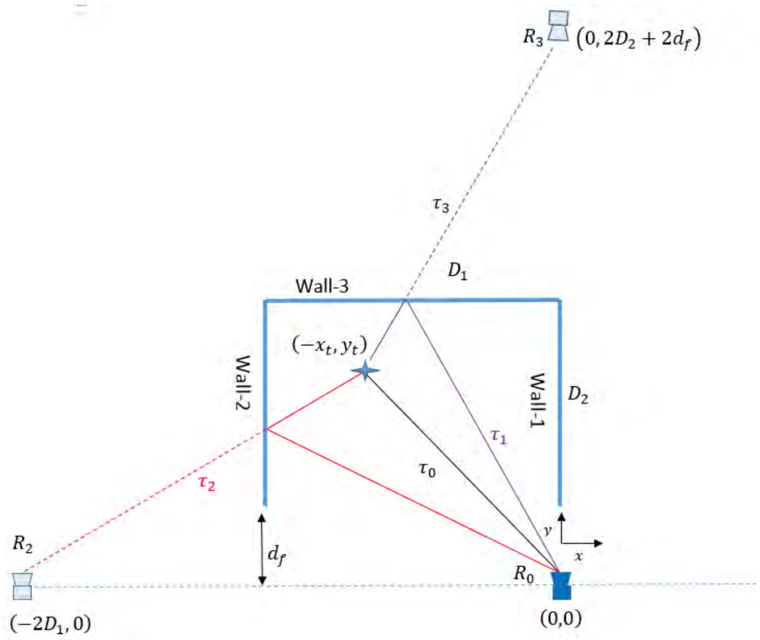

Figure 6-2: Marginal radar configuration.

6.4.2. Localization Scheme

Generally, if we place a radar system in the proximity of the known side wall as shown in Figure 6-2, at most two first order multipath returns from the remaining walls will be registered. This reduces the number of possible combinations from six to two provided that the direct arrival is received as depicted in Figure 6-3 which shows two possible sets of loci due to radar and VRs. In Figure 6-3 (a) we assume proper wall association and Figure 6-3 (b) represents incorrect wall association. If the first multipath return is due to the reflection from wall-2, the system of equations considering monostatic configurations about the radar and VRs as shown in Figure 6-3 (a) will be:

$$x_t^2 + y_t^2 = c^2\tau_0^2 \tag{6-5}$$

$$(2D_1 - x_t)^2 + y_t^2 = c^2\tau_2^2 \tag{6-6}$$

$$x_t^2 + \left(y_t - 2D_2 - 2d_f\right)^2 = c^2\tau_3^2 \tag{6-7}$$

where c is the speed of electromagnetic wave in free space. The target is located as the point of intersection of the three circles (6-5), (6-6) and (6-7).

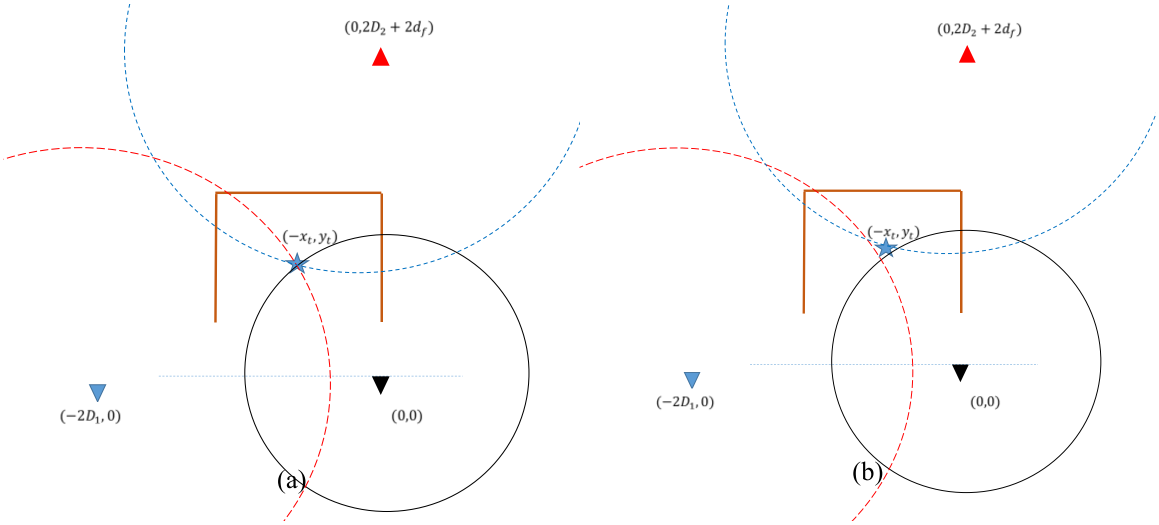

Figure 6-3: Two possible wall associations: (a) correct (b) incorrect.

If we consider the wrong association of the time delays to their respective walls, we solve (6-5), (6-6) and (6-7) with τ_2 and τ_3 interchanged as in Figure 6-3 (b). Multipath return due to the presence of wall-2 is position dependent and may not exist all along. However, the direct and back-wall returns always exist. Based on the geometry presented in Figure 6-2, the condition to have multipath from wall-2 is:

$$\frac{D_1 y_t}{(2D_1 - x_t)} > d_f \tag{6-8}$$

In the target positions where multipath due to wall-2 cannot be observed, it reduces the number of possible combination during wall association to only one as shown by the floor plan in Figure 6-4. In Figure 6-4, an exhaustive search of possible target locations was carried out to study the effect of target location to the complexity of the proposed scheme. The scene of around $6 \times 4m^2$ was descritized to 30×30 pixels and each pixel assumes a target location. In some locations within the room marked by 1, the condition in (6-8) is not met leading to one possible wall association which greatly reduces the complexity of the scheme. Otherwise, there are two possible wall associations which need to be examined for correct localization.

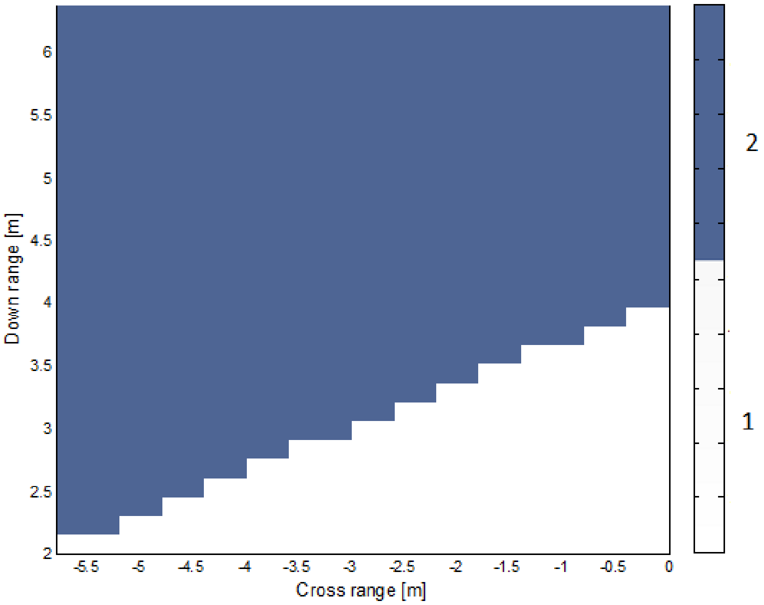

Figure 6-4: Regions showing the number of possible solutions.

Let $\boldsymbol{z}$ and $\boldsymbol{w}$ represent solutions when considering correct and incorrect time delays associations to the available walls, respectively. The solution will be valid if it satisfies equations (6-5)-(6-7).

Consider correct wall association scenario with $\boldsymbol{z}_{12} = (-x_t, y_t)$ representing the point of intersection of (6-5) and (6-6) and $\boldsymbol{z}_{13}$ is the intersection of (6-5) and (6-7). Ideally, the solution, $\boldsymbol{z}_{13}$ will be declared valid if $\boldsymbol{z}_{13} = \boldsymbol{z}_{12}$. In the presence of timing errors, the solution will be valid if and only if:

$$\|\boldsymbol{z}_{12} - \boldsymbol{z}_{13}\| = \delta_z \tag{6-9}$$

δ_z is the residual which shows the deviation of the two intersections $\boldsymbol{z}_{12}$ and $\boldsymbol{z}_{13}$, assuming correct wall association as shown in Figure 6-3(a). The selection of $\boldsymbol{z}_{12}$ and $\boldsymbol{z}_{13}$ is due to the fact that it is easier to estimate the direct arrival time than multipath returns and also the multipath from wall-2 does not exist for all possible target locations. This explains why z_{23}, is not a best candidate to consider for localization.

For a given received multipath, we need to find out from which wall it was generated. This scheme therefore, needs to examine both wall association scenarios as depicted in Figure 6-3. Solving (6-5) and (6-6) gives:

$$\boldsymbol{z}_{12} = \left(D_1 - \alpha, \sqrt{c^2\tau_2^2 - (D_1 + \alpha)^2}\right) \tag{6-10}$$

Similarly, solving (6-5) and (6-7) we have:

$$\boldsymbol{z}_{13} = \left(\sqrt{c^2\tau_3^2 - \left[D_2 + d_f + \beta\right]^2}, D_2 + d_f - \beta\right) \tag{6-11}$$

where $\alpha = \frac{c^2}{4D_1}(\tau_2^2 - \tau_0^2)$ and $\beta = \frac{c^2}{4(D_2+d_f)}(\tau_3^2 - \tau_0^2)$

For the wrong wall association, the corresponding solutions, $\mathbf{w}_{12}$ and $\mathbf{w}_{13}$ are similar to (6-10) and (6-11), respectively, with τ_2 and τ_3 interchanged. The residual of the wrong wall association, δ_w is equivalent to (6-9) with $\mathbf{z}$ replaced by $\mathbf{w}$.

To correctly associate the returns to their respective walls, δ_z needs to be smaller than δ_w. This gives a clear distinction of the correct wall association from incorrect one. For better performance, δ_z should be small enough and less than δ_w. The variation of residual with target location for the wrong hypothesis is shown in Figure 6-5. The horizontal axis represents possible target location along the crossrange and the vertical axis shows the target location along the range direction. The amount of residual is represented in color scale which increases from white to black as shown in the figure and interpreted by the color bar. It can be inferred from Figure 6-5 that along the diagonal of the given room, the residual value when considering the wrong association is minimal. In such scenarios, the wall association is no longer important. This is due to the symmetry with respect to delay times. In the lower right corner, no multipath is received from wall-2 and therefore, the residual is no longer important.

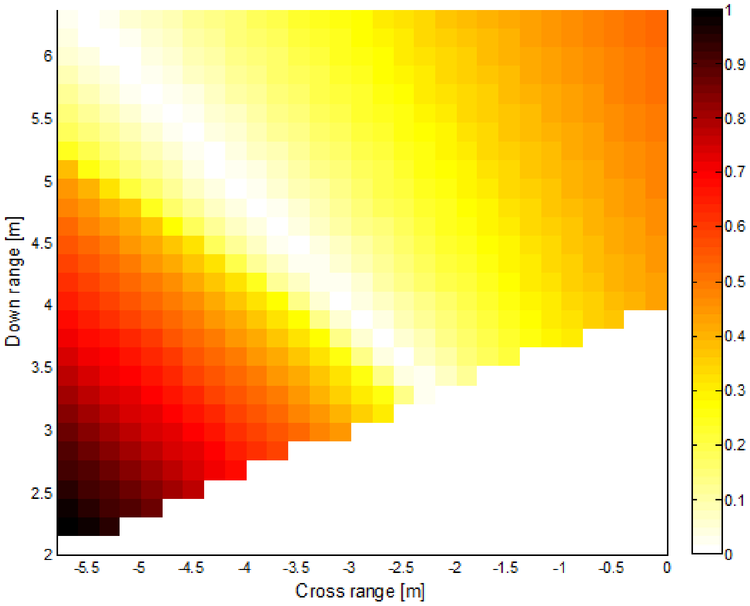

Figure 6-5: Variation of residual with target locations for wrong wall association.

6.5. Simulation Results

6.5.1. Target Localization

Simulating the scene model in Figure 6-2, with a target at $(-3.69, 3.6)\ m$, randomly located. The right and left sidewalls are located at the origin and at a crossrange of $-5.8m$, respectively. The back wall resides at $6.37m$ downrange. A UWB signal of bandwidth $2GHz$ shown in Figure 6-6 was transmitted and received by the radar located along the right wall at a standoff distance of $2m$. The direct return, the first and second reflections associated with the two walls were recorded as depicted in Figure 6-7. The time delay between the radar and the target, $\tau_0 = 17.18ns$, the time delay associated with the two VRs, $\tau_2 = 52.36ns$ and $\tau_3 = 32.86ns$.

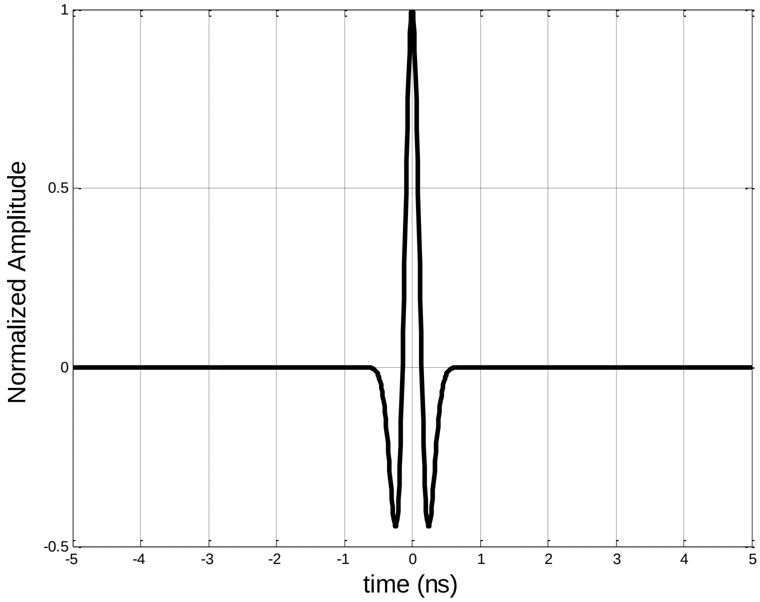

Figure 6-6: UWB transmitted signal.

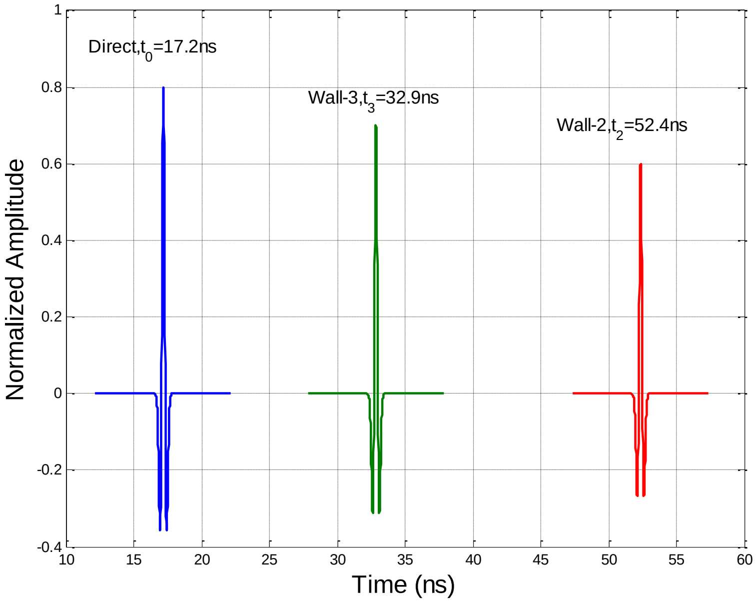

Figure 6-7: Received signal with multipath.

When the delays are incorrectly associated to their respective walls, the target was incorrectly localized as shown in Figure 6-8. The figure shows the location of the target when the delays are correctly and incorrectly associated to their respective walls. The correct ordering of the delays is achieved by evaluating the residuals in (6-9) for the two possible arrival sequences. Under ideal condition, δ_z is expected to be negligible and less than δ_w except when the target lies along the diagonal of the room joining the radar. In such a case, wall association is no longer needed. It is desired that the residual varies slowly when the system is subjected to timing errors. Once the wall association is achieved, the target location is given by (6-11). Sensitivity of the residual value can be taken as a reasonable performance measure of the localization scheme.

The received signal is pre-processed to mitigate the contribution of the front wall as in [44]–[46], [48].

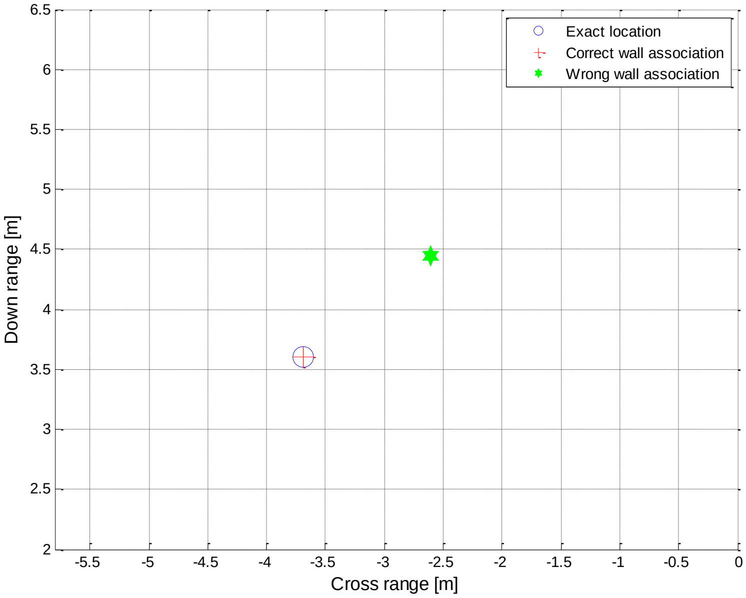

Figure 6-8: Target localization with and without correct wall association.

6.5.2. Sensitivity Due to Timing Errors

To evaluate the performance of the proposed scheme, 1000 randomly generated target positions were localized individually. Due to limited bandwidth and limited SNR, an additive timing measurement error was assumed from $-3ns$ to $3ns$ to investigate the robustness of the proposed method. Timing error in this context refers to the time difference between the expected pulse location and the observed one. The variation of residual values with timing errors is shown in Figure 6-9. The figure shows three possible cases for the timing errors of the corresponding delays. From the results, it is noted that the amount of residual for correct wall association is more sensitive to multipath return from the back wall and less affected by the multipath return due to side wall as shown in Figure 6-9 (a) - (c). In Figure 6-9, it is assumed that the remaining returns are correctly registered.

As long as $\delta_z < \delta_w$, the scheme associates the registered delays correctly to their respective walls and the probability of correct localization increases. It can be deduced from the graph that the scheme is robust over a reasonable range of timing errors.

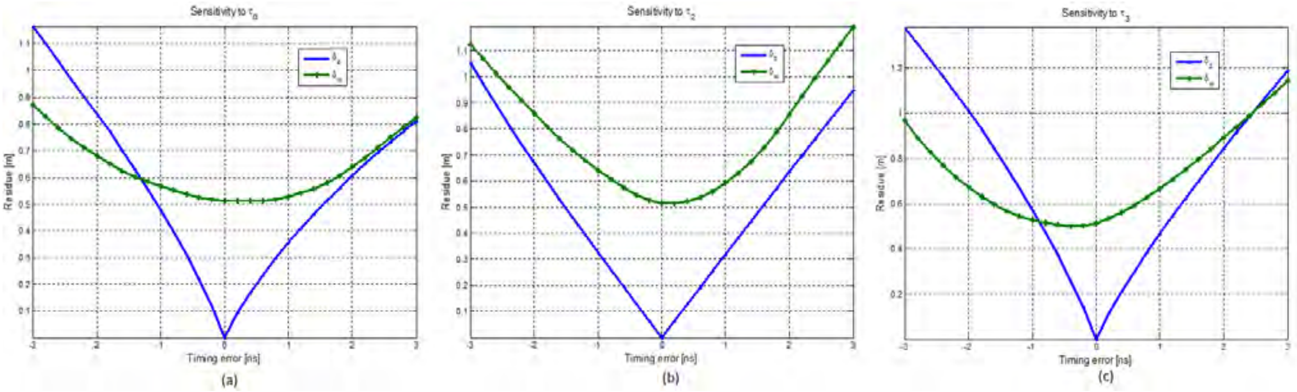

Figure 6-9: Variation of residuals with timing error (a) τ_0 (b) τ_2 (c) τ_3.

6.5.3. Localization Error

Even when perfect wall association is achieved, we need to investigate the localization error of the proposed scheme in the presence of timing error

Let $\Delta\tau_0$, and $\Delta\tau_3$ represent the timing errors associated with direct return, and return from the back wall, respectively. Suppose that the estimated target location is $(x_t + \Delta x_t, y_t + \Delta y_t)$. The possible error in crossrange direction is given by:

$$\Delta x_t = \left|\frac{\partial x_{13}}{\partial \tau_0}\right| \Delta\tau_0 + \left|\frac{\partial x_{13}}{\partial \tau_3}\right| \Delta\tau_3 \tag{6-12}$$

Similarly, the possible downrange error is:

$$\Delta y_t = \left|\frac{\partial y_{13}}{\partial \tau_0}\right| \Delta\tau_0 + \left|\frac{\partial y_{13}}{\partial \tau_3}\right| \Delta\tau_3 \tag{6-13}$$

From (6-12) and (6-13), the maximum location error, Δr: the displacement of the estimated target from the exact location, given by:

$$\Delta r = \sqrt{\Delta x_t^2 + \Delta y_t^2} \tag{6-14}$$

The expressions for the partial derivatives in (6-12) and (6-13) can be shown to be:

$$\frac{\partial x_{13}}{\partial \tau_0} = \frac{\dfrac{c^2}{2\left(D_2 + d_f\right)}\left(D_2 + d_f + \beta\right)\tau_0}{\sqrt{c^2\tau_3^2 - \left(D_2 + d_f + \beta\right)^2}} \tag{6-15}$$

$$\frac{\partial x_{13}}{\partial \tau_3} = \frac{c^2\tau_3 - \dfrac{c^2}{2\left(D_2 + d_f\right)}\left(D_2 + d_f + \beta\right)\tau_3}{\sqrt{c^2\tau_3^2 - \left(D_2 + d_f + \beta\right)^2}} \tag{6-16}$$

$$\frac{\partial y_{13}}{\partial \tau_0} = \frac{c^2}{2\left(D_2 + d_f\right)}\tau_0 \tag{6-17}$$

$$\frac{\partial y_{13}}{\partial \tau_3} = -\frac{c^2}{2\left(D_2 + d_f\right)}\tau_3 \tag{6-18}$$

Figure 6-10 shows the variation of maximum location error with timing errors due to direct and back-wall returns. The horizontal axis indicates the variation of the timing error due to the direct return and the vertical axis shows the variation of the timing error due to the back wall. The value of the error is represented in color scale increasing from white to black as shown and interpreted by the color bar. It can be inferred that the scheme is stable over wide range of timing errors. The location error is more pronounced when the timing errors change in the same directions. From the expressions of partial errors, we can also deduce that we can localize more accurately when the room is large.

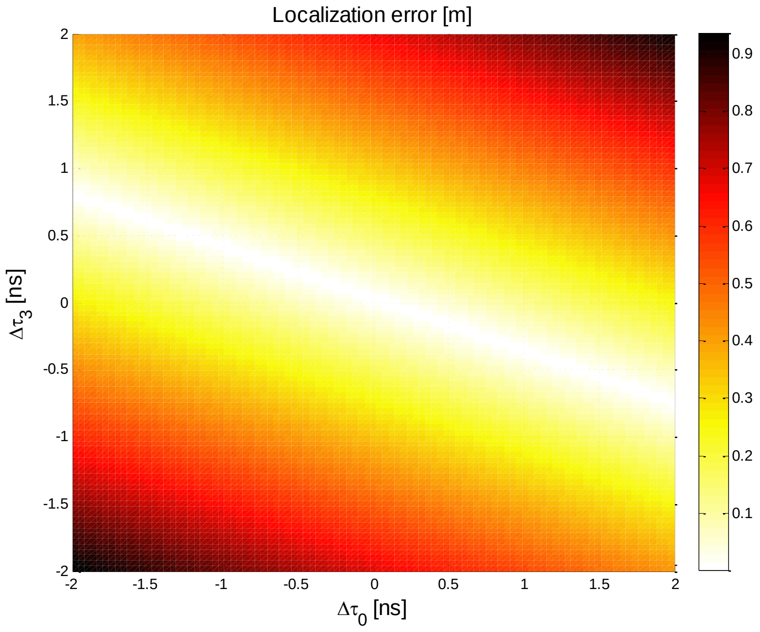

Figure 6-10: Variation of localization error with timing errors.

6.6. Conclusion

In this chapter, we proposed a target localization scheme with single marginal transceiver which takes into account the information from the VRs. Based on aspect dependence of multipath returns, the antenna was located in the vicinity of the side wall to minimize wall ambiguity and reduces the number of possible solutions making the scheme more efficient. The correct wall association was made possible by considering three monostatic configurations: using the real radar and two VRs. The analytical solution for the possible target location was obtained. To ensure the maximum number of needed returns for localization, pre-processing the received signal might be needed including the thresholding and time gating. The effectiveness and robustness of the proposed scheme were shown using mathematical derivation and simulation results. It was shown through simulated measurement that the scheme is robust to wide range of timing errors. The idea and formulation of the problem can be extended to localize multiple targets under given conditions.

6.7.List of Publications

1. A. T. Abdalla and Ali. H. Muqaibel, "Indoor target localization using marginal antenna with virtual radars support", to be submitted

“The pursuit of knowledge is never-ending. The day you stop seeking knowledge is the day you stop growing”

Brandon Travis Ciaccio

CHAPTER 7

CONCLUSIONS AND RECOMMENDATIONS FOR FUTURE DIRECTIONS

This chapter summarizes the main contributions of this dissertation and suggests the expected directions for the future works.

7.1. Summary of the Contributions

The dissertation contributions with their corresponding publications are summarized as follows:

7.1.1. Ghost Suppression Method Exploiting Aspect Dependence with Compressive Sensing

We proposed a new multipath ghost suppression method in TWRI which exploit the AD feature under CS framework. The exploitation of this peculiar feature reduces the size of the sensing matrix drastically compared to the recently published work in the same track as the image reconstruction requires only direct returns information. Besides, the method relaxes the constraint of the knowledge of the reflecting geometry as suggested in the recent literatures. We propose a measurement procedure using strategically selected duo-subaperture to realize the AD feature and then suppress ghost's artifacts. CS is employed to reconstruct the corresponding scenes. Results based on MATLAB simulation and real experiments show the effectiveness of the proposed method.

7.1.2. Pythagorean Based Coprime Arrays

In this work, we proposed sparse arrays based on PPT coprime integers to replace random based subapertures. Coprime based arrays are known to increase the DoF in DOA problems and therefore, may ensure sufficient multipath resolvability in TWRI problems with design simplicity advantage. We used the fact that Pythagorean triple are pairwise coprime numbers and their squares also pairwise coprime which helps to design arrays with sufficient number of active elements and yet with feasible lengths. Results based on MATLAB simulation and specialized software package show the effectiveness of the proposed array configurations.

7.1.3. Extended Target Modelling and New Reconstruction Perspective in TWRI

We proposed a generalized signal model for ETs in TWRI applications. In this case, we formulated the scene as a group sparse vector with unknown group sizes and agnostic to target distributions. The posed conditions on the behind the wall scene are justifiable as in some applications we have multiple extended targets having different reflectivity values and distributions which are not usually known. Even if the distribution of each extended target pixels is known but vectorizing the scene will result into a vector with complex distribution. The problem was formulated under the newly developed reconstruction algorithm, Support Agnostic Bayesian Matching Pursuit (SABMP).

7.1.4. Target Localization Scheme Exploiting Virtual Radars

We came up with a single antenna based indoor target localization method exploiting virtual radars. This was possible due to aspect dependence property of specular multipath components which do exist only at certain radar locations. The use of marginal radar has reduced the wall ambiguity and lowered the computational complexity significantly compared to the latest published similar approaches. Simulation results show that the method is robust to the timing errors and can localize with good accuracy.

7.1.5. Signal Model

A comprehensive received signal model has been introduced that collectively considers the front wall reflections and reverberations, the side-wall reflections and target-to-target interactions as well. In CS based approaches, the target-to-target interaction has been ignored due to nonlinear behavior. In this work, we have modeled the target-to-target interaction component as a linear component by imposing additional but justifiable assumptions.

7.1.6. Image Fusion Techniques

When performing multiple imaging, the subimages were fused to yield a final image using masking approach. In this work we also examined two image fusion strategies which outperform the traditional image masking approach. The first approach based on weighted Sum of the individual subimages. It is a two-step approach whereby an intermediate image is first defined which takes the weighted sum of the subimages such that it minimizes the clutter norm and maintain the true targets casting it as an optimization problem. Then the intermediate image is masked with the individual.

The second approach based on harmonic mean of the individual subimages. The fact that harmonic mean of a list of numbers leans towards the least elements of the list and maintains the same value for equal elements, can be utilized to suppress large clutters in TWRI while it maintains the true targets. So, the harmonic mean of the individual forms an intermediate image which then masked with individual subimage.

7.2.Future Directions

Multipath ghosts not only cause confusion with the genuine targets but populate the scene rendering it less sparse which deteriorate the performance of CS. The current trend to suppress the ghosts in TWRI literature is based on post image processing. The image is first reconstructed and then the ghosts are identified and suppressed. To enhance the CS algorithms, ghost suppression methods based on pre-processing are urgently needed. The effect of multipath should be suppressed prior to the image reconstruction. Further, considering the time history and moving targets are possible extensions for the work.

This work proposed the use of sparse arrays in TWRI applications based on PPTs. The proposal to use Pythagorean triples in imaging is fresh and further theoretical analysis is needed. Further research can be conducted to study the optimal configuration in 2D and propose the best arrangement for TWRI applications. Further, experimental validation is also needed to support the claims.

As the Block SABMP extends the block of pixels in one direction, a more general algorithm which extends in two dimensions is needed for the performance improvement.

In this work, a method to localize a single target by exploiting multipath returns from VRs has been presented. This method laid a foundation on which a more general framework can be developed to incorporate multiple targets. A further research is also needed to exploit VRs for imaging in which case the size of the physical aperture may be reduced and therefore, reduces data acquisition time and memory demand.

With availability of measurement equipment, more experimental data are needed. The data available on the database by Villanova does not account for the multipath effect and therefore not suitable for multipath suppression and/or exploitation related problems.

Moreover, considering more complicated channel models that account for path-loss, antenna directivity, and target angular reflectivity are among the suggestions

REFERENCES

[1] M. Leigsnering, F. Ahmad, M. Amin, and A. Zoubir, "Multipath exploitation in through-the-wall radar imaging using sparse reconstruction," *IEEE Trans. Aerosp. Electron. Syst.*, vol. 50, no. 2, pp. 920–939, 2014.

[2] P. Setlur, G. Alli, and L. Nuzzo, "Multipath exploitation in through-wall radar imaging via point spread functions.," *IEEE Trans. Image Process.*, vol. 22, no. 12, pp. 4571–86, Dec. 2013.

[3] J. Z. B., Chakraborty, Y. Li, "Multipath exploitation with adaptive waveform design for tracking in urban terrain," in *Acoustics Speech and Signal Processing (ICASSP)*, 2010, pp. 3894–3897.

[4] Z. Li, K. Lingjiang, J. Yong, Z. Zhongxing, and F. Lan, "A novel approach of multi-path suppression based on sub-aperture imaging in through-wall-radar imaging," in *IEEE Radar Conference (RADAR)*, 2013, no. 61201276, pp. 4–7.

[5] J. L. Krolik, J. Farrell, A. Steinhardt, and N. F. Drive, "Exploiting multipath propagation for GMTI in urban environments," in *IEEE Conference on Radar*, 2006, pp. 65–68.

[6] A. T. Abdalla, A. H. Muqaibel, and S. Al-dharrab, "Aspect Dependent Multipath Ghost Suppression in TWRI under Compressive Sensing Framework," in *International Conference on Communications, Signal Processing and their Applications (ICCSPA15)*, 2015.

[7] M. Leigsnering, F. Ahmed, M. Amin, and A. M. Zoubir, “Compressive Sensing Based Multipath Exploitation for Stationary and Moving Indoor Target Localization,” *IEEE J. Sel. Top. signal Process. to Appear*, 2015.

[8] M. Leigsnering, M. G. Amin, F. Ahmad, and A. M. Zoubir, “Multipath exploitation and suppression for SAR imaging of building interiors [An overview of recent advances],” *Signal Process. Mag. IEEE*, vol. vol.31, no. 4, pp. 110–119, 2014.

[9] R. Linnehan and J. Schindler, “Multistatic scattering from moving targets in multipath environments,” *2009 IEEE Radar Conf.*, vol. 1, pp. 1–6, 2009.

[10] Y.-S. Yoon and M. Amin, “High resolution through-the-wall radar imaging using extended target model,” in *Radar Conference, 2008. RADAR ’08. IEEE*, 2008, pp. 1–4.

[11] P. Setlur, M. Amin, and F. Ahmad, “Multipath model and exploitation in through-the-wall and rrban radar sensing,” *IEEE Trans. Geosci. Remote Sens.*, vol. 49, no. 10, pp. 4021–4034, Oct. 2011.

[12] Q. Tan, “A new method for multipath interference suppression in through-the-wall UWB radar imaging,” in *2nd International Conference on Advanced Computer Control, Shenyang China,* 2010, no. 2, pp. 535–540.

[13] Q. Tan, H. Leung, Y. Song, and T. Wang, “Multipath ghost suppression for through-the-wall radar,” *IEEE Trans. Aerosp. Electron. Syst.*, vol. 50, no. 3, pp. 2284–2292, Jul. 2014.

[14] P. Setlur, M. Amin, and F. Ahmad, “Multipath model and exploitation in through-

the-wall and urban radar sensing," *IEEE Trans. Geosci. Remote Sens.*, vol. 49, no. 10, pp. 4021–4034, 2011.

[15] P. Setlur, N. Tadahiro, N. Devroye, and D. Erricolo, "Multipath Exploitation in Non-LOS Urban Synthetic Aperture Radar," *IEEE J. Sel. Top. Signal Process.*, vol. 8, no. 1, pp. 137–152, 2014.

[16] H. T. Hayvaci, P. Setlur, N. Devroye, and D. Erricolo, "Maximum likelihood time delay estimation and Cram′er-Rao bounds for multipath exploitation," in *IEEE Radar Conference*, 2012, vol. 1, pp. 764–768.

[17] H. T. Hayvaci, "Improved radar target time-delay estimation with multipath exploitation," in *IEEE International conference on electromagnetic in advanced applications*, 2013, vol. 1, pp. 1232–1235.

[18] H. T. Hayvaci, A. De Maio, and D. Erricolo, "Improved detection probability of a radar target in the presence of multipath with prior knowledge of the environment," *IET Radar, Sonar Navig.*, vol. 7, no. 1, pp. 36–46, Jan. 2013.

[19] G. E. Smith and B. G. Mobasseri, "Multipath exploitation for radar target classification," in *2012 IEEE Radar Conference*, 2012, pp. 0623–0628.

[20] M. Leigsnering, F. Ahmad, M. Amin, and A. Zoubir, "Compressive sensing based specular multipath exploitation for through-the-wall radar imaging," in *IEEE International Conference on Acoustics, Speech and Signal Processing (ICASSP)*, 2013, pp. 6004–6008.

[21] Q. Wu, Y. D. Zhang, M. G. Amin, and F. Ahmad, "Through-the-wall radar imaging

based on modified Bayesian compressive sensing," *2014 IEEE China Summit Int. Conf. Signal Inf. Process.*, pp. 232–236, Jul. 2014.

[22] G. Gennarelli and F. Soldovieri, "Multipath Ghosts in Radar Imaging: Physical Insight and Mitigation Strategies," *IEEE J. Sel. Top. Appl. Earth Obs. Remote Sens.*, vol. 8, no. 3, pp. 1078–1086, 2015.

[23] D. Garren, "SAR image formation uncorrupted by multiple-bounce artifacts," *Proc. 2002 IEEE Radar Conf. (IEEE Cat. No.02CH37322)*, pp. 338–343.

[24] D. Garren, D. Sullivan, J. North, and J. Goldstein, "Image preconditioning for a SAR image reconstruction algorithm for multipath scattering," in *IEEE International Radar Conference, 2005*, 2005, pp. 300–305.

[25] D. Deiana, A. S. Kossen, and W. L. Van Rossum, "Multipath exploitation in an urban environment using a MIMO surveillance radar," in *IEEE 11th Radar symposium*, 2010, pp. 1–4.

[26] L. Li and J. L. Krolik, "Vehicular MIMO SAR imaging in multipath environments," *2011 IEEE RadarCon*, vol. 5, no. 2, pp. 989–994, May 2011.

[27] M. S. Mercan and E. Öztürk, "Through wall imaging based on MIMO UWB radar with a fast image reconstruction method," in *IEEE Radar Conference,* 2013, pp. 29–32.

[28] F. Ahmad, M. Amin, S. Kassam, and G. Frazer, "A wideband, synthetic aperture beamformer for through-the-wall imaging," *IEEE Int. Symp. Phased Array Syst. Technol. 2003.*, pp. 187–192, 2003.

[29] F. Ahmad, M. Amin, and S. Kassam, “Synthetic aperture beamformer for imaging through a dielectric wall,” *IEEE Trans. Aerosp. Electron. Syst.*, vol. 41, no. 1, pp. 271–283, 2005.

[30] H. Mansour and D. Liu, “Blind multi-path elimination by sparse inversion in through-the-wall-imaging,” in *IEEE 5th International Workshop on Computational Advances in Multi-Sensor Adaptive Processing (CAMSAP)*, 2013, pp. 256–259.

[31] J. Wang, P. Wang, Y. Li, Q. Song, and Z. Zhou, “A multipath suppression technique for through-the-wall radar,” in *2013 IEEE International Conference on Ultra-Wideband (ICUWB)*, 2013, pp. 215–220.

[32] A. T. Abdalla and A. H. Muqaibel, “Multiple Target Sparse Reconstruction in TWRI Utilizing Ghost’s Aspect Dependence Feature,” in *2015 IEEE International RF and Microwave Conference*, 2015.

[33] A. T. Abdalla and A. H. Muqaibel, “Single-View Bistatic Sparse Reconstruction in TWRI Exploiting Ghost’s Aspect Dependence Feature,” in *IEEE Wireless Communications and Networking Conference*, 2016.

[34] A. H. Muqaibel, A. T. Abdalla, and S. Al-dharrab, “Aspect dependent efficient multipath ghost suppression in TWRI with compressive sensing,” *J. Radioengineerring,submitted*, 2015.

[35] A. T. Abdalla and A. H. Muqaibel, “Through-the-Wall Radar Imaging Exploiting Pythagorean Coprime-Based Synthetic Apertures with Sparse Reconstruction,” *J. Digit. Signal Process. Submitt.*, 2016.

[36] A. T. Abdalla and A. H. Muqaibel, "Indoor target localization using marginal antenna with virtual radars support," *Arab. J. Sci. Eng. Submitt.*, 2015.

[37] S. E. Hamran, "Radar Performance of Ultra Wideband Waveforms," in *Radar Technology*, G. Kounemou, Ed. INTECH, 2009.

[38] W. Zhang, M. G. Amin, F. Ahmad, A. Hoorfar, and G. E. Smith, "Ultrawideband impulse radar through-the-wall imaging with compressive sensing," *Int. J. Antennas Propag.*, vol. 2012, p. 11, 2012.

[39] M. J. Oyan, S.-E. Hamran, L. Hanssen, T. Berger, and D. Plettemeier, "Ultrawideband Gated Step Frequency Ground-Penetrating Radar," *Geosci. Remote Sensing, IEEE Trans.*, vol. 50, no. 1, pp. 212–220, 2012.

[40] X. Raimundo, "FMCW Signals for Radar Imaging and Channel Sounding," Durham University, 2015.

[41] E. Lagunas, "Compressive Sensing Based Candidate Detector and its Applications to Spectrum Sensing and Through-the-Wall Radar Imaging," Universitat Polit`ecnica de Catalunya, 2014.

[42] L. Nguyen, "Image Resolution Computation for Ultra-Wideband (UWB) Synchronous Impulse Reconstruction (SIRE) Radar," 2007.

[43] Y. Teng, H. Griffiths, C. Baker, and K. Woodbridge, "Netted radar sensitivity and ambiguity," *IET Radar, Sonar Navig.*, vol. 1, pp. 479–486, 2007.

[44] F. Tivive, A. Bouzerdoum, and M. Amin, "A Subspace Projection Approach for Wall Clutter Mitigation in Through-the-Wall Radar Imaging," *IEEE Trans. Geosci.*

Remote Sens., vol. 53, no. 4, pp. 2108–2122, 2015.

[45] Y.-S. Yoon and M. Amin, "Spatial filtering for wall-clutter mitigation in through-the-wall radar imaging," *IEEE Trans. Geosci. Remote Sens.*, vol. 47, no. 9, pp. 3192–3208, Sep. 2009.

[46] F. Tivive, M. G. Amin, and A. Bouzerdoum, "Wall clutter mitigation based on eigen-analysisin through-the-wall radar imaging," in *Proc. IEEE Workshop on DSP*, 2011, pp. 1–8.

[47] A. Karousos, G. Koutitas, and C. Tzaras, "Transmission and reflection coefficients in time-domain for a dielectric slab for UWB signals," *VTC Spring 2008 - IEEE Veh. Technol. Conf.*, pp. 455–458, May 2008.

[48] E. Lagunas, M. G. Amin, F. Ahmad, and M. Nájar, "Wall mitigation techniques for indoor sensing within the compressive sensing framework," *IEEE Trans. Geosci. Remote Sens*, vol. 51, no. 2, pp. 891–906, 2013.

[49] F. Ahmad and M. G. Amin, "Multi-location wideband synthetic aperture imaging for urban sensing applications," *J. Franklin Inst.*, vol. 345, no. 6, pp. 618–639, 2008.

[50] F. Ahmad, M. G. Amin, and S. Kassam, "A beamforming approach to stepped-frequency synthetic aperture through-the-wall radar imaging," in *Proceedings of the IEEE First International Workshop on Computational Advances in Multi-Sensor Adaptive Processing, Puerto Vallarta, Mexico*, 2005, pp. 24–27.

[51] A. C. Gurbuz, J. H. McClellan, and W. R. Scott, "A compressive sensing data acquisition and imaging method for stepped frequency GPRs," *IEEE Trans. Signal*

Process., vol. 57, no. 7, pp. 2640–2650, Jul. 2009.

[52] R. J. Burkholder, I. J. Gupta, and J. T. Johnson, “Comparison of monostatic and bistatic radar images,” *IEEE Antenna Propag. Mag.*, vol. 45, no. 3, pp. 41–50, 2003.

[53] P. Bezoušek and V. Schejbal, “Bistatic and Multistatic Radar Systems,” *Radioengineering*, vol. 17, no. 3, pp. 53–59, 2008.

[54] P. Setlur, G. Smith, F. Ahmad, and M. Amin, “Target localization with a single sensor via multipath exploitation,” *IEEE Trans. Aerosp. Electron. Syst.*, vol. 48, no. 3, 2012.

[55] L. Wang and X. Huang, “Research on UWB SAR Image Formation with Suppressing Multipath Ghosts,” in *CIE Int. Conf. Radar*, 2006, pp. 1–3.

[56] A. AlBeladi, “Multipath exploitation in through-the-wall radar imaging using sparsity-driven detection,” King Fahd University of Petroleum and Minerals, 2015.

[57] M. Masood, “Distribution Agnostic Structured Sparsity Recovery: Algorithms and Applications,” King Abdullah University of Science and Technology, 2015.

[58] D. L. Donoho, “Compressed sensing,” *IEEE Trans. Inf. Theory*, vol. 52, no. 4, pp. 1289–1306, Apr. 2006.

[59] E. J. Candès, “Compressive sampling,” in *Proceedings of the International Congress of Mathematicians, European Mathematical Society, Madrid, Spain*, 2006.

[60] M. Leigsnering, “Sparsity-Based Multipath Exploitation for Through-the-Wall

Radar Imaging," der Technischen Universitat Darmstadt, 2015.

[61] L. Li, P. Boufounos, D. Liu, H. Mansour, and S. Sahinoglu, "Sparse MIMO Architectures For Through-The-Wall Imaging," in *Sensor Array and Multichannel Signal Processing Workshop (SAM), 2014 IEEE 8th*, 2014, pp. 513 – 516.

[62] D. L. Donoho, Y. Tsaig, I. Drori, and J. L. Starck, "Sparse solution of underdetermined systems of linear equations by stage wise orthogonal matching pursuit," *IEEE Trans. Inf. Theory*, vol. 58, no. 2, pp. 1094–1121, 2012.

[63] Q. Huang, L. Qu, B. Wu, and G. Fang, "UWB through-wall imaging based on compressive sensing," *IEEE Trans. Geosci. Remote Sens.*, vol. 48, no. 3, pp. 1408–1415, Mar. 2010.

[64] J. Tropp and A. Gilbert, "Signal recovery from random measurements via orthogonal matching pursuit," *IEEE Trans. Inf. Theory*, vol. 53, no. 12, pp. 4655–4666, 2007.

[65] D. Needell and R. Vershynin, "Uniform uncertainty principle and signal recovery via regularized orthogonal matching pursuit," *Found. Comput. Math.*, vol. 9, no. 3, pp. 317–334, 2009.

[66] D. Needell and A. Tropp, "CoSaMP: Iterative signal recovery from incomplete and inaccurate samples," *Appl. Comp. Harmon. Anal*, vol. 26, no. 3, pp. 301–321, 2009.

[67] P. Schniter, L. C. Potter, and J. Ziniel, "Fast Bayesian Matching Pursuit: Model Uncertainty and Parameter Estimation for Sparse Linear Models," *IEEE Trans. Signal Process. to be Publ.*, 2009.

[68] M. Masood and T. Y. Al-Naffouri, “Support agnostic bayesian matching pursuit for block sparse signals,” in *38th. IEEE Int. Conf. on Acoustics, Speech and Signal Processing (ICASSP 2013), Vancouver, Canada*, 2013, pp. 4643–4647.

[69] M. Masood and T. Al-Naffouri, “Sparse Reconstruction Using Distribution Agnostic Bayesian Matching Pursuit,” *Signal Process. IEEE Trans.*, vol. 61, no. 21, pp. 5298–5309, 2013.

[70] M. G. Amin, *Through-the-wall radar imaging*. CRC Press, Taylor and Francis Group, 2010.

[71] F. Ahmad, W. Zhang, and M. G. Amin, “Three-dimensional wideband beamforming for imaging through a single wall.,” *IEEE Geosci. Remote Sens. Lett.*, vol. 5, no. 2, p. 176—179, 2008.

[72] Y.-S. Yoon and M. Amin, “Compressed sensing technique for high-resolution radar imaging,” *Proc. SPIE Signal Process. Sens. Fusion Target Recognit. XVII*, vol. 6968, no. 1, 2008.

[73] J. Yang and Y. Zhang, “Alternating direction algorithms for L1-problems in compressive sensing,” *SIAM J. Sci. Comput.*, vol. 33, no. 1–2, pp. 250–278, 2011.

[74] M. Amin, F. Ahmad, and W. Zhang, “A compressive sensing approach to moving target indication for urban sensing,” in *2011 IEEE RadarCon (RADAR)*, 2011, no. 1, pp. 509–512.

[75] M. G. Amin and F. Ahmad, “Compressive sensing for through-the-wall radar imaging,” *J. Electron. Imaging*, vol. 22, no. 3, p. 030901, Jul. 2013.

[76] P. P. Vaidyanathan and P. Pal, “Sparse sensing with coprime arrays,” *Conf. Rec. - Asilomar Conf. Signals, Syst. Comput.*, vol. 59, no. 2, pp. 1405–1409, 2010.

[77] H. Achanta, S. Biswas, S. Dasgupta, M. Jacob, B. Dasgupta, and R. Mudumbai, “Coprime conditions for Fourier sampling for sparse recovery,” in *Proceedings of the IEEE Sensor Array and Multichannel Signal Processing Workshop*, 2014, pp. 533–536.

[78] Y. D. Zhang, S. Qin, and M. Amin, “DOA Estimation Exploiting Coprime Arrays With Sparse Sensor Spacing,” in *Acoustics, Speech and Signal Processing (ICASSP), 2014 IEEE International*, 2014, pp. 2267 – 2271.

[79] S. Qin, Y. Zhang, and M. Amin, “Generalized Coprime Array Configurations for Direction-of-Arrival Estimation,” *Signal Process. IEEE …*, vol. 63, no. 6, pp. 1377–1390, 2015.

[80] G. Di Martino and A. Iodice, “Coprime Synthetic Aperture Radar (CopSAR): A New Acquisition Mode for Maritime Surveillance,” *IEEE Trans. Geosci. Remote Sens.*, vol. 53, no. 6, pp. 3110–3123, 2015.

[81] “Theory of Sparse Coprime Sensing in Multiple Dimensions,” *IEEE Trans. Signal Process.*, vol. 59, no. 8, pp. 3592–3608, 2011.

[82] G. Di Martino, A. . Iodice, and S. Medagli, “Orthogonal coprime SAR,” in *2015 IEEE International Geoscience and Remote Sensing Symposium (IGARSS)*, 2015, pp. 3758–3761.

[83] J. Ramirez and J. Krolik, “Multiple source localization with moving co-prime

arrays," in *2015 IEEE International Conference on Acoustics, Speech and Signal Processing (ICASSP)*, 2015, pp. 2374–2378.

[84] S. Qin, Y. D. Zhang, and M. . Amin, "Sparsity-based multi-target localization exploiting multi-frequency coprime array," in *2015 IEEE China Summit and International Conference on Signal and Information Processing (ChinaSIP)*, 2015, pp. 329–333.

[85] C. Zhou, Z. Gu, S. Yujie, and N. . Goodman, "Doa estimation by covariance matrix sparse reconstruction of coprime array," in *2015 IEEE International Conference on Acoustics, Speech and Signal Processing (ICASSP)*, 2015, pp. 2369 – 2373.

[86] D. Mitchell, "An Alternative Characterisation of All Primitive Pythagorean Triples," *Math. Gaz.*, vol. 85, no. 503, pp. 273–275, 2001.

[87] "Coprime integers." [Online]. Available: https://en.wikipedia.org/wiki/Coprime_integers. [Accessed: 23-Feb-2016].

[88] D. Hugues, S.-G. Lassus, D. David, and R. Guillaume, "Range Reduction Based on Pythagorean Triples for Trigonometric Function Evaluation," in *2015 IEEE 26th International Conference on ASAP: Application-Specific Sys-tems, Architectures and Processor*, 2015, pp. 74–81.

[89] L. Price, "Pythagorean tree: A new species." [Online]. Available: http://arxiv.org/abs/0809.4324. [Accessed: 22-Feb-2016].

[90] D. McCullough, "Height and excess of Pythagorean triples," *Mathematics Magazine 78*, pp. 26–44, 2005.

[91] M. Leigsnering, C. Debes, and A. M. Zoubir, “Compressive Sensing in Through-The-Wall Radar Imaging,” in *IEEE Int. Conf. Acoustics, Speech and Signal Processing*, 2011, pp. 4008–4011.

[92] G. Gennarelli, V. Gemine, P. Braca, and M. Amin, “Multiple Extended Target Tracking for Through-Wall Radars,” *IEEE Trans. Geosci. Remote Sensing, To Appear*, 2015.

[93] Q. Wu, Y. D. Zhang, F. Ahmad, and M. G. Amin, “Compressive-sensing-based high-resolution polarimetric through-the-wall radar imaging exploiting target characteristics,” *IEEE Antennas Wirel. Propag. Lett.*, vol. 14, pp. 1043–1047, 2015.

[94] Y. C. Eldar, P. Kuppinger, and H. Bolcskei, “Block-sparse signals: uncertainty relations and efficient recovery,” *IEEE Trans. Signal Process.*, vol. 58, no. 6, pp. 3042–3054, Jun. 2010.

[95] Q. Wu, Y. D. Zhang, M. G. Amin, and B. Himed, “Multi-Task Bayesian Compressive Sensing Exploiting Intra-Task Dependency,” *IEEE Signal Process. Lett.*, vol. 22, no. 4, pp. 430–434, 2015.

[96] “Earth Mover’s Distance,” 2009. [Online]. Available: http://www.mathworks.com/matlabcentral/fileexchange/22962-the-earth-mover-s-distance. [Accessed: 14-Mar-2016].

[97] P. Setlur, M. Amin, and F. Ahmad, “Multipath Doppler signatures from targets moving behind walls,” in *2010 IEEE Radar Conference*, 2010, pp. 799–803.

[98] K. Liu, “Range-based source localisation with pure reflector in presence of

multipath propagation," *Electron. Lett.*, vol. 46, no. 13, p. 957—958, 2010.

[99] G. E. Smith and B. G. Mobasseri, "Robust Through-the-Wall Radar Image Classification Using a Target-Model Alignment Procedure," *Image Process. IEEE Trans.*, vol. 21, no. 2, pp. 754–767, 2012.

[100] A. H. Muqaibel, M. G. Amin, and F. Ahmad, "Directional multipath exploitation for stationary target localization with a single-antenna," in *International Radar Conference: catching the invisible*, 2014.

[101] M. Balthasar, M. Leigsnering, and A. M. Zoubir, "Compressive Classification for Through-The-Wall Radar Imaging," in *20th European Signal Processing Conference (EUSIPCO 2012)*, 2012, no. Eusipco, pp. 2288–2292.

[102] J. . Wu, Q. . c Liang, Z. . Zhou, X. . Wu, and B. . Zhang, "Compressive sensing for sense-through-wall UWB noise radar signal," in *Proceedings of the 2011 6th International ICST Conference on Communications and Networking*, 2011, pp. 979–983.

[103] Y.-S. Yoon and M. Amin, "Through-The-Wall Radar Imaging Using Compressive Sensing Along Temporal Frequency Domain," in *ICASSP 2010*, 2010, pp. 2806–2809.

[104] D. Garren, J. Goldstein, D. Obuchon, R. Greene, and J. North, "SAR image formation algorithm with multipath reflectivity estimation," in *Proceedings of the IEEERadar Conference, 2004*, 2004, pp. 323–328.

VITAE

Name :Abdi Talib Abdalla

Nationality :Tanzanian

Date of Birth :10/1/1979

Email :abdit@kfupm.edu.sa; abdit@hotmail.com

Address :Zanzibar, Tanzania

Academic Background :MSc. In Electronic Engineering and Information Technology, University of Dar es Salaam, Tanzania, 2010